Title

Biomaterials for Enhanced Care in Sickle Cell Disease and Complex Wounds

Author

Enueme, Nneamaka Isioma

Publication Date

2025

Peer reviewed|Thesis/dissertation

UNIVERSITY OF CALIFORNIA

Los Angeles

Biomaterials for Enhanced Care in Sickle Cell Disease and Complex Wounds

A dissertation submitted in partial satisfaction of the requirements for the degree Doctor of Philosophy in Bioengineering

by

Nneamaka Isioma Enueme

2025

ABSTRACT OF THE DISSERTATION

Biomaterials for Enhanced Care in Sickle Cell Disease

and Complex Wounds

by

Nneamaka Isioma Enueme

Doctor of Philosophy in Bioengineering

University of California, Los Angeles, 2025

Professor Andrea M. Kasko, Chair

This dissertation presents a materials-driven approach to designing therapeutics that respond to the clinical complexity of sickle cell disease (SCD) and trauma-induced wounds. Though vastly different in origin, both challenges are marked either by oxidative stress, impaired tissue healing, or high infection risk-particularly in underserved populations or austere environments. While curative therapies for SCD exist, their financial inaccessibility and infrastructural demands highlight an urgent need for intermediate, accessible treatment options. Similarly, battlefield and trauma wounds require rapid, on-site care that is robust and capable of sustained therapeutic delivery. This work addresses both challenges by developing modular biomaterials built primarily from naturally derived components and engineered for function. Over the course of this project, I synthesized flavonoid-based macromolecules and developed chitosan- and PEG-based hydrogels to investigate how material chemistry can be tuned to deliver therapeutic function over time. Specifically, I engineered flavonoid-based macromolecules to enable sustained antioxidant activity, targeting the oxidative stress that drives vaso-occlusion and disease progression in SCD. I also designed two distinct hydrogel systems. The chitosan-based

hydrogels release a vasodilator and an antibiotic to address the impaired perfusion and microbial colonization characteristic of sickle cell leg ulcers. Alternatively, the PEG-based hydrogel system was engineered for rapid polymerization and multifunctional delivery, releasing antibiotics, hemostatic agents, and analgesics to meet the urgent therapeutic needs of battlefield and trauma wounds. I characterized all constructs for functional properties, including degradability, drug release kinetics, radical scavenging activity, mechanical performance, cytocompatibility, and their ability to interact with biological tissue without impairing healing. Key findings demonstrate that the flavonoid-macromer systems display sustained antioxidant activity, with tunable release governed by functionalization and degradation rate. Hydrogels designed for local drug delivery exhibited favorable mechanical properties and released therapeutics over multi-day periods. When translated into preclinical models, the PEG-based systems significantly reduced microbial burden and demonstrated efficacy in both murine and large animal studies. Altogether, this body of work establishes a framework for developing accessible biomaterials that address the challenges of systemic disease and complex wound care. By integrating natural therapeutics with materials design, this dissertation contributes new tools to a space where efficacy, biocompatibility, and accessibility are equally critical. These materials not only hold potential to alleviate the burden of sickle cell complications but also extend toward broader applications in trauma care, offering practical solutions where conventional therapies fall short.

The dissertation of Nneamaka Isioma Enueme is approved.

Nasim Annabi

Nicholas Matthew Bernthal

Timothy J. Deming

Nabil J. Tawil

Andrea M. Kasko, Committee Chair

University of California, Los Angeles

2025

DEDICATION

To my amazing support system - God, mama bear, my sisters and my brothers.
To my dad, I miss you every day. Thank you for everything.

TABLE OF CONTENTS

Chapter 1: Introduction and Background 1

1.1 Understanding Sickle Cell Disease (SCD) and its complications 1

1.2 Global impact of SCD 2

1.3 Current treatment, disease management and limitations 3

1.4 Scope of research 6

References 9

Chapter 2: Synthesis of Flavonoid-based Macromolecules: Antioxidant Therapy 14

2.1 Introduction 14

2.2 Materials and methods 16

2.3 Results and discussion 24

2.4 Conclusions 40

2.5 Supplemental Information 41

References 47

Chapter 3: Multifunctional Chitosan Hydrogels Targeting Sickle Cell Leg Ulcers 55

3.1 Introduction 55

3.2 Materials and methods 57

3.3 Results and discussion 68

3.4 Conclusions 82

3.5 Supplemental information 84

Chapter 4: Hydrogel Wound Dressings for Prolonged Field Care in Austere Environments ..97

4.1 Introduction 97

4.2 Materials and methods 99

4.3 Results and discussion 104

4.4 Conclusions 117

4.5 Supplemental Information 119

References 124

Chapter 5: Future perspective and broader impact 128

LIST OF FIGURES

CHAPTER 1

Figure 1. 1. A summary of the clinical complications of sickle cell disease 2

Figure 1. 2. A map showing the worldwide birth incidence of sickle cell disease per 100,000 livebirths 3

CHAPTER 2

Figure 2. 1. Role of antioxidant therapy in SCD management[9].....16

Figure 2. 2. Graphical representation of the setup used for soxhlet extraction (created with BioRender).....25

Figure 2. 3. Atom numbering of apigeninidin.....26

Figure 2. 4 Stacked IR spectra of apigeninidin and apigeninidin polymers. IP stands for interfacial polymer and CP stands for condensation polymer.....28

Figure 2. 5. Stacked ^{1}HNMR spectra of apigenin-MMP after a 30-day incubation in PBS at 37 °C. The phenol peak of apigenin labeled 'x' in the box was used to calculate hydrolytic degradation.....32

Figure 2. 6. Stacked FTIR spectra of apigenin-PETMP after a 30-day incubation in PBS at 37 °C, showing the appearance of broad phenol bands in relation to time change. 33

Figure 2. 7. In vitro release profiles of A) apigenin and B) apigeninidin. Concentrations were determined using a standard curve.....36

Figure 2. 8. Radical scavenging activity of apigeninidin and apigeninidin polymers. Ascorbic acid and unconjugated apigeninidin were set as the standard (control).....38

Figure 2. 9. Radical scavenging activity of apigenin-thiol molecules over time and hydrolysis duration. A) Apigenin-PETMP and B) Apigenin-MMP. "Day 0" to "Day 30" refer to timepoints collected during hydrolysis studies.....40

CHAPTER 3

Figure 3. 1. A) Elastic modulus and swelling ratio trends of CHIMA hydrogels. B) Time-dependent swelling ratio of CHIMA hydrogels. 71

Figure 3. 2. A) Images of bacterial culture plates after ZOI experiments. B) Quantification of the ZOI studies. 74

Figure 3. 3. Hydrogel-cell compatibility assays. 76

Figure 3. 4. Hydrogel cell-adhesion assay 77

Figure 3. 5. In vitro adhesive properties of 3.2% CHIMA gels using pig lung tissue 79

Figure 3. 6. Chemical structures of A) amlodipine and B) doxycycline 81

Figure 3. 7. In vitro kinetic release of amlodipine from chitosan hydrogels 82

CHAPTER 4

Figure 4. 1. Research workflow diagram illustrating the sequential steps to develop and validate our hydrogel platform. 99

Figure 4. 2. Design and synthesis of 35mL hydrogels for large animal studies. 105

Figure 4. 3. Kinetic release profiles of therapeutic agents from PEGDA 3350 hydrogels. 108

Figure 4. 4. HPLC chromatograms. 110

Figure 4. 5. Minimum inhibitory concentration (MIC) assay for PEGDA 3350 hydrogels 112

Figure 4. 6. In vivo efficacy of drug release in murine models 115

Figure 4. 7. In vivo efficacy in ovine models 117

LIST OF TABLES

CHAPTER 1

Table 1. 1. Overview of current therapeutic strategies for sickle cell disease, their mechanisms, clinical progress, and associated limitations. 5

CHAPTER 2

Table 2. 1. Showing the temperature at which 25% of each material is degraded 27

Table 2. 2. Showing the hydrolytic degradation of apigenin-MMP in respect to the integral of 'x' peak 31

Table 2. 3. The hydrodynamic size and polydispersity index for the various PLGA microparticle formulations 34

Table 2. 4. IC_{50} values of apigeninidin and apigeninidin polymers. Ascorbic acid was used as the standard 37

Table 2. 5. Estimated molecular weight of polymers based on NMR analysis. 38

CHAPTER 3

Table 3. 1. A table showing the CHIMA/ PEGDA hydrogel formulation. Therapeutics for release studies were typically added to the water composition of the hydrogel. I2959 stands for Irgacure 2959. 59

Table 3. 2 Showing the drug stock concentrations for each therapeutic and the final amount in each hydrogel disc 67

Table 3. 3. A table showing the mesh size of the hydrogel groups in correlation to their respective water retention ability. 72

Table 3. 4. Effect of Irgacure 2959 concentration on the modulus of DOX and AML-loaded hydrogels compared to blank unloaded gels. 80

CHAPTER 4

Table 4. 1. Showing the experimental and derived mechanical properties of the different molecular weight PEGDA hydrogels 106

Table 4. 2. Showing the MIC of antibiotics released from the hydrogel against S. aureus and P. aeruginosa 111

ACKNOWLEDGEMENTS

I would like to express my deepest gratitude to my mentor and committee chair, Professor Andrea Kasko. Dear Andrea, thank you for taking a chance on me from the first day I showed up on a Zoom call in your drug delivery class. You saw so much potential in my ideas and continuously inspired me to build it into what they are today. Thank you for teaching me and inspiring me to love science. You have built such a beautiful lab culture, and I will forever be grateful to be a Kasko Lab Alum. Finally, thank you for making my research dreams come true by believing in the sickle cell project.

I would also like to thank all my committee members for all their support and for always believing in me and giving me great advice. Professor Deming, taking your class made me enjoy polymer chemistry and the behind the scenes of biomaterials research. Professor Tawil, I was always so encouraged by our random check-ins on my work and progress in the Engineering V hallway, thank you for believing in me. Professor Annabi, thank you for believing in my hydrogel project and allowing me to work on various aspects of it in your lab – I truly appreciate you. Finally, Professor Bernthal – thank you for being such a great collaborator, I have learned so much from you and your team and I am honored to have worked on a project with you.

To my mum – my number 1 role model, without you I would not be here. Thank you for always believing in me, even in the moments I had no fight left you believed I could do it. Thank you for taking care of me and always sending me milo. I love you to the moon and back.

To my dad – thank you for being the perfect example of perseverance. Thank you for teaching me the wisdom of contentment. I wish you were here to see you little girl get her PhD. Your legacy lives on. I miss you.

To my sisters – Lulu and Chinanya, thank you for inspiring me every single day of my PhD. You both inspired my projects. Thank you for picking my late-night calls when I needed advice

and motivation to keep going. I am so grateful to have learned how to keep fighting and persevere from you both. I love you with all my heart.

To my brothers – Josh and Oly, thank you for believing in me and getting me into video games – it helped me in so many ways after a long day of research.

To Haley – thank you for pushing me and praying with me, I will never forget that pep talk in the middle of the UCLA store about Thomas Edison. I love and miss you.

To Mel – Melimel, your friendship means so much to me, thank you for all the late-night laughs and chats that helped us push each other.

To Rebecca and Kalkidan – thank you for always encouraging me with flowers and cards when I had a difficult day. Most of all with prayers. I wouldn't be here without you both.

To Erika and Laura – thank you for being amazing spiritual mentors. Thank you for your great advice and support.

To Bolu, Meso, Steph and Sogo – my day ones. Regardless of being 7000 miles away for the most part, you were always there for me. I love you all and miss you

To Moriel – PhD bestie for the restie. Thank you for everything, I appreciate how much you pushed me to keep going. I absolutely loved our brunches, they sustained me.

To Shadi – Shaddsss, thank you for teaching me how to use almost every equipment in lab. I enjoyed our in-n-out trips and chats about the future. You were a friend in lab I could always talk to when I missed home.

To Elizabeth – Lizzz, the best hood mate ever. Thank you for being an amazing friend and collaborator. You are someone I can always rely on.

To Brooke – thank you for being a great friend and teacher. I admire you in so many ways. I am grateful for our shared love for anime.

To Kelly – my taco bell partner. Thank you for being a listening ear and chatting about chemistry with me when research was tough. You are the best.

To Kirstie – thank you for all the afternoons at the DLS lab running my samples, you are such a sweet friend, and I appreciate you.

To James and Andrew – thank you for the time we spent together in the Kasko lab, you both are amazing friends. James, I have not forgotten the promised TikTok challenge.

To Anika and Ali – thank you for being the best undergraduate mentees, you both are incredible scientists. I cannot wait to see the amazing things you will do.

VITA

2019	B.S., Microbiology Covenant University, Ota, Nigeria
2022	M.Sc., Bioengineering University of California, Los Angeles
2025	Ph.D., Bioengineering (expected) University of California, Los Angeles

PUBLICATIONS

Jackson Hoffman, B. A., Pumford, E. A., **Enueme, A. I**., Fetah, K. L., Friedl, O. M., & Kasko, A. M. (2023). Engineered macromolecular Toll-like receptor agents and assemblies. Trends in biotechnology, 41(9), 1139–1154.

Akinnola, O.O., Ajayi, S.A., Ogunleye, B.O., **Enueme, N.I**. (2020). Disinfection by-products in swimming pools and health-related issues. In M.N.V Prasad (Eds.), Disinfection Byproducts in Drinking Water (pp. 235-252). Elsevier Science.

IN PREPARATION

Pumford, E. A., Hamad, C., **Enueme, A.I**., Mamouei, Z., Bernthal, N.M., Kasko, A.M., Wenke, J.C., Wainwright, W. (2025). Advanced drug eluting hydrogel wound dressing for prolonged field care: Innovations in drug delivery and trauma management. Science Translational Medicine. Manuscript submitted

Enueme, A. I., Kasko, A.M. (2025). Multifunctional chitosan hydrogels targeting sickle cell leg ulcers. Journal of Biomaterials Research Part A. Manuscript in preparation

Enueme, A. I., Kasko, A.M. (2025). Synthesis of Flavonoid-Based Macromers for Sustained Antioxidant Therapy. Manuscript in preparation

Enueme, A. I., Jackson Hoffman, B.A., Pumford, E.A., Kasko, A.M. (2025) Bioengineered interventions for complications of sickle cell disease. Manuscript in preparation

PRESENTATIONS

Enueme, A. I., Kasko, A. M. (2025). Multifunctional Chitosan Hydrogels Targeting Venous and Sickle Cell Leg Ulcers. Excellence in Graduate Polymer Research Symposium. ACS Spring, 2025. March 23-27, 2025, San Diego, CA.

Enueme, A. I., Kasko, A. M. (2024). Chitosan Hydrogels for Treating Venous Ulcers. Oral presentation at 7th Annual Bioengineering Research Day, UCLA. February 16, 2024, Los Angeles, CA.

Enueme, A. I. (2018). Coagulase Negative Staphylococci. Seminar presented to the Biological Science Department, Covenant University, Nigeria. November 2018, Nigeria.

Chapter 1: Introduction and Background

1.1 Understanding Sickle Cell Disease (SCD) and its complications

"A disease believed to have evolved as a defense against malaria is now the most prevalent inherited genetic disorder worldwide"[1,2]. SCD is an umbrella term used to describe specific variations of a red-blood cell (RBC) mutation. These include sickle cell anemia (HbSS), the most common and severe form; HbS β-thalassemia and HbSC, which involve co-inheritance of hemoglobin S (HbS) with another abnormal β-globin; and other sickle cell variants such as HbSD, HbSE, Hb Lepore, and HbO-Arab[3]. They are caused by a single nucleotide mutation in the β-globin gene that leads to several life altering complications[3,4].

SCD begins at the molecular level when a single point mutation replaces the amino acid, glutamic acid for valine leading to the production of HbS. Unlike normal hemoglobin, HbS undergoes polymerization, forming rigid 14-membered fibres that elongate to form rod-like polymers that denature the naturally round RBCs, and alter their properties[5]. At the macroscopic level, this cellular sickling causes significant vessel occlusion that triggers the acute and chronic complications seen in SCD patients (**Fig. 1.1**). The pathophysiology of each SCD complication is similar; however, the manifestation of these complications are dependent on the affected region of the human body[6]. The most prevalent and life-threatening complication is vaso-occlusive crisis (VOC). As the name implies, it is a downstream effect of blockages occuring in the blood vessels in response to denatured RBC. Vaso-occlusion generally occurs due to impaired blood flow caused by increased plasma viscosity as well as RBC sequestration[7]. VOC manifests in three distinct types of pain: acute recurrent painful episodes, chronic pain syndromes, and neuropathic pain. Acute painful crises are a hallmark SCD and the leading cause of hospitalization. These episodes are characterized by inflammation, reduced red blood cell flexibility, and pain caused by tissue damage. Chronic pain syndromes, which may persist for months, are often associated with avascular necrosis,

inflammatory pain, leg ulcers, and chronic osteomyelitis. Lastly, the third manifestation, neuropathic pain although fairly evaluated in SCD patients, is characterized as a burning or sharp sensation[8,9]. Asides from the crisis symptoms described above, vaso-occlusion also drives other severe SCD complications including chronic organ damage and non-healing leg ulcers that progress from tissue ischemia. These complications are known to greatly affect the quality of life[10].

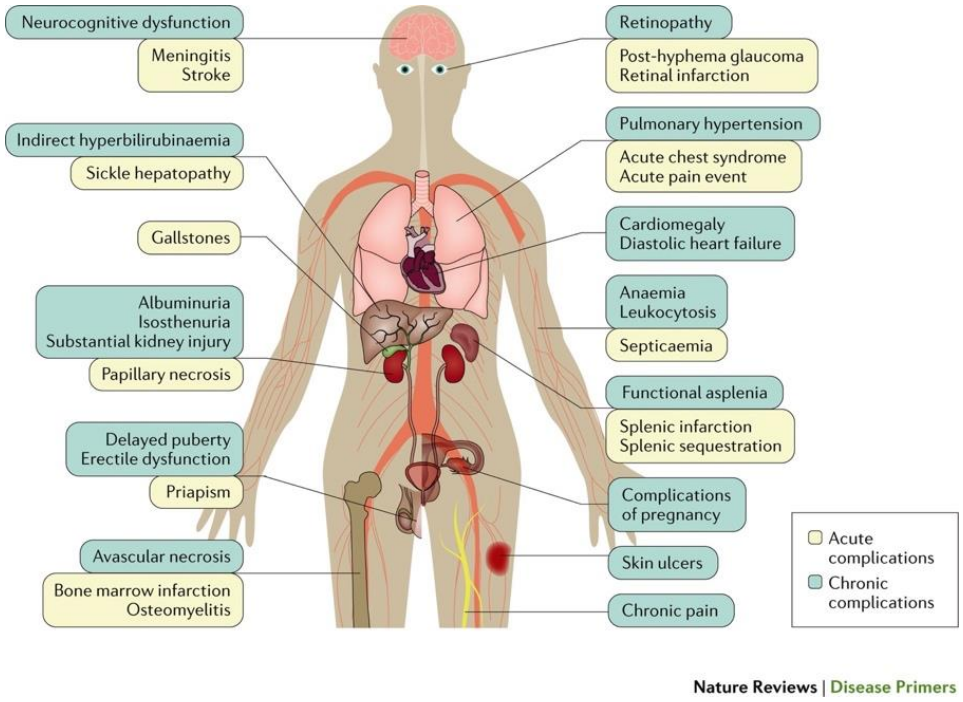

Figure 1. 1. A summary of the clinical complications of sickle cell disease[11.]

1.2 Global impact of SCD

The impact of SCD on health and the economy is one of the incentives for research in this field. A Global Burden of Disease study reports SCD affecting 7.74 million individuals worldwide, with approximately 300 million living with the trait[12]. The prevalence and incidence of the disease has increased globally by 41.4% in 21 years. It is also increasingly becoming one of the factors that contribute to health care burdens and disparities worldwide, with higher incidence in malaria endemic regions of Africa, the Middle East, the Caribbean and South Asia[12,13] (**Fig. 1.2**). One of the major health care burdens include the high incidence

of child mortality. Cross-sectional studies show that under-5 mortality rate for SCD (the probability of a newborn dying before the age of 5), is as high as 90%, with sickle cell disease attributing for 7.3% of under-5 mortalities in Africa[12]. The economic burden of SCD is also substantial. Due to the numerous complications associated with the disease, individuals often face high healthcare costs. In 2016 alone, the total economic burden of in-patient care was $811 million. SCD related lifetime medical costs also add up to approximately $1.7 million per individual[14].

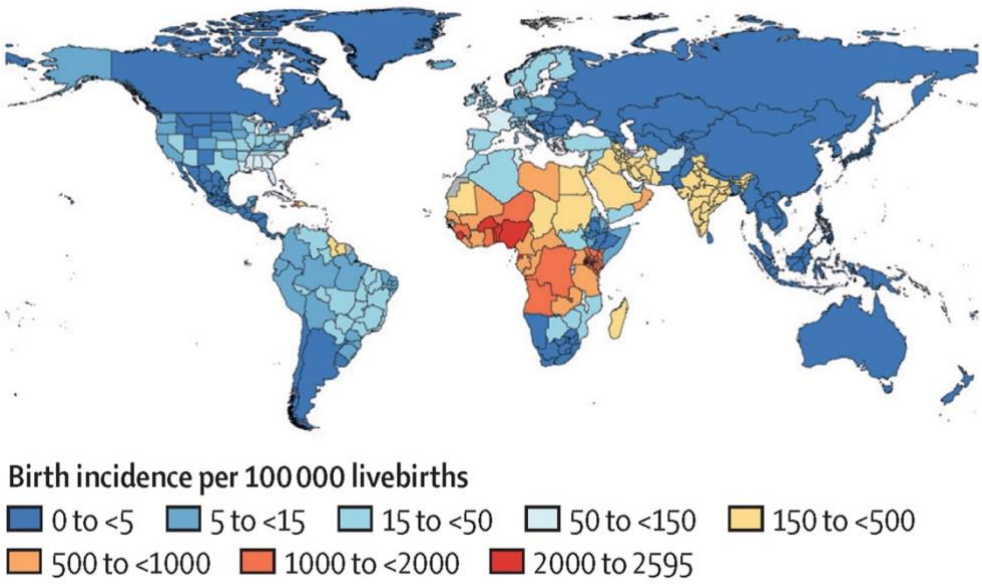

Figure 1. 2. A map showing the worldwide birth incidence of sickle cell disease per 100,000 livebirths[12]

1.3 Current treatment, disease management and limitations

Considering the complications of SCD and the impact the disease has on the livelihood of individuals all around the world, several treatment strategies have been explored to manage the disease. These strategies range from the use of pharmaceuticals for disease management, to curative approaches with hematopoietic stem cell transplantation (HSCT) and gene therapy. Undoubtedly, advances in gene therapy have created a 'beacon of hope' for SCD patients. By modifying the patient's genotype to target the root cause of the disease, these therapies,

primarily gene editing and gene addition, offer the potential of a lifelong cure[15–17]. Gene addition strategies use vectors, such as lentiviruses, to introduce anti-sickling β-globin genes, while gene editing approaches like CRISPR-Cas9, activate γ-globin gene expression to elevate fetal hemoglobin (HbF) levels in the bloodstream. These methods, alongside HSCT show great promise, with clinical trials reporting increased hemoglobin levels (**Table 1.1**).

Despite these advances, the 'beacon of hope' they offer has been dimmed by the financial burden associated with these therapies. As of 2023, ten promising treatments for SCD were in clinical testing, each with the potential to revolutionize disease management. However, the projected costs for these therapies were around $2 million. Recently approved gene therapies: Casgevy and Lyfgenia exemplify this issue, priced at $2.2 million and $3.1 million respectively[18,19]. For many individuals in the affected population, these curative treatments remain financially inaccessible, illustrating that while scientific breakthroughs have brought us closer to a cure, equitable access is still a distant goal[16].

Another growing aspect in SCD management involves the use of disease-modifying drugs that inhibit HbS polymerization. These therapies act either by stabilizing the oxygenated form of HbS, as seen with voxelotor or by inducing fetal hemoglobin production, such as with hydroxyurea[15,20]. While more accessible than gene therapy, these drugs come with their own challenges such as the necessity for lifelong oral administration, potential organ toxicity, treatment dependency, and psychological strain[21]. Finally, for localized, non-systemic complications such as leg ulcers, standard care relies on non-specific interventions like compression therapy, negative pressure devices, and analgesics. These approaches, while helpful, often fail to address the underlying pathology that stems from vessel occlusion, allowing the wounds to persist and significantly diminish quality of life. Taken together, these limitations underscore two urgent needs in SCD care: (1) the development of effective therapies that can serve as a bridge while curative therapy remains financially out of reach, and (2) the creation of lower-toxicity interventions that provide targeted treatment for SCD-related

complications. To address these treatment gaps, bioengineered solutions offer a promising yet underexplored avenue, which we aim to further develop in this work.

Table 1. 1. Overview of current therapeutic strategies for sickle cell disease, their mechanisms, clinical progress, and associated limitations.

Therapy	Mechanism	Recent progress	Limitations
Hemopoietic stem cell transplantation [21–23]	• Autologous: use of the patient's own stem cells • Allogenic: use of donor stem cells	Over 50 clinical trials as of 2025 with about 25 currently recruiting	• Limited affordability • Low donor availability • Patient rejection • Risk of death • Age limitations
Gene therapy			
Gene addition [15,24,25]	• Lentiviral vectors • Gammaretroviral vectors • Others e.g adenoviral and foamy viral vectors	Lyfgenia (FDA approved in 2023) NCT02140554	• Limited affordability • Risk of hematologic malignancy
Gene editing[25,26]	• The use of transcription activator-like effector nucleases • CRISPR-Cas 9 • Zinc finger nucleases	Casgevy (FDA approved in 2023) NCT03745287	• Limited affordability • Ethical concerns
Disease-modifying therapy			
Hydroxyurea [15,27]	• Increase of HbF production	FDA approved in 1998	• Impact on HbF decreases over time • Side effects including myelosuppression
Voxelotor[20,23,28,29]	• Increase of hemoglobin oxygen affinity	FDA approved in 2019 Discontinued in 2024	• Side effects such as increased risk of venous thrombosis • Discontinued because of risks that outweigh the benefits
Targeting vaso-occlusion and inflammation (drug therapy)			

Crizanlizumab[15,20]	• Inhibits RBC adhesion	FDA approved in 2019 Discontinued in the EU in 2023	• Discontinued
Poloxamer[6,30]	• Reducing blood viscosity and adhesion of sickled cells to the endothelium (ref)	Phase III clinical trial NCT01737814	• 2021 studies show that poloxamer does not improve the symptoms of VOC
L-glutamine[31]	• Preventing oxidative damage	FDA approved in 2017	• Mild and infrequent adverse effects
N-acetylcysteine	• Oxidative stress reduction	FDA approved NCT01800526	• Mild and infrequent adverse effects

1.4 Scope of research

This dissertation seeks to address the critical challenges outlined above by exploring how bioactive compounds and bioengineering principles can be harnessed to develop therapeutic materials for SCD. The research primarily focuses on two debilitating complications that significantly affect quality of life: vaso-occlusive crises and sickle cell leg ulcers. In chapter 2, we utilize naturally occurring compounds (flavonoids) to synthesize macromolecules that can act as slow releasing antioxidants to relieve oxidative stress in SCD – a factor shown to influence the progression of painful crises[32]. In chapter 3, we synthesize a tunable, photo-crosslinked hydrogel network from chitosan that aims to release antibiotics and a vasodilator locally. This approach targets microvascular occlusion, a driving force behind ischemia and the chronicity of non-healing leg ulcers in SCD patients.

Exploiting bio-active molecules: Chitosan and Flavonoids

Chitosan and flavonoid compounds were selected for these studies because they offer unique advantages as therapeutic agents due to their inherent bioactivity and biocompatibility.

Chitosan, a naturally derived polysaccharide, is widely recognized for its biocompatibility, biodegradability, and intrinsic antimicrobial activity. In the context of wound care, particularly for SCD-associated leg ulcers, chitosan offers several key benefits. Its positive charge allows it to interact with negatively charged bacterial cell membranes, leading to antimicrobial effects without the need for additional antibiotics. Furthermore, its chemical structure also allows for functionalization and crosslinking, enabling the design of hydrogels with tunable mechanical and drug release properties[33]. **Flavonoids**, a diverse class of polyphenolic compounds found in plants, are known for their antioxidant and anti-inflammatory properties. In SCD, chronic oxidative stress plays a pivotal role in hemolysis, endothelial dysfunction, and the increased incidence of vaso-occlusive crises. By leveraging the radical scavenging capabilities of flavonoids, we aim to explore their incorporation into polymer networks as sustained-release antioxidant agents[32].

By incorporating chitosan and flavonoids into biomaterial design, the majority of this dissertation highlights a dual approach (utilizing both structure and function) to address the complications of SCD. Their use also aligns with the growing need for safer, naturally derived therapeutics.

Broader applications in complex wounds

Expanding beyond SCD, Chapter 5 applies similar hydrogel synthesis strategies developed in Chapter 4 to address the challenges of complex, traumatic wounds. This is a collaborative project funded by the U.S. Department of Defense and working with colleagues in the UCLA Department of Orthopaedic Surgery, and the University of Texas Medical Branch that focuses on battlefield injuries—settings where access to timely and comprehensive wound care is limited. In this chapter, we develop hydrogels capable of inhibiting both gram-negative and gram-positive bacterial colonization, while concurrently providing analgesic and hemostatic effects. The unifying theme of this dissertation lies in the rational to design of

biomaterials that not only address the pathophysiological complexity of SCD but are also translatable to broader wound care applications. By leveraging natural compounds and bioengineering tools, this work contributes to the ongoing effort to develop accessible, effective, and targeted therapies for both genetic complications and trauma-induced chronic wounds.

References

(1) Serjeant, G. R. The Natural History of Sickle Cell Disease. *Cold Spring Harb. Perspect. Med.* **2013**, *3* (10), a011783. https://doi.org/10.1101/cshperspect.a011783.

(2) Shriner, D.; Rotimi, C. N. Whole-Genome-Sequence-Based Haplotypes Reveal Single Origin of the Sickle Allele during the Holocene Wet Phase. *Am. J. Hum. Genet.* **2018**, *102* (4), 547–556. https://doi.org/10.1016/j.ajhg.2018.02.003.

(3) Kapoor, S.; Little, J. A.; Pecker, L. H. Advances in the Treatment of Sickle Cell Disease. *Mayo Clin. Proc.* **2018**, *93* (12), 1810–1824. https://doi.org/10.1016/j.mayocp.2018.08.001.

(4) Aljabry, M.; Sulimani, S.; Alotaibi, G.; Aljabri, H.; Alomary, S.; Aljabri, O.; Sallam, M.; Alsultan, A. Prevalence and Regional Distribution of Beta-Hemoglobin Variants in Saudi Arabia: Insights from the National Premarital Screening Program". *J. Epidemiol. Glob. Health* **2024**, *14* (3), 1242–1248. https://doi.org/10.1007/s44197-024-00281-x.

(5) Vekilov, P. G. Sickle-Cell Haemoglobin Polymerization: Is It the Primary Pathogenic Event of Sickle-Cell Anaemia? *Br. J. Haematol.* **2007**, *139* (2), 173–184. https://doi.org/10.1111/j.1365-2141.2007.06794.x.

(6) Casella, J. F.; Barton, B. A.; Kanter, J.; Black, L. V.; Majumdar, S.; Inati, A.; Wali, Y.; Drachtman, R. A.; Abboud, M. R.; Kilinc, Y.; Fuh, B. R.; Al-Khabori, M. K.; Takemoto, C. M.; Salman, E.; Sarnaik, S. A.; Shah, N.; Morris, C. R.; Keates-Baleeiro, J.; Raj, A.; Alvarez, O. A.; Hsu, L. L.; Thompson, A. A.; Sisler, I. Y.; Pace, B. S.; Noronha, S. A.; Lasky, J. L., III; de Julian, E. C.; Godder, K.; Thornburg, C. D.; Kamberos, N. L.; Nuss, R.; Marsh, A. M.; Owen, W. C.; Schaefer, A.; Tebbi, C. K.; Chantrain, C. F.; Cohen, D. E.; Karakas, Z.; Piccone, C. M.; George, A.; Fixler, J. M.; Singleton, T. C.; Moulton, T.; Quinn, C. T.; de Castro Lobo, C. L.; Almomen, A. M.; Goyal-Khemka, M.; Maes, P.; Emanuele, M.; Gorney, R. T.; Padgett, C. S.; Parsley, E.; Kronsberg, S. S.; Kato, G. J.; Gladwin, M. T. Effect of Poloxamer 188 vs Placebo on Painful Vaso-Occlusive Episodes

in Children and Adults With Sickle Cell Disease: A Randomized Clinical Trial. *JAMA* **2021**, *325* (15), 1513–1523. https://doi.org/10.1001/jama.2021.3414.

(7) Sundd, P.; Gladwin, M. T.; Novelli, E. M. Pathophysiology of Sickle Cell Disease. *Annu. Rev. Pathol. Mech. Dis.* **2019**, *14* (Volume 14, 2019), 263–292. https://doi.org/10.1146/annurev-pathmechdis-012418-012838.

(8) Uwaezuoke, S. N.; Ayuk ,Adaeze C; Ndu ,Ikenna K; Eneh ,Chizoma I; Mbanefo ,Ngozi R; and Ezenwosu, O. U. Vaso-Occlusive Crisis in Sickle Cell Disease: Current Paradigm on Pain Management. *J. Pain Res.* **2018**, *11* (null), 3141–3150. https://doi.org/10.2147/JPR.S185582.

(9) Ballas, S. K.; Gupta, K.; Adams-Graves, P. Sickle Cell Pain: A Critical Reappraisal. *Blood* **2012**, *120* (18), 3647–3656. https://doi.org/10.1182/blood-2012-04-383430.

(10) Francis, R. B. Large-Vessel Occlusion in Sickle Cell Disease: Pathogenesis, Clinical Consequences, and Therapeutic Implications. *Med. Hypotheses* **1991**, *35* (2), 88–95. https://doi.org/10.1016/0306-9877(91)90029-x.

(11) Kato, G. J.; Piel, F. B.; Reid, C. D.; Gaston, M. H.; Ohene-Frempong, K.; Krishnamurti, L.; Smith, W. R.; Panepinto, J. A.; Weatherall, D. J.; Costa, F. F.; Vichinsky, E. P. Sickle Cell Disease. *Nat. Rev. Dis. Primer* **2018**, *4* (1), 1–22. https://doi.org/10.1038/nrdp.2018.10.

(12) Thomson, A. M.; et al., Global, Regional, and National Prevalence and Mortality Burden of Sickle Cell Disease, 2000–2021: A Systematic Analysis from the Global Burden of Disease Study 2021. *Lancet Haematol.* **2023**, *10* (8), e585–e599. https://doi.org/10.1016/S2352-3026(23)00118-7.

(13) Lee, L.; Smith-Whitley, K.; Banks, S.; Puckrein, G. Reducing Health Care Disparities in Sickle Cell Disease: A Review. *Public Health Reports®* **2019**, *134* (6), 599–607. https://doi.org/10.1177/0033354919881438.

(14) Johnson, K. M.; Jiao, B.; Ramsey, S. D.; Bender, M. A.; Devine, B.; Basu, A. Lifetime Medical Costs Attributable to Sickle Cell Disease among Nonelderly Individuals with Commercial Insurance. *Blood Adv.* **2022**, *7* (3), 365–374. https://doi.org/10.1182/bloodadvances.2021006281.

(15) Salinas Cisneros, G.; Thein, S. L. Recent Advances in the Treatment of Sickle Cell Disease. *Front. Physiol.* **2020**, *11*. https://doi.org/10.3389/fphys.2020.00435.

(16) Abraham, A. A.; Tisdale, J. F. Gene Therapy for Sickle Cell Disease: Moving from the Bench to the Bedside. *Blood* **2021**, *138* (11), 932–941. https://doi.org/10.1182/blood.2019003776.

(17) Brandow, A. M.; Liem, R. I. Advances in the Diagnosis and Treatment of Sickle Cell Disease. *J. Hematol. Oncol.J Hematol Oncol* **2022**, *15* (1), 20. https://doi.org/10.1186/s13045-022-01237-z.

(18) Johnson, K. M.; Jiao, B.; Ramsey, S. D.; Bender, M. A.; Devine, B.; Basu, A. Lifetime Medical Costs Attributable to Sickle Cell Disease among Nonelderly Individuals with Commercial Insurance. *Blood Adv.* **2023**, *7* (3), 365–374. https://doi.org/10.1182/bloodadvances.2021006281.

(19) Philippidis, A. CASGEVY Makes History as FDA Approves First CRISPR/Cas9 Genome Edited Therapy. *Hum. Gene Ther.* **2024**, *35* (1–2), 1–4. https://doi.org/10.1089/hum.2023.29263.bfs.

(20) Current and Future Treatments for Sickle Cell Disease: From Hematopoietic Stem Cell Transplantation to in Vivo Gene Therapy. *ResearchGate* **2025**. https://doi.org/10.1016/j.ymthe.2025.03.016.

(21) Homayun, B.; Lin, X.; Choi, H.-J. Challenges and Recent Progress in Oral Drug Delivery Systems for Biopharmaceuticals. *Pharmaceutics* **2019**, *11* (3), 129. https://doi.org/10.3390/pharmaceutics11030129.

(22) Hulbert, M. L.; Shenoy, S. Hematopoietic Stem Cell Transplantation for Sickle Cell Disease: Progress and Challenges. *Pediatr. Blood Cancer* **2018**, *65* (9), e27263. https://doi.org/10.1002/pbc.27263.

(23) Wong, E.; Godhamgaonkar, A.; McLornan, D. P. Principles of Haemopoietic Stem Cell Transplantation. *Medicine (Baltimore)* **2025**. https://doi.org/10.1016/j.mpmed.2025.02.012.

(24) Leonard, A.; Tisdale, J. F. A New Frontier: FDA Approvals for Gene Therapy in Sickle Cell Disease. *Mol. Ther.* **2024**, *32* (2), 264–267. https://doi.org/10.1016/j.ymthe.2024.01.015.

(25) bluebird bio. *A Phase 1/2 Study Evaluating Gene Therapy by Transplantation of Autologous CD34+ Stem Cells Transduced Ex Vivo With the LentiGlobin BB305 Lentiviral Vector in Subjects With Severe Sickle Cell Disease*; Clinical trial registration NCT02140554; clinicaltrials.gov, 2025. https://clinicaltrials.gov/study/NCT02140554 (accessed 2025-04-10).

(26) Singh, A.; Irfan, H.; Fatima, E.; Nazir, Z.; Verma, A.; Akilimali, A. Revolutionary Breakthrough: FDA Approves CASGEVY, the First CRISPR/Cas9 Gene Therapy for Sickle Cell Disease. *Ann. Med. Surg.* **2024**, *86* (8), 4555. https://doi.org/10.1097/MS9.0000000000002146.

(27) Agrawal, R. K.; Patel, R. K.; shah, V.; Nainiwal, L.; Trivedi, B. Hydroxyurea in Sickle Cell Disease: Drug Review. *Indian J. Hematol. Blood Transfus.* **2014**, *30* (2), 91–96. https://doi.org/10.1007/s12288-013-0261-4.

(28) Schneider, M. E. Thrown into Disarray | ASH Clinical News | American Society of Hematology.

(29) Lin, Y.; Li, H.; Dong, Y.; Fang, W.; Huang, H.; He, M.; Zhou, X.; Sun, N. A Retrospective Research of Adverse Event Reporting System Events for Voxelotor Based on the FAERS

Database. *BMC Pharmacol. Toxicol.* **2025**, *26* (1), 74. https://doi.org/10.1186/s40360-025-00915-1.

(30) Mast Therapeutics, Inc. *Evaluation of Purified Poloxamer 188 in Vaso-Occlusive Crisis of Sickle Cell Disease (EPIC): A Phase 3 Randomized, Double-Blind, Placebo-Controlled, Multicenter Clinical Trial of MST-188 (Purified Poloxamer 188) Injection in Subjects With Sickle Cell Disease Experiencing Vaso Occlusive Crisis*; Clinical trial registration NCT01737814; clinicaltrials.gov, 2016. https://clinicaltrials.gov/study/NCT01737814 (accessed 2025-04-10).

(31) Cieri-Hutcherson, N. E.; Hutcherson, T. C.; Conway-Habes, E. E.; Burns, B. N.; White, N. A. Systematic Review of L-Glutamine for Prevention of Vaso-Occlusive Pain Crisis in Patients with Sickle Cell Disease. *Pharmacother. J. Hum. Pharmacol. Drug Ther.* **2019**, *39* (11), 1095–1104. https://doi.org/10.1002/phar.2329.

(32) Ibrahim, A.; and Muhammad, S. A. Antioxidant-Rich Nutraceutical as a Therapeutic Strategy for Sickle Cell Disease. *J. Am. Nutr. Assoc.* **2023**, *42* (6), 588–597. https://doi.org/10.1080/27697061.2022.2108930.

(33) Guo, S.; Ren, Y.; Chang, R.; He, Y.; Zhang, D.; Guan, F.; Yao, M. Injectable Self-Healing Adhesive Chitosan Hydrogel with Antioxidative, Antibacterial, and Hemostatic Activities for Rapid Hemostasis and Skin Wound Healing. *ACS Appl. Mater. Interfaces* **2022**, *14* (30), 34455–34469. https://doi.org/10.1021/acsami.2c08870.

Chapter 2: Synthesis of Flavonoid-based Macromolecules: Antioxidant Therapy

2.1 Introduction

Oxidative stress in SCD has been a point of interest as a bio-marker for the diseases' progression and severity[1,2]. This is because polymerization of HbS, the hallmark of SCD is a direct cause of oxidative stress in SCD patients. Global oxidative stress markers, malondialdehyde (MAL) and advanced oxidation protein products (AOPP) have been reported at higher concentrations in SCD patients[3,4]. Oxidative stress occurs when there is an imbalance between the intracellular level of oxidizing species such as reactive oxygen species (ROS) and antioxidant activity. Under normal conditions, there is a balance between ROS and the body's defence system of antioxidants namely, molecules like superoxide dismutase, glutathione and catalase[1,5]. However, in sickle cell patients, the continual polymerization and depolymerization of HbS leads to the deficiency of the antioxidants typically formed in RBCs, mononuclear cells and platelets, resulting in high oxidative stress[2].

Oxidative stress also plays a central role in the pathophysiology of secondary complications associated with SCD, including hemolysis, vaso-occlusion, and organ damage. Studies have shown that reducing ROS levels in SCD patients significantly decreases the incidence of these downstream complications[5–7]. As a result, antioxidants such as N-acetylcysteine, L-glutamine, L-arginine, and zinc are commonly used as supportive therapies in SCD management. Of particular interest is the use of phytochemicals—also referred to as *nutraceuticals*, a term coined by Stephen DeFelice in 1989—which has gained traction due to their natural antioxidant properties and reduced risk of renal toxicity[8–10]. One nutraceutical, Jobelyn®, a sorghum bicolor leaf extract has been used in regions of West Africa as a dietary supplement to reduce vaso-occlusive crises and other complications associated with SCD. A study by Diaku-Akinwumi et al., demonstrated a significant decrease in oxidative stress markers 6 – 12 weeks from the start of Jobelyn® supplementation. This treatment was also

seen to increase the levels of hemoglobin. Interestingly, beyond the scope of SCD, Jobelyn® was shown to reduce inflammation and oxidative stress in animal models of rheumatoid arthritis[6,11].

Despite the efforts in the use of natural antioxidative therapy in managing disease complications, there are several setbacks. Particularly with low bioavailability and excessive antioxidative supplementation, with the latter potentially exacerbating the condition[12,13]. In addition, high antioxidant dosage can have pro-inflammatory effects and pose a risk to SCD patients who already experience chronic inflammation[5,14,15]. To address these limitations, this study was designed to develop polymeric materials derived from bioactive compounds in nutraceuticals that enable sustained release and prolonged antioxidant activity. Inspired by sorghum bicolor leaf extract (Jobelyn®), which contains multiple flavonoids as active constituents, we selected apigeninidin and apigenin as model compounds. These flavonoids were used to synthesize macromolecules that retained their antioxidant properties and exhibited extended activity in vitro. Additionally, Poly Lactic-co-Glycolic Acid (PLGA) microparticles incorporating the flavonoids were synthesized to study their release kinetics. The long-term goal of this work is to develop a microparticle-based drug delivery systems utilizing flavonoid-derived polymers for enhanced, sustained antioxidant therapy in SCD.

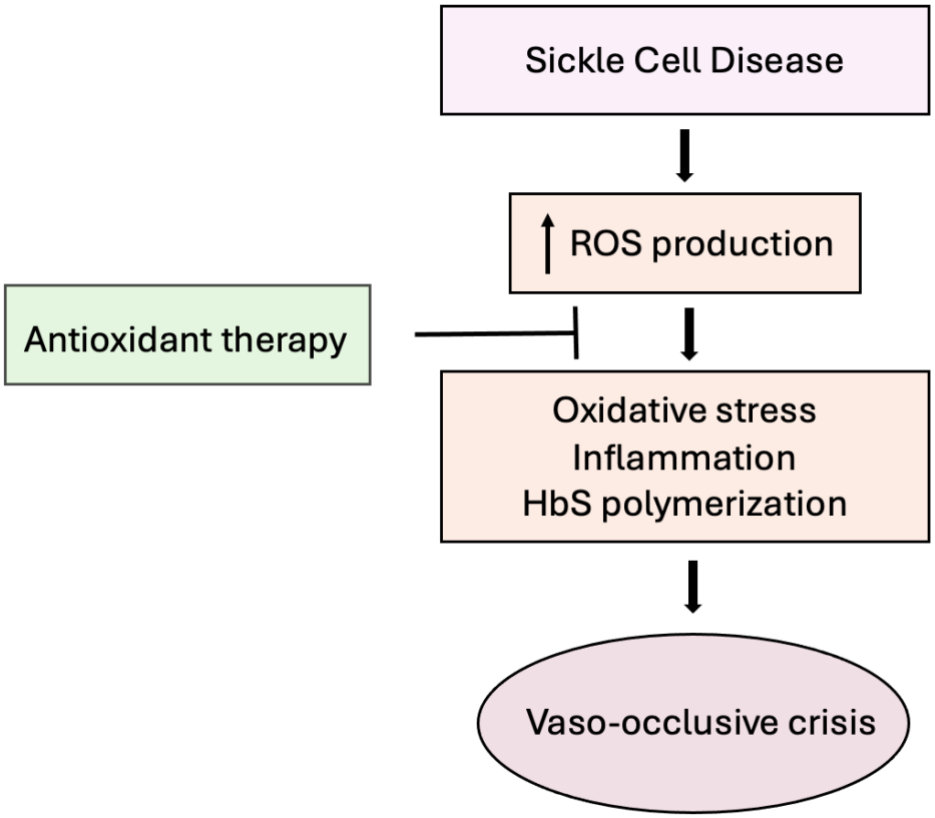

Figure 2. 1. Role of antioxidant therapy in SCD management[9].

2.2 Materials and methods

Jobelyn®, sorghum bicolor leaf extract obtained from Health Forever Products (Lagos, Nigeria), apigenin obtained from Xi'an NEO Biotech, methanol (Fisher, 99.8%), acryloyl chloride (Sigma, ≥ 97%), triethylamine (TEA, sigma, ≥ 99%), dichloromethane (DCM, Thermo Scientific, ≥99.5%), tetrahydrofuran (THF, Fisher Scientific, 99.9%), ethyl acetate (Fisher Scientific, 99.5%), hexanes (Fisher Scientific, 98.5%), methyl-3-mercarptopropionate (MMP, Fisher Scientific, 98%), pentaerythritol tetrakis (3-mercaptopropionate) (PETMP, Sigma Aldrich, 97%), adipoyl chloride (Acros organics, > 95%), sodium hydroxide (NaOH, Fisher Scientific, 97%), pyridine (Fisher Scientific, 99%), Poly(lactic-co-glycolic acid) (PLGA 50:50) (Sigma Aldrich), poly (vinyl) alcohol (Sigma Aldrich), sodium dodecyl sulfate (SDS, sigma Aldrich, 99%), 2,2'-azobisisobutyronitrile (AIBN, Sigma Aldrich, 98%), deuterated

solvents; chloroform-d, 99.8%, deuterium oxide, 99.8% and dimethyl sulfoxide-d6, 99.9% (Acros Organics)

2.2.1 Soxhlet extraction of apigeninidin from sorghum bicolor

To extract apigeninidin, 0.20 g sorghum bicolor was soxhlet extracted with 50 mL of refluxing methanol for 48 h. The typical yield of the extracted compound was 29.1%.

2.2.2 Interfacial polymerization of apigeninidin

Apigeninidin (0.48 g, 2.1 mmol) was dissolved in a 0.1 M solution of NaOH (5 mL) and stirred at room temperature for 5 minutes. A mixture of adipoyl chloride (0.3 ml, 2.1 mmol) in DCM (5 mL) was also prepared. To the adipoyl chloride mixture, apigeninidin solution was added slowly over a couple of minutes. The organic phase and aqueous phase were stirred to react at 450 rpm for 10 minutes. The product was then collected via vacuum filtration (0.62 g, 96%).

2.2.3 Condensation polymerizations of apigeninidin

Polycondensation reactions were performed by dissolving apigeninidin (0.01 g, 0.039 mmol) in 5 mL pyridine at 70 °C, then cooled to room temperature. Argon was bubbled through the solution to remove dissolved gases. Next, 1.5 equivalents of adipoyl chloride (8 μL, 0.059 mmols) was added directly into the reaction flask and left stirring for 24 hours. Purification was carried out by removing pyridine under vacuum, and triturating the resulting solids in cold 1M HCl water to remove residual pyridine and salts formed as a by-product. The product was then isolated by vacuum drying (0.005 g, 34%). These set of reactions were initially carried out in THF with the addition of triethylamine as a base. The reaction conditions were modified to improve the solubility of apigeninidin by switching the reaction solvent from THF to pyridine.

Due to the solubility of both interfacial and condensation polymers, proton nuclear magnetic resonance (^{1}HNMR) analysis was carried out on the polymers after soxhlet extraction in methanol. This was used to estimate functionalization and the molecular weight (MW) of the compounds.

2.2.4 Acrylation of apigenin

Apigenin (1.0 g, 3.7 mmol) was suspended in 5 mL THF and mixed with TEA (1.5 mL, 13 mmol). Acryloyl chloride diluted in 3 mL THF was then added dropwise into the reaction flask, over an ice bath. After dropwise addition, it was allowed to react overnight at room temperature. The resulting mixture was concentrated using a rotary evaporator, the remaining compound was then washed with deionized water by stirring for 5 hours. The product was isolated via freeze drying to yield a yellow powder (1.24 g, 80.7%). In order to separate mono-acrylated from di- and tri-acrylated compounds, the compound was further purified through column chromatography in 60:40 hexanes and ethyl acetate (35% yield). ^{1}H NMR spectra were recorded on Bruker AV-300 or Bruker AV-400 spectrometers at room temperature in $CDCl_3$. Chemical shifts are reported with respect to the internal solvent, 7.26 ppm ($CDCl_3$). NMR spectra shown in supplemental fig. 2.7. *^{1}H NMR (400 MHz, $CDCl_3$) δ = 7.90 (d, 2H, ArH), 7.43 (d, 1H, ArH), 7.31 (d, 2H, ArH), 6.96 (d, 1H, ArH), 6.63 (s, 1H, ArH), 6.67-6.09 (m, 9H, vinylic protons).*

2.2.5 Emulsion polymerization of apigenin acrylate

Emulsion polymerizations were performed in an aqueous environment. First, sodium dodecyl sulfate (SDS, 1.7 mg, 0.005 mmol) as an emulsifier was added to 1.5 mL water in a two-neck round bottom flask. Apigenin acrylate (280 mg, 0.5 mmol) dissolved in DCM was added to the flask and stirred at 800 rpm, 60 ℃ for 30 minutes. The reaction temperature was

set to 44 °C. Ammonium Persulfate (APS, 1.3 mg, 0.005 mmol) was added to the reaction, and it was left stirring overnight. The resulting compound was isolated via freeze-drying.

2.2.6 Free-radical polymerization of apigenin acrylate

Apigenin acrylate (250 mg, 0.6 mmol) and AIBN (0.94 mg, 0.006 mmol) were dissolved in 2 mL THF. The mixture was bubbled through with argon for 10 minutes and degassed with argon through 6 cycles of freeze-pump-thaw. The reaction solvent (THF) was dried under vacuum and the resulting solids were washed with cold water and isolated by freeze-drying.

2.2.7 Micheal addition with methyl-3-mercaptopropionate (Apigenin-MMP)

Apigenin-MMP was synthesized by dissolving apigenin acrylate (0.1 g, 0.25 mmol) in 5 mLDCM. Triethylamine (1 μL, 0.0073 mmol) was added directly to the reaction vessel, followed by MMP (81 μL, 0.73 mmol). The equivalents for this reaction were determined based on a 1:1 ratio of acrylates to thiols. The reaction was left to stir overnight at room temperature. The resulting solution was washed three times with an equal volume of brine, dried with magnesium sulfate and concentrated using a rotary evaporator (0.11 g, 65.7%).). ^{1}H NMR spectra were recorded on Bruker AV-300 or Bruker AV-400 spectrometers at room temperature in $CDCl_3$. Chemical shifts are reported with respect to the internal solvent, 7.26 ppm ($CDCl_3$). NMR spectra shown in supplemental fig. 2.8. *^{1}H NMR (400 MHz, $CDCl_3$) δ = 7.87 (d, 2H, ArH), 7.37 (d, 1H, ArH), 7.28 (d, 2H, ArH), 6.88 (d, 1H, ArH), 6.62 (s, 1H, ArH), 3.71 (s, 9H), 3.02-2.66 (m, 24H).*

2.2.8 Micheal addition with pentaerythritol tetrakis-3-mercaptopropionate (Apigenin-PETMP)

Apigenin-PETMP was synthesized using similar methods as described above. Apigenin acrylate (0.1 g, 0.25 mmol) was dissolved in 3 mL DCM. Triethylamine (0.25 µL, 0.0018 mmol) was then added directly to the reaction vessel, followed by PETMP (68.7 µL, 0.18 mmol). The equivalents for this reaction were also determined based on a 1:1 ratio of acrylates to thiols. The reaction was left to stir overnight at room temperature. The resulting yellow solid was dried using a rotary evaporator (0.25 g, 45.5%). Due to the insolubility of the reaction product, all analyses were carried out via IR spectroscopy.

2.2.9 Characterization of apigeninidin polymers

The synthesized apigeninidin polymers were also characterized via Fourier-Transform Infrared (FTIR) spectroscopy and Thermogravimetric analysis (TGA). These characterization techniques were chosen due to the insolubility of the polymers. IR spectroscopy was used to qualitatively determine phenol functionalization through -OH stretch disappearance and the appearance -COOH stretches. Thermal analysis was used to examine differences in the thermal characteristics of monomers and polymers. FTIR measurements were performed via the Attenuated Total Reflectance method using an FTIR spectrometer (Spectrum RX, PerkinElmer, Waltham, MA). TGA of the apigeninidin polymers where characterized by a thermogravimetric analyzer (TGA 8000, PerkinElmer, Waltham, MA) from 30 – 600 °C in an inert atmosphere and a heating rate of 10 °C/ min. Samples were weighed to approximately 2 mg for analysis.

2.2.10 Hydrolytic degradation of apigenin-thiol molecules

The hydrolysis of apigenin-MMP and apigenin-PETMP was evaluated using NMR and FTIR spectroscopy, respectively. Briefly, 0.02 g of each sample was placed in a scintillation

vial containing 2 mL of dPBS (pH 7.4). The samples were incubated at 37 ℃ and continuously agitated at 250 rpm using an MSC-100 thermo shaker incubator (Allsheng Instruments, China). At days 1, 4, 7, 14, and 30, the buffer solution was removed from each vial. The remaining solid and buffer solutions were freeze-dried and analyzed for mass loss and structural changes. Qualitative NMR analyses were performed on apigenin-MMP samples. Chloroform-d was used as the deuterated solvent, and 5 mM duroquinone was set as the internal standard. This was done using the capillary tube method to quantify changes in peak signal intensities. Apigenin-PETMP samples were qualitatively analyzed using IR spectroscopy due to its solubility limitations. The buffer solutions were also analyzed in D_2O[16].

2.2.11 Determination of antioxidant activity

DPPH (2,2-diphenyl-1-picryl-hydrazyl) assay was used to analyze the antioxidant activity of the synthesized flavonoid compounds. A DPPH methanolic solution (100 µL, 100 µM) was added to methanolic solutions of each sample (100 µL) at concentrations between 10 – 350 µM. After mixing, the samples were incubated for 30 minutes in the dark, and absorbance at 517 nm was measured using a BioMate 3S UV-visible spectrophotometer (Waltham, MA). The percent of DPPH scavenging activity was calculated using the following equation:

$$DPPH\ scavenging\ activity\ (\%) = \frac{A_0 - A_1}{A_0} \times 100 \qquad Eq.(1)$$

Where A_0 is the absorbance of the negative control (100 µL of methanol mixed in 100 µL of DPPH and maintained under the same conditions as samples) at 517 nm and A_1 is the absorbance of the samples. For apigeninidin samples known to absorb light around 517 nm, a blank correction method using the Beer's law was employed for calculations. A calibration curve of each apigeninidin-containing sample was made ranging between 5 – 200 µM.

This linear curve was used to determine the absorbance of the apigeninidin-containing samples at calculated concentrations. The exact concentration of the apigeninidin samples left over from the DPPH radical scavenging reaction was calculated using the equations below:

$$Absorbance\ (A) = \varepsilon * b * C \qquad Eq.(2)$$

$$\Delta A = Abs_{initial} - Abs_{final} \qquad Eq.(3)$$

$$\Delta[DPPH] = \frac{\Delta A}{\varepsilon * b} \qquad Eq.(4)$$

Where the change in DPPH concentration was estimated to be equivalent to the amount of antioxidant consumed in the reaction, based on a 1:1 stoichiometry[17]. A_1 for all apigeninidin-containing samples were normalized using the values calculated. IC_{50} values were estimated by linear regression and the assays were performed in triplicate[18].

2.2.12 Flavonoid-loaded microparticle synthesis and characterization

PLGA microparticles loaded with apigenin and apigeninidin were prepared using a modified emulsification-evaporation method[19,20]. Due to the high water solubility of apigeninidin, the microparticles were fabricated using a double emulsion (water-in-oil-in-water) technique. PLGA was first dissolved in DCM at a concentration of 150 mg/ml. Then, 100 µL of apigeninidin (20 mg/ml in deionized water) was added dropwise and the mixture was emulsified by sonication twice on ice at 90% amplitude for 10 seconds with a 10-second pause using a Sonics Vibra-Cell ultrasonicator (Newton, CT, USA). Next, 1 mL of apigeninidin at the same concentration, and 2 mL of 1% PVA were slowly added into the solution followed by another round sonication to form the final emulsion. The emulsion was then added to a solution containing 5 mL of apigeninidin (25 mg/ml) and 5 mL of 0.3% PVA, this was stirred at 350 rpm for four hours to allow solvent evaporation. The microparticles were isolated by

centrifugation at 10,000 rpm for five minutes, after which the supernatant was discarded and replaced with 10 mL of deionized water. This washing step was repeated twice before the particles were collected via freeze-drying. For apigenin-loaded microparticles, the same method was followed with minor modifications. Due to the lower water solubility of apigenin, a single emulsion (oil-in-water) technique was used. While all other conditions remained unchanged, apigenin was dissolved in hot ethanol at a concentration of 1.4 mg/mL before emulsification[21]. Calculated yields were 50% for apigeninidin-loaded particles and 85% for apigenin-loaded particles.

The encapsulation and loading efficiencies of the microparticles were also determined. First, 5 mg of loaded microparticles were dissolved in 2 mL acetone for apigeninidin particles or ethanol for apigenin particles, then sonicated at 37°C for 10 minutes. The amount of flavonoids encapsulated was quantified using a UV-vis spectrophotometer, with absorbance measurements converted to concentration using a standard curve[22]. The drug encapsulation efficiency and drug loading efficiency was calculated from equation 5 and 6.

$$Encapsulation\ Efficiency = \frac{W_t}{W_i} \times 100 \qquad Eq.(5)$$

$$Loading\ Efficiency = \frac{W_x}{W_y} \times 100 \qquad Eq.(6)$$

Where W_t is the total amount of incorporated material, W_i is the total amount of material added during microparticle preparation (polymer + drug), W_x is the amount of encapsulated drug and W_y is the amount of drug used for preparation in the microparticle. Furthermore, to measure the average size, zeta potential and polydispersity index, the microparticles was analyzed using a Zetasizer Nano ZS (Malvern, UK). The samples were dispersed in 5 mM NaCl solution and examined at room temperature. Each sample was kept at a concentration of 1 mg/ml and scanned in triplicates.

2.2.13 Release of flavonoids from PLGA microparticles

In vitro release experiments were conducted at 37℃ to evaluate the kinetics of flavonoid release. Flavonoid-loaded microparticles (1 mg) were suspended in 2 mL of PBS (pH 7.4) and incubated on a thermoshaker at 200 rpm. At predetermined time points (1 hr, 4 hr, 24 hr, 48 hr, 72 hr, and 124 hr), samples were centrifuged at 4000 rpm for five minutes, and the supernatant was collected for analysis using a UV-visible spectrophotometer. Absorbance measurements were taken at 410 nm for apigeninidin and 336 nm for apigenin. For apigenin analysis, the samples were freeze-dried and redispersed in ethanol prior to measurement. Standard curves of apigeninidin in PBS and apigenin in ethanol were used to quantify flavonoid release from the microparticles. Each time point included a blank microparticle control, and all experiments were performed in triplicate[23,24]

2.3 Results and discussion

2.3.1 Extraction of apigeninidin and synthesis of apigenindin polymers

Sorghum bicolor contains several phytochemicals, including apigeninidin, luteolinidin, and naringenin, with apigeninidin being the most abundant[25,26]. After the soxhlet extraction of sorghum bicolor, electrospray ionization mass spectrometry (ESI-MS) analysis confirmed that apigeninidin was the sole compound present (**Fig S.1**). Apigeninidin contains phenolic groups that provide reactive sites for polymerization[27–29]. Specifically, we are interested in the incorporation of ester linkages which would introduce hydrolytically cleavable bonds. This allows for tunable and potentially prolonged activity based on the degradation rate of the polymer. Extracted apigeninidin was used for the synthesis of interfacial and condensation polymers as shown in **scheme 2.1**.

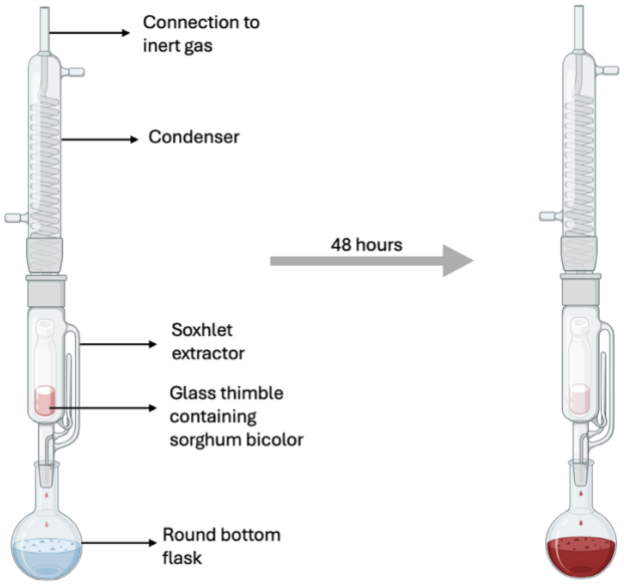

Figure 2. 2. Graphical representation of the setup used for soxhlet extraction (created with BioRender)

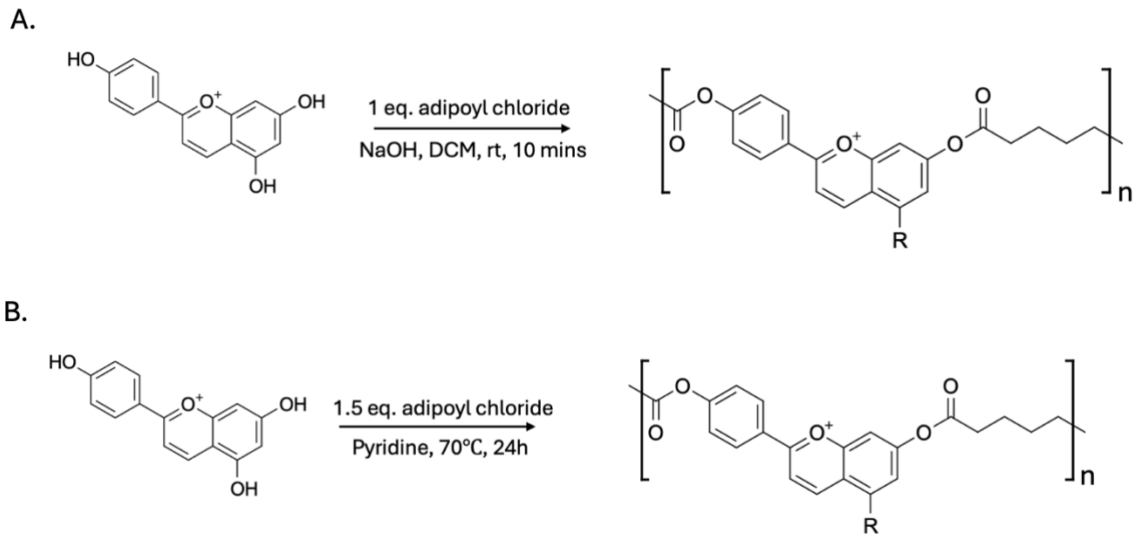

Scheme 2. 1. A) Interfacial polymerization of apigeninidin. B) Condensation polymerization of apigeninidin. The R group represents attachment of an adipoyl chloride spacer.

2.3.2 Characterization of apigeninidin polymers

The synthesized polymers were structurally characterized through ^{1}HNMR and FTIR spectroscopy. Due to the limited solubility of the polymers, soxhlet extraction with methanol

was performed to isolate a soluble fraction for analysis. ^{1}HNMR spectra revealed aromatic proton signals consistent with the native apigeninidin structure (**Fig S2.2 – 2.4**). To estimate the molecular weight, the integrals of the aromatic peaks were compared to those of the aliphatic four-carbon chain from the adipoyl chloride spacer. Particularly, the C3 and C4 protons of apigeninidin were used as reference peaks due to their prominence in the proton NMR spectrum (**Fig 2.3**). The interfacial polymer (IP) had an estimated molecular weight of 1716 g/mol, while the condensation polymer (CP) was estimated at 1351 g/mol. It is likely that higher molecular weight species remained insoluble and were not captured in this analysis, suggesting the presence of larger, more complex polymeric structures. Further analysis of these fractions can be done using techniques like Matrix-Assisted Laser Desorption/Ionization Time-of-Flight Mass Spectrometry (MALDI-TOF-MS)[30,31]. It is also important to note that two of the four condensation polymers could not be analyzed by ^{1}HNMR due to the absence of characteristic apigeninidin aromatic peaks, even after Soxhlet extraction. This may be attributed to low functionalization or the presence of predominantly unreacted starting materials and reagents.

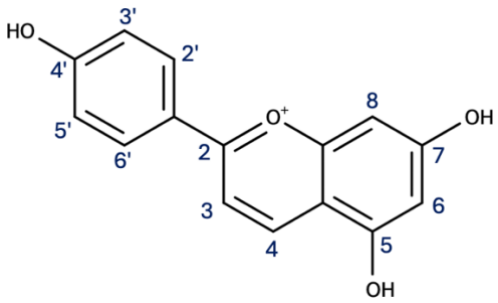

Figure 2. 3. Atom numbering of apigeninidin

To further characterize the samples, FTIR analysis was performed. IR spectra of flavonoids such as apigeninidin have a characteristic broad peak at 3200-3428 cm^{-1} representing the phenolic-OH groups[32]. As shown in **Fig 2.4**, the synthesized polymers displayed little to no peaks around the 3200-3428 cm^{-1} region, indicating partial or total

functionalization of the phenolic groups. A distinct increase in peaks between 2850-3000 cm^{-1} suggests the successful incorporation of sp^3-hybridized aliphatic groups from the adipoyl chloride spacer. Furthermore, the emergence of peaks between 1715-1730 cm^{-1} which is absent in the monomer, suggests the formation of ester bonds across all polymer samples. Overall, these results are consistent with ^{1}HNMR data confirming the functionalization of apigeninidin. Finally, thermogravimetric analysis was performed for all apigeninidin samples. The thermal stability of apigeninidin and apigeninidin polymers were assessed. Specifically, the temperature at which 25% weight loss occurred was calculated as shown in **Table 2.1**. A 25% weight loss threshold was selected for TGA analysis to capture early-stage degradation behavior, including partial thermal decomposition and the evaporation of residual volatile compounds from the synthesis process. We observed that native apigeninidin degraded at 334 °C, while functionalized apigeninidin polymers exhibited degradation temperatures ranging from 201–300 °C. These results indicate that in an inert atmosphere, polymer functionalization does not significantly affect thermal stability (**Fig S2.5**).

Table 2. 1. Showing the temperature at which 25% of each material is degraded

Sample	25% weight loss
Apigeninidin	334 ℃
AE-CP 55.2	201 ℃
AE-CP 61.2	300 ℃
AE-CP 81.2	280 ℃
AE-IP 104.1	295 ℃

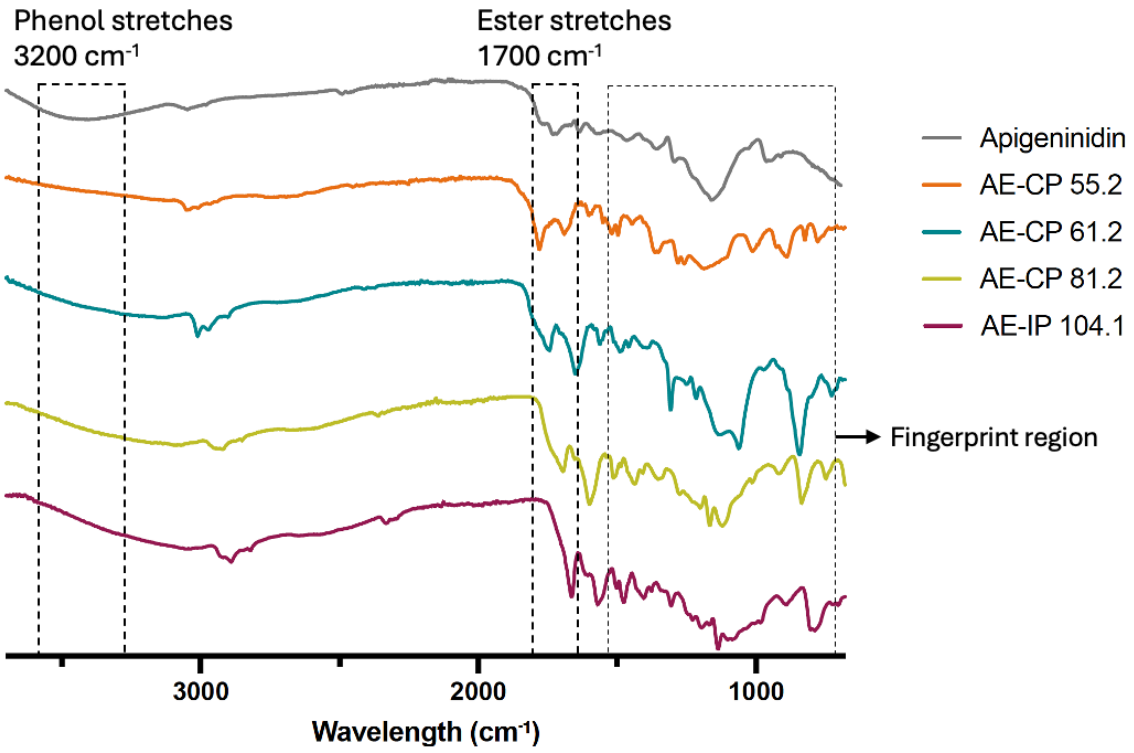

Figure 2. 4 Stacked IR spectra of apigeninidin and apigeninidin polymers. IP stands for interfacial polymer and CP stands for condensation polymer.

2.3.3 Utilizing click chemistry in the synthesis of apigenin-thiol molecules

Prior to synthesizing the apigenin-thiol molecules, we attempted emulsion and free-radical polymerizations of apigenin acrylate These reactions were unsuccessful, likely due to the presence of phenol groups on partially "acrylated" apigenin molecules that can scavenge the free radicals formed during the reaction. To overcome this challenge, we separated the di- and tri-acrylated apigenin molecules using an hexanes and ethyl acetate column chromatography (60:40 v/v). The di- and tri-acrylated fractions were re-subjected to the same reaction conditions. Despite these efforts, polymerization remained unsuccessful. However, these limitations led to a new approach, the development of thiol-acrylate Michael reactions. Thiol-Michael reactions are referred to as prized tools in materials chemistry because of their modular "click" nature which stems from fast kinetics and high yields[33]. In respect to this work,

the synthesis of highly functionalized molecules with hydrolytically cleavable groups makes this chemistry particularly desirable and it overcomes the polymerization limitations we faced with partially acrylated compounds. The apigenin-thiol molecules were synthesized following a two-step reaction that involved acrylation of apigenin and subsequent thiol-michael addition (**scheme 2.2**). The thiol-michael additions were performed using two thiol molecules. The first molecule being MMP and the second, PETMP, a larger molecule containing four 3-mercarptopropionate groups (**scheme 2.3**). The synthesized molecules, apigenin-MMP and apigenin-PETMP were analyzed via ^{1}HNMR spectroscopy and FTIR spectrometry respectively (**Fig S2.7 - 2.9**). Due to the high functionality of apigenin-PETMP samples, we observed solubility limitations making IR analysis one of the most suitable characterization techniques. The IR spectra of apigenin-PETMP showed loss of the phenolic-OH stretch around 3200 cm^{-1}, the appearance of a thioether and an ester stretch around 698 cm^{-1} and 1700 cm^{-1} respectively, suggesting the formation of the product[34,35] (**Fig S2.9)**.

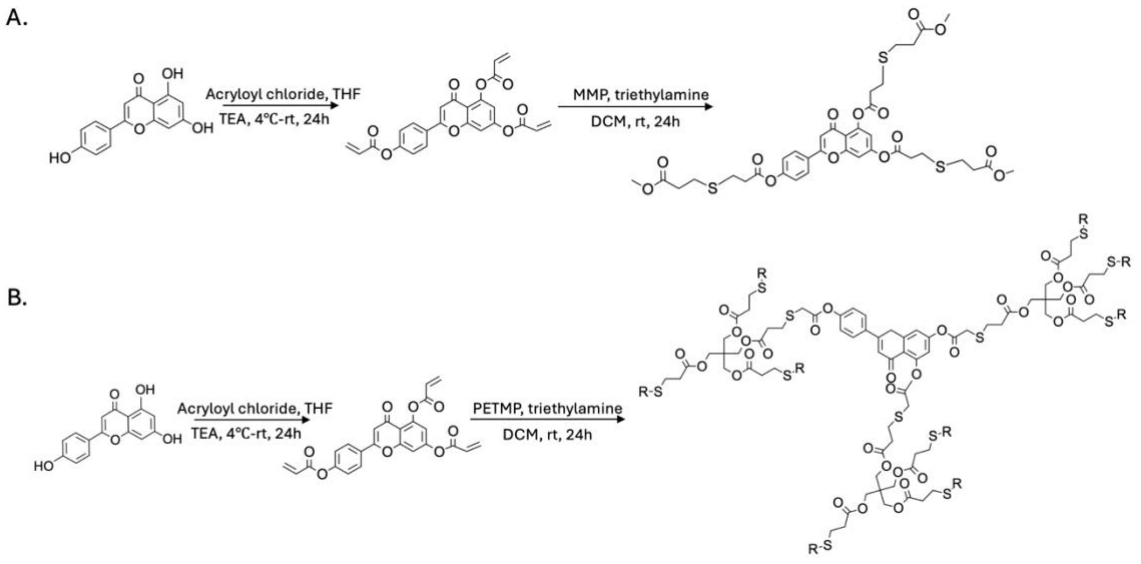

Scheme 2. 2. Two-step synthesis scheme for apigenin-thiol molecules. A) Apigenin-MMP and B) Apigenin-PETMP. *Where MMP is methyl-3-mercaptopropionate; PETMP is pentaerythritol tetrakis-3-mercaptopropionate; R represents the apigenin moiety.*

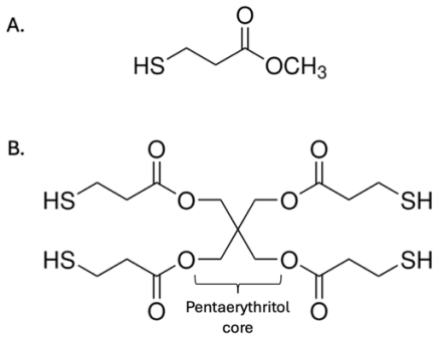

Scheme 2. 3. Showing the structural differences between MMP and PETMP. PETMP contains four methyl-3-mercaptopropionate groups connected by a pentaerythritol core.

2.3.4 Sustained release of apigenin: hydrolytic degradation studies

The hydrolysis-driven release study of apigenin from the apigenin-thiol molecules was performed at 37°C in PBS and with agitation, to simulate physiological conditions. At pre-determined time points, the various samples were analyzed using ^{1}HNMR for apigenin-MMP samples and FTIR for apigenin-PETMP samples. In ^{1}HNMR analysis, degradation was quantified by monitoring the reversion of apigenin-MMP to apigenin using the 'x' peak labeled in **Fig 2.5**. The 'x' peak which corresponds the phenolic-OH group attached to the 4′-position of the B-ring in the apigenin structure. This peak was selected due to its prominence and stability across all apigenin samples, with no observed overlaps. In contrast, peaks 'a-e'which correspond to the aromatic region of apigeninidin showed variability in peak area and overlapped with signals from apigenin-MMP. As a result, they could not be reliably used for accurate analysis. (**Fig 2.5**). Degradation was calculated using Equations 7 and 8 and normalized to day 0.

$$Degradation = \frac{peak\ area\ (peak'x')}{total\ area\ i.e.\ integration\ if\ there\ was\ 100\%\ deg.} \times 100 \qquad Eq.(7)$$

$$Normalized\ degradation = \frac{deg.at\ day\ 1,4\ or\ 7 - \text{deg.}\ at\ day\ 0}{deg.at\ day\ 0} \times 100 \qquad Eq.(8)$$

At days 4, 7, 14, and 30, we observed 15.6 %, 28.1 %, 40.6 %, and 31.3 % degradation, respectively (**Table 2.2**). There was no observed degradation on day 1. Surprisingly, the calculated degradation at day 30 was lower than at day 14. Although this was unexpected, it may indicate that hydroylsis of the ester group used for degradation calculations reaches a plateau after 14 days (that is; the COOH group attached to the 4′-position of the B-ring in the apigenin structure). This also suggests that the 30-day hydrolysis data likely reflects cleavage of only one of the three ester groups in the apigenin-MMP structure, indicating that more detailed quantification will require ^{1}HNMR peak deconvolution.

Table 2. 2. Showing the hydrolytic degradation of apigenin-MMP in respect to the integral of 'x' peak

Timepoint	Deg. using peak x (%)	Normalized deg. using peak x (%)
Day 1	32	0
Day 4	37	15.6
Day 7	41	28.1
Day 14	45	40.6
Day 30	42	31.3

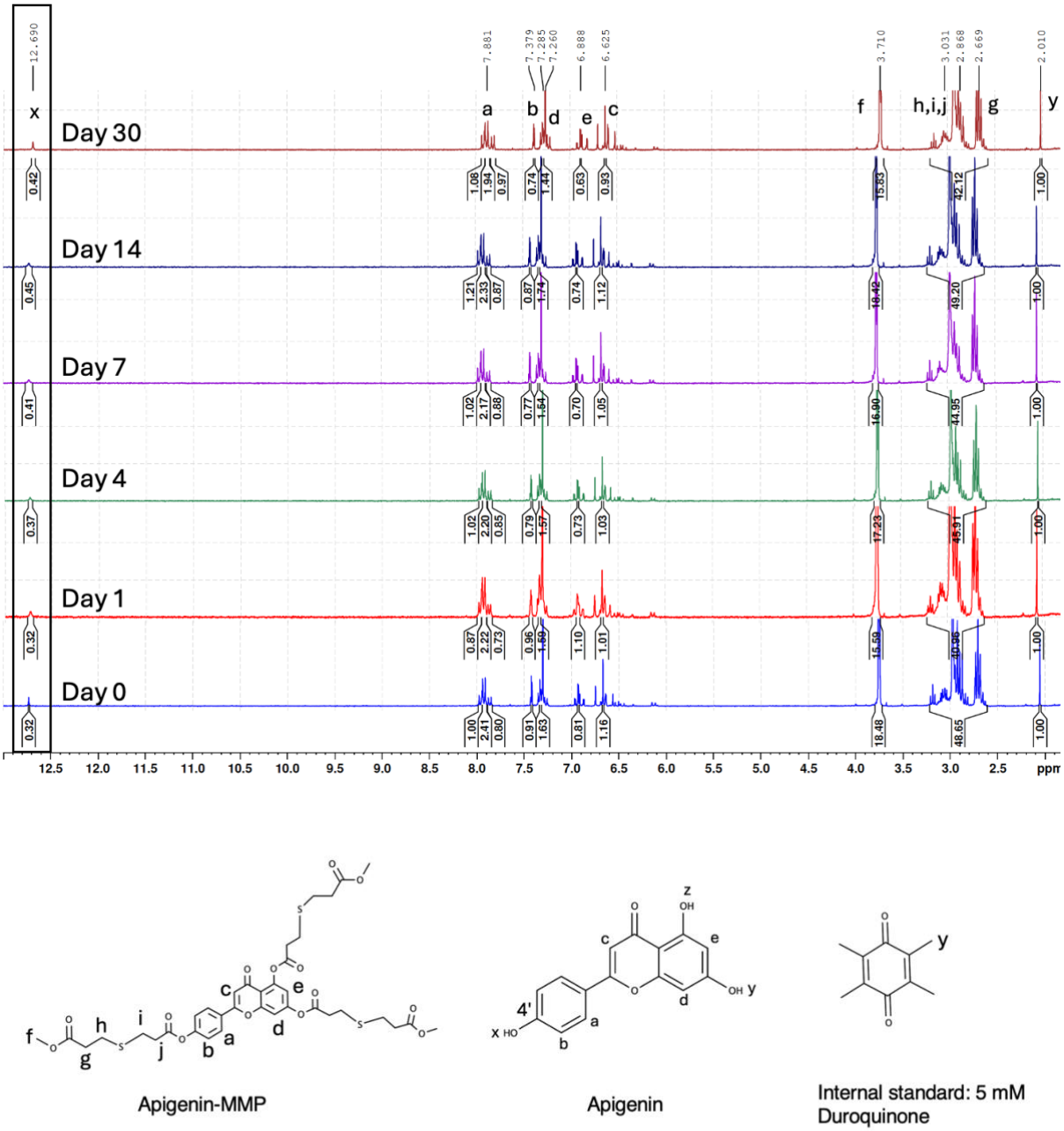

Figure 2. 5. Stacked ^{1}HNMR spectra of apigenin-MMP after a 30-day incubation in PBS at 37 °C. The phenol peak of apigenin labeled 'x' in the box was used to calculate hydrolytic degradation.

Qualitative FTIR analysis of apigenin-PETMP samples also indicate hydrolysis. We observed the emergence of phenol stretches in incubated samples, with the most prominent phenol-OH band observed at day 30 (**Fig 2.6**). These results align with the future objectives of

this work, demonstrating that the synthesized apigenin-thiol molecules may enable sustained release of apigenin. This approach can be further developed into a particulate delivery system using our established synthesis.

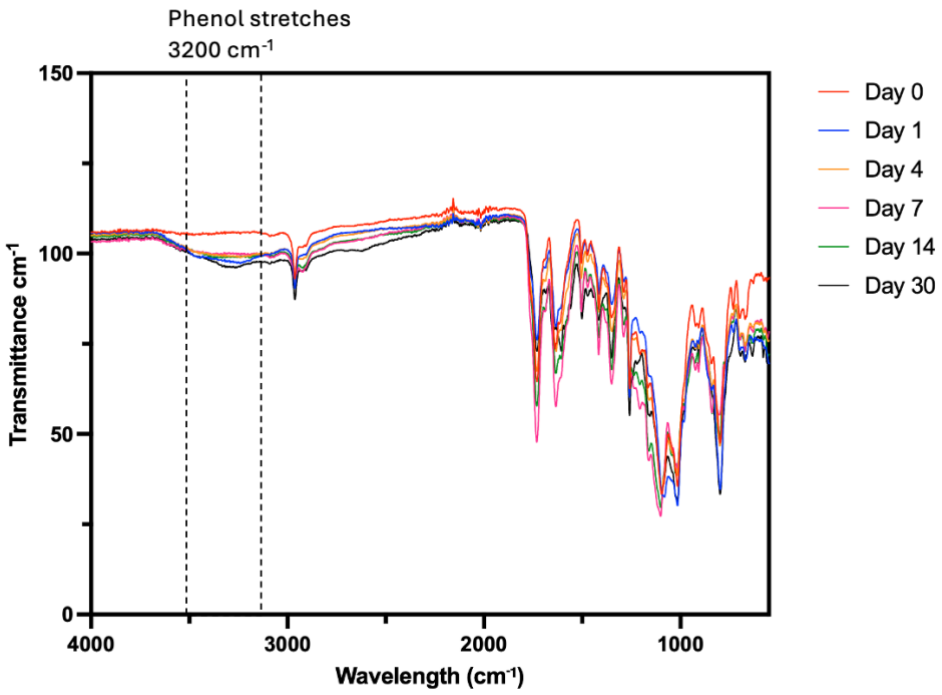

Figure 2. 6. Stacked FTIR spectra of apigenin-PETMP after a 30-day incubation in PBS at 37 °C, showing the appearance of broad phenol bands in relation to time change.

2.3.5 Characterization of flavonoid-loaded PLGA microparticles

Dynamic Light Scattering (DLS) and encapsulation efficiency experiments were performed to evaluate the behavior of the flavonoids as drugs in a microparticle drug delivery system. The results will be useful as a control for future studies with microparticles synthesized from flavonoid-based polymers. Encapsulation and loading efficiencies were calculated using equations (4) and (5). Apigenin-loaded and apigeninidin-loaded MPs exhibited low encapsulation efficiencies of 6% and 4%, respectively, with corresponding loading efficiencies of 22% and 17%. This may be attributed to the low encapsulation often observed between PLGA microparticles and hydrophilic drugs[36,37]. Despite the low incorporation, these findings

show that incorporation of the flavonoids into a synthetic polymer requires further optimization, and may not be ideal. This supports our rationale for synthesizing microparticles using flavonoid-derived polymers in future studies. The hydrodynamic size and polydispersity index (PDI) were obtained from DLS analysis. The mean particle sizes of the loaded microparticles were between 1.9 μM and 2.4 μM. The PDI was between 0.9 to 1 indicating polydisperse samples (**Table 2.3**). Considering their intended application, these sizes are particularly favorable. In the context of SCD, the primary targets for mitigating oxidative stress are the circulatory system and the spleen, an organ that plays a central role in filtering damaged red blood cells and modulating immune responses. Intravenous delivery of microparticles within the 0.2-3 μm range has been shown to preferentially promote spleen accumulation, making this size distribution promising for targeted delivery in SCD therapy. These findings suggest that the developed system has potential for future *in vivo* applications aimed at reducing oxidative damage[38,39]

Table 2. 3. The hydrodynamic size and polydispersity index for the various PLGA microparticle formulations

Formulation	Hydrodynamic size (μM)	PDI
Blank PLGA microparticles	0.94 ± 0.07	0.67 ± 0.05
Apigenin-PLGA microparticles	2.40 ± 0.20	1
Apigeninidin-PLGA microparticles	1.90 ± 0.05	0.98 ± 0.03

2.3.6 In vitro release

Figure 2.7 A & B show the *in vitro* release profiles of apigenin and apigeninidin from PLGA microparticles over a five day period. To account for simultaneous degradation of the PLGA carrier, each sample was centrifuged to separate the microparticles from the released drug. Measurements were then normalized using blank microparticle controls[40,41]. Apigenin showed an initial burst release, with the majority of the compound released in the first 24 hours,

followed by a plateau, indicating limited sustained release. In contrast, apigeninidin displayed a more gradual release profile, with approximately 39% cumulative release, suggesting more controlled release kinetics. Interestingly, this phenomenon may be attributed to differences in loading efficiency, with apigenin-loaded microparticles exhibiting burst release corresponding to their higher loading efficiency. A similar trend was reported in PLA microspheres, where a 30% increase in drug loading resulted in significantly accelerated release kinetics[42]. Overall, the observed release profiles highlight the need for further optimization of the microparticle synthesis process for both apigenin and apigeninidin formulations. While the current systems have potential, the release duration falls short of our ideal therapeutic window. A cumulative release over 5-7 days would be preferred to maximize drug availability before clearance from the bloodstream[43].

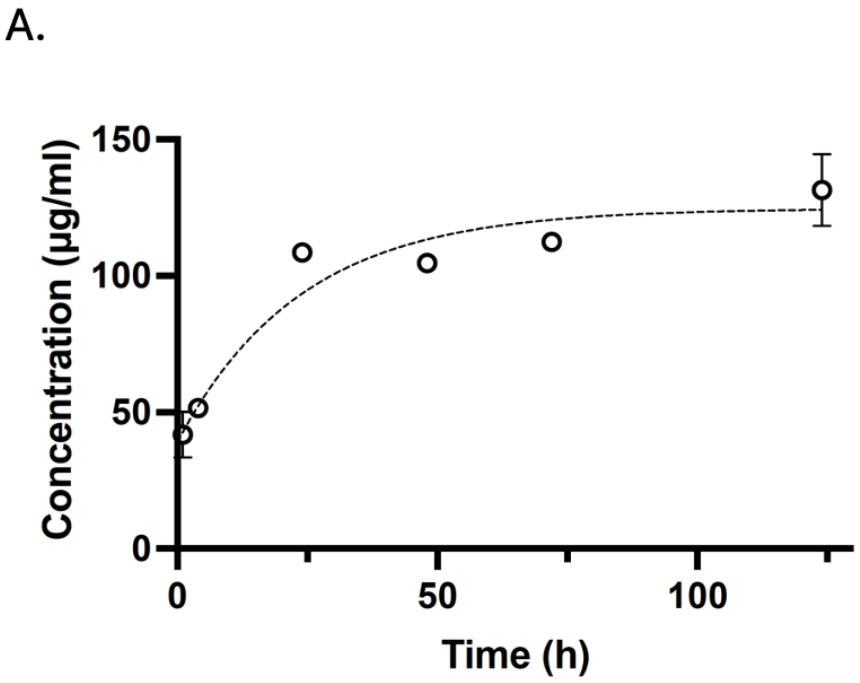

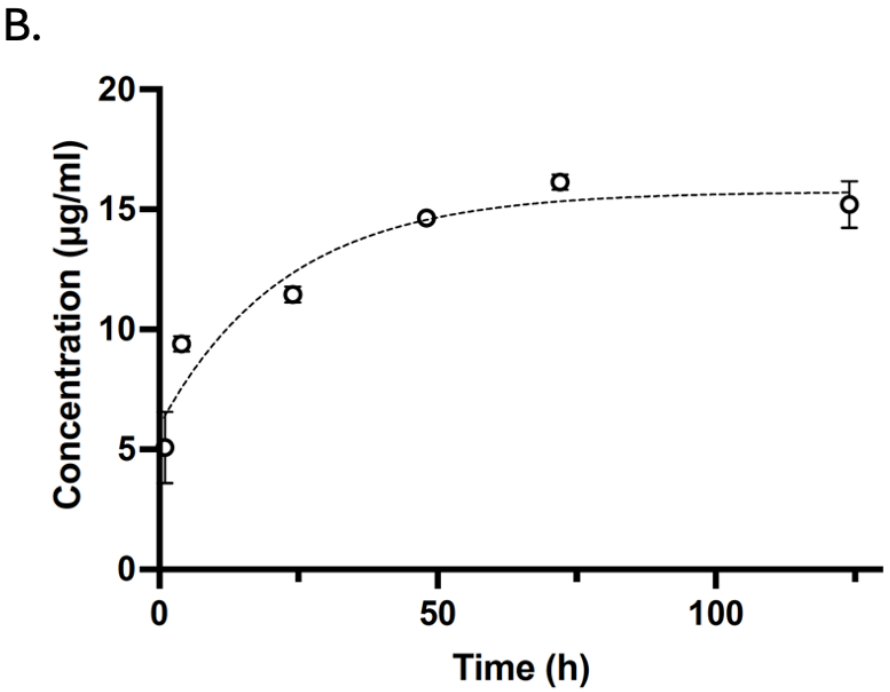

Figure 2. 7. *In vitro* release profiles of A) apigenin and B) apigeninidin. Concentrations were determined using a standard curve.

2.3.7 Antioxidant activity of flavonoid polymers and complexes

A key objective of this study was to synthesize flavonoid-based molecules that retain their ability to scavenge free radicals while enabling sustained antioxidant activity *in vivo*. To evaluate this, a DPPH free radical scavenging assay was performed[44]. After a 30-minute incubation, apigeninidin polymers exhibited IC_{50} values (the concentration required to scavenge 50% of DPPH radicals) ranging from 81.3-269 µM (**Table 2.4**). For comparison, melatonin, a well-known antioxidant, has reported IC_{50} values between 75 and 200 µM, suggesting that our synthesized polymers exhibit comparable antioxidant efficacy[45,46]. We also observed that the IC_{50} value of non-polymerized apigeninidin was lower than that of the polymerized apigeninidin. This difference correlates with the estimated molecular weights of the apigeninidin polymers, where higher molecular weight polymers generally displayed higher IC_{50} values (**Table 2.5).** This trend suggests that increased polymerization reduces the

availability of functional groups responsible for radical scavenging. Particularly, FTIR analysis showed loss of functional groups like phenolic-OH groups that scavenge radicals, confirming this idea. This observation aligns with findings in other studies. For instance, research on chitosan gallate derivatives demonstrated that lower molecular weight samples had significantly lower IC_{50} values in DPPH assays, indicating higher antioxidant activity[47,48]. Furthermore, this supports the idea of a delayed-release antioxidant system, where antioxidant activity can increase as more apigeninidin is released *in vivo*. Additionally, a trend of increasing scavenging activity was observed as concentration increased (**Fig 2.8**)

For apigenin-thiol molecules, we observed little to no scavenging activity on functionalized molecules after 30 minutes. However, scavenging activity was tested on samples that were used in hydrolytic degradation studies, specifically day 0, day 4, day 14 and day 30 samples. Here, we saw that scavenging activity increased as more hydrolysis occurred (**Fig 2.9**). This activity was also observed to increase as a function of time. Apigenin-PETMP samples had higher % scavenging over time when compared to apigenin-MMP samples. The results from both flavonoid complexes suggest that they can be used to facilitate controlled antioxidant activity.

Table 2. 4. IC_{50} values of apigeninidin and apigeninidin polymers. Ascorbic acid was used as the standard. IP stands for interfacial polymer and CP stands for condensation polymer.

Samples	**IC_{50} (uM)**
Ascorbic acid	11.3[49]
Apigeninidin	58
AE-CP 55.2	81.3
AE-CP 61.2	132
AE-CP 81.2	67.8
AE-IP 104.1	269

Table 2. 5. Estimated molecular weight of polymers based on NMR analysis. IP stands for interfacial polymer and CP stands for condensation polymer.

Polymers	Estimated molecular weight (g/mol)	IC_{50} value (radical scavenging)
AE-IP 104.1 (interfacial polymer)	1716	269
AE-CP 61.2 (condensation polymer)	1351.3	132
AE-CP 55.2 (condensation polymer)	-	67.8
AE-CP 81.2 (condensation polymer)	-	81.3

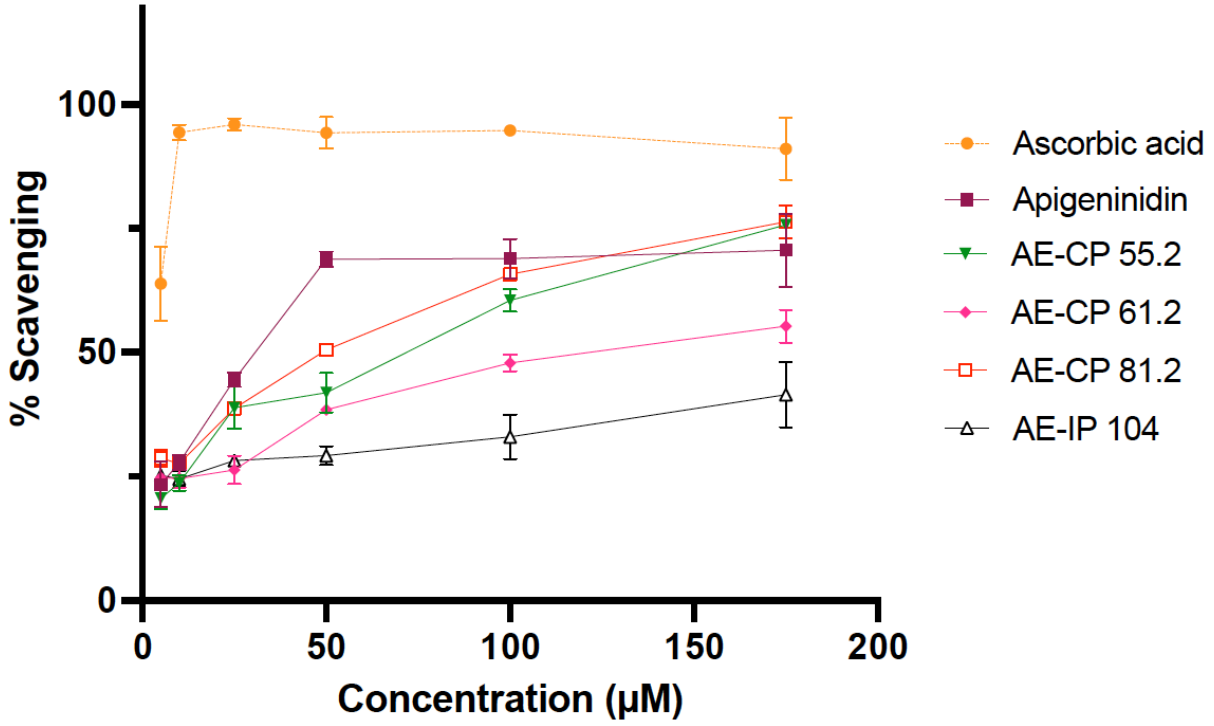

Figure 2. 8. Radical scavenging activity of apigeninidin and apigeninidin polymers. Ascorbic acid and unconjugated apigeninidin were set as the standard (control).

Finally, we observed that non-functionalized apigenin had low scavenging activity, with concentrations of 175 μM scavenging about 35% of DPPH radicals. A study

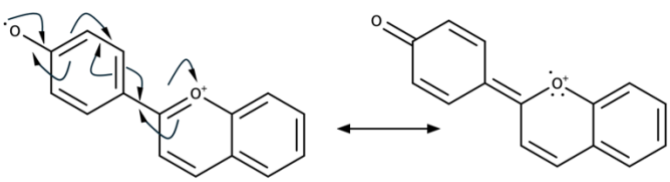

Scheme 2. 4. Proposed scheme for resonance stabilization of apigeninidin radicals[51].

by Tian *et al.* showed that apigenin had a lower scavenging activity when compared to other natural antioxidants like luteolin and quercetin because of a smaller amount of enol groups on apigenin's structure[50]. However, since apigenin and apigeninidin have an equal amount of enol groups, we hypothesize that the differences we observed may be due to the cation on apigeninidin structure which can facilitate resonance stabilization during the scavenging process[51].

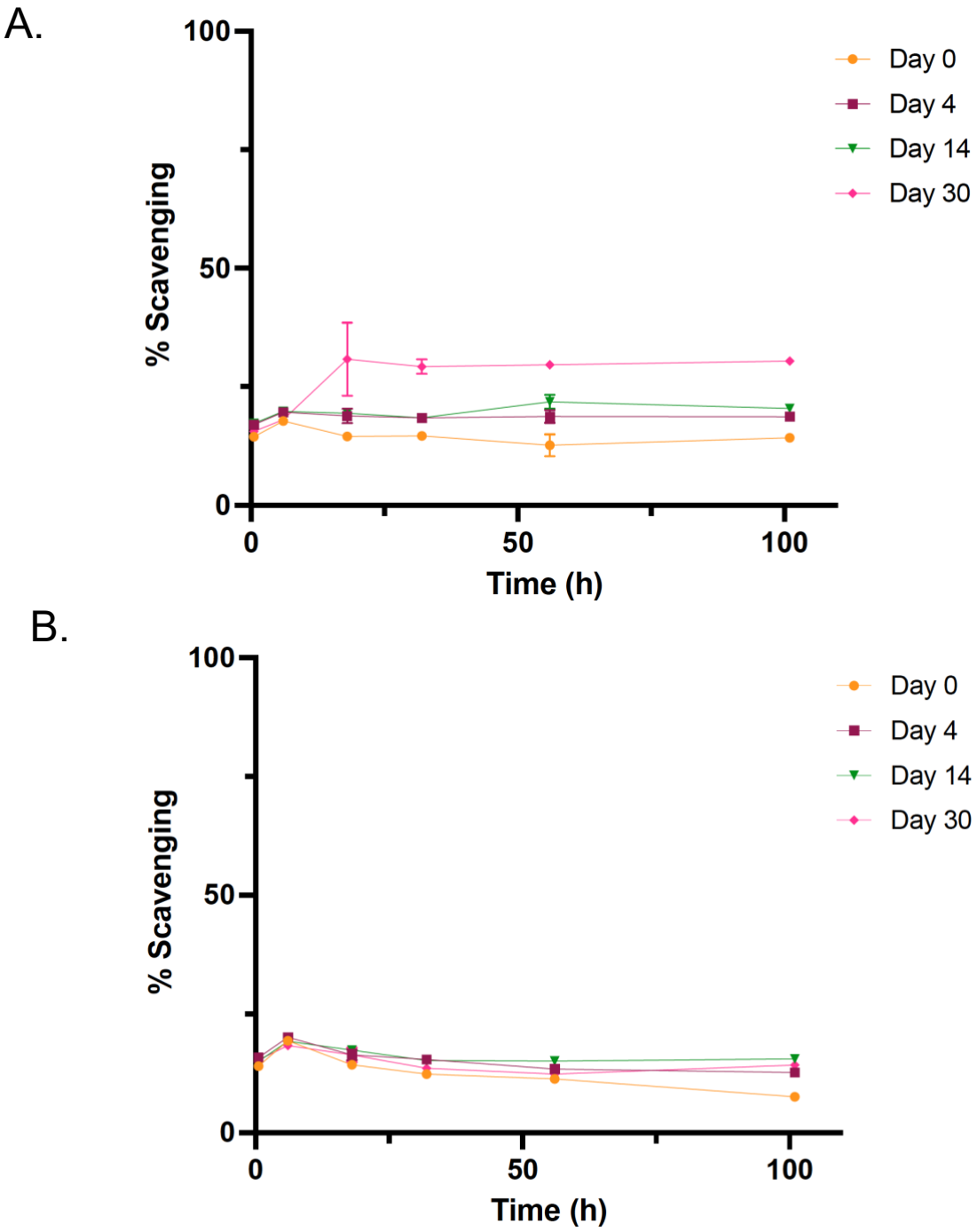

Figure 2. 9. Radical scavenging activity of apigenin-thiol molecules over time and hydrolysis duration**.** A) Apigenin-PETMP and B) Apigenin-MMP. “Day 0” to “Day 30” refer to timepoints collected during hydrolysis studies.

2.4 Conclusions

This work demonstrates the successful synthesis of flavonoid-based polymers and macromolecules capable of sustained antioxidant activity in vitro. This activity is influenced by both molecular size and the rate of hydrolytic degradation. Additionally, the synthesized microparticles fall within the optimal range for spleen-targeted delivery via intravenous administration-an important consideration for oxidative stress management SCD. These findings provide a strong foundation for future studies focused on engineering delivery systems from these bio-active polymers. Such systems offer a promising alternative to oral antioxidant supplements in SCD, potentially overcoming challenges related to low bioavailability and risks associated with excessive supplementation.

2.5 Supplemental Information

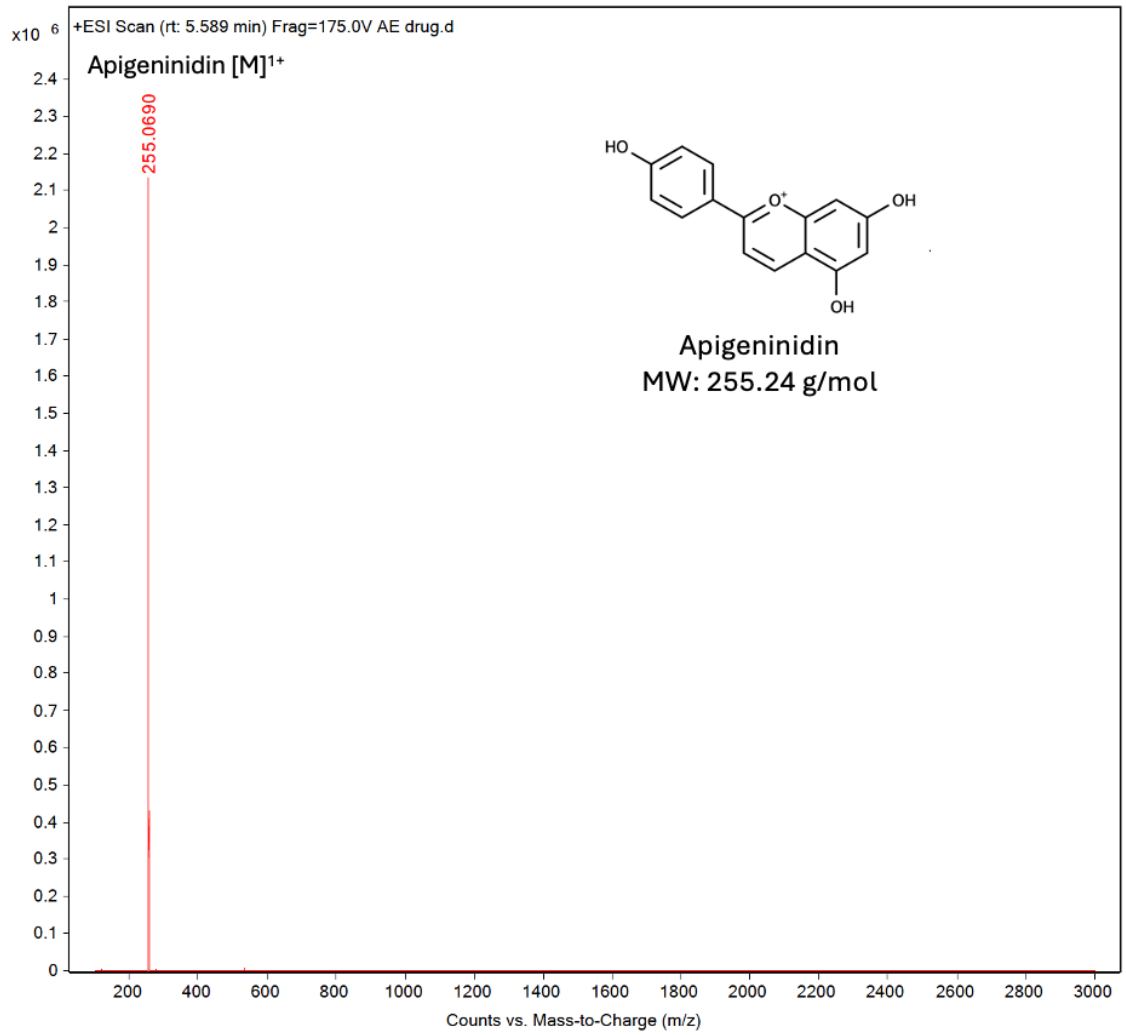

Figure S2.1. ESI-MS of soxhlet extracted sorghum bicolor

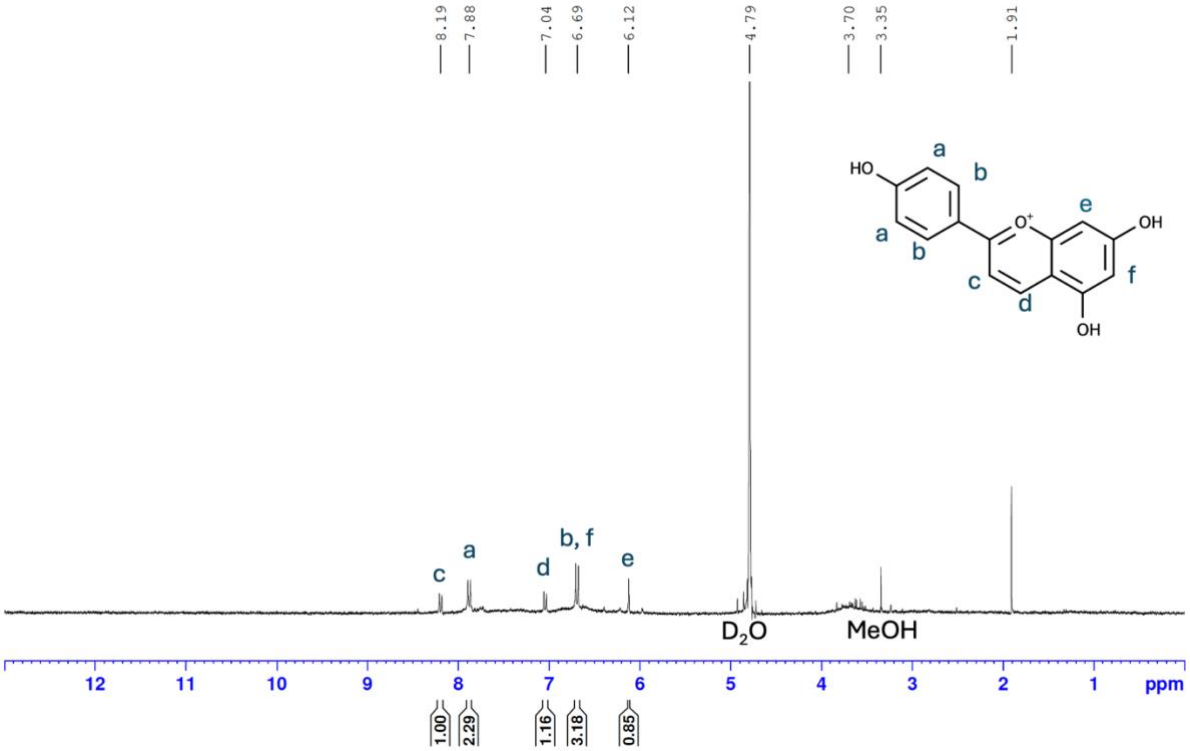

Figure S2.2. [1]HNMR spectra of soxhlet-extracted apigeninidin

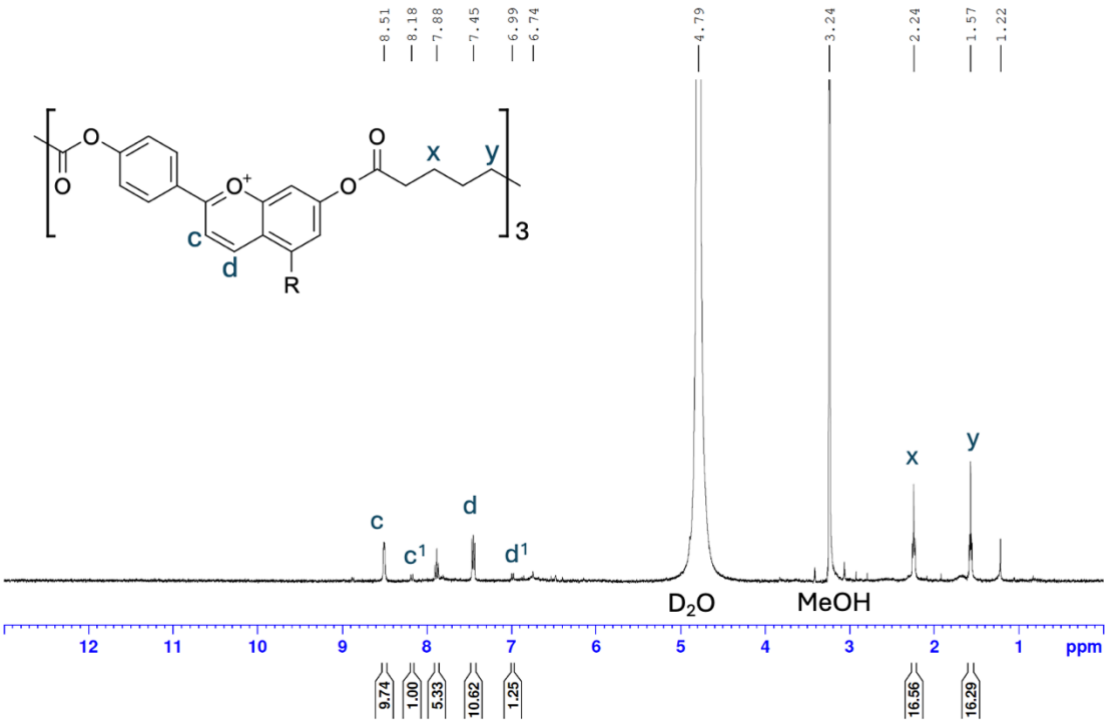

Figure S2.3. [1]HNMR spectra of apigeninidin interfacial polymer (AE-IP 104.1) after a soxhlet extraction. Where c^1 and d^1 were labeled using native apigeninidin NMR spectra. Both peaks represent apigeninidin peaks from the end of the polymer chain where no functionalization occurred. c^1 was set as the reference peak.

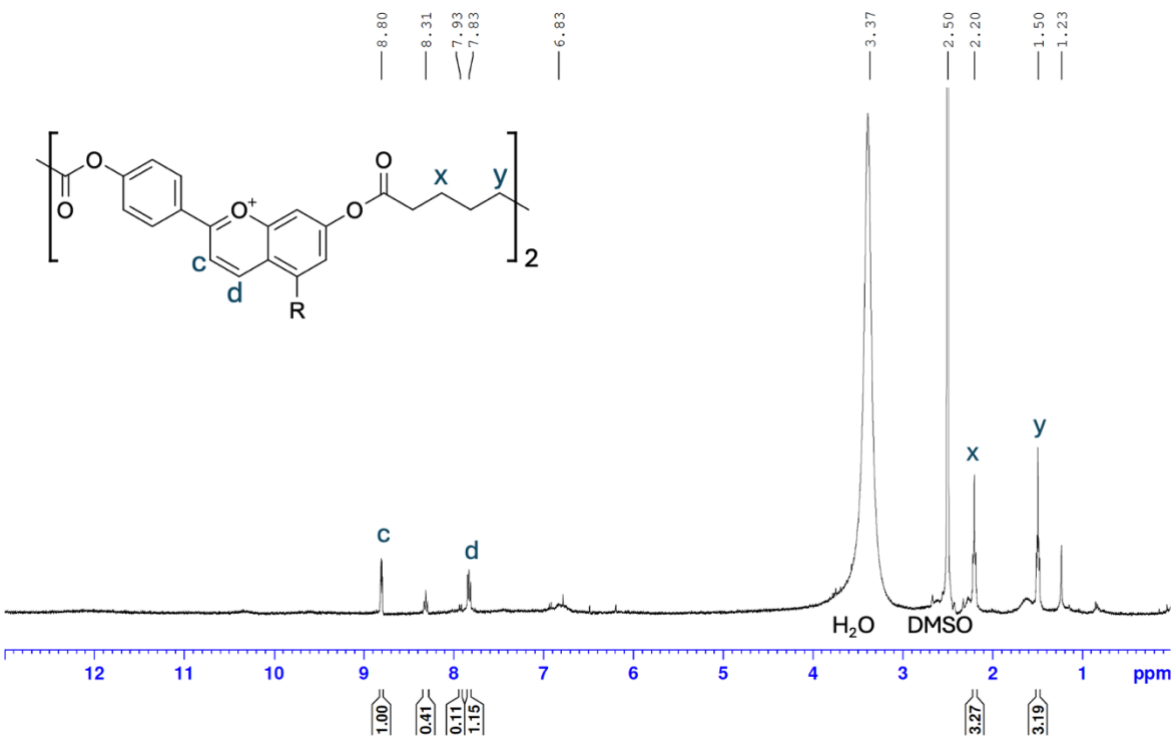

Figure S2.4. [1]HNMR spectra of apigeninidin condensation polymer (AE-CP 61.2) after a soxhlet extraction. 'c' was set as the reference peak.

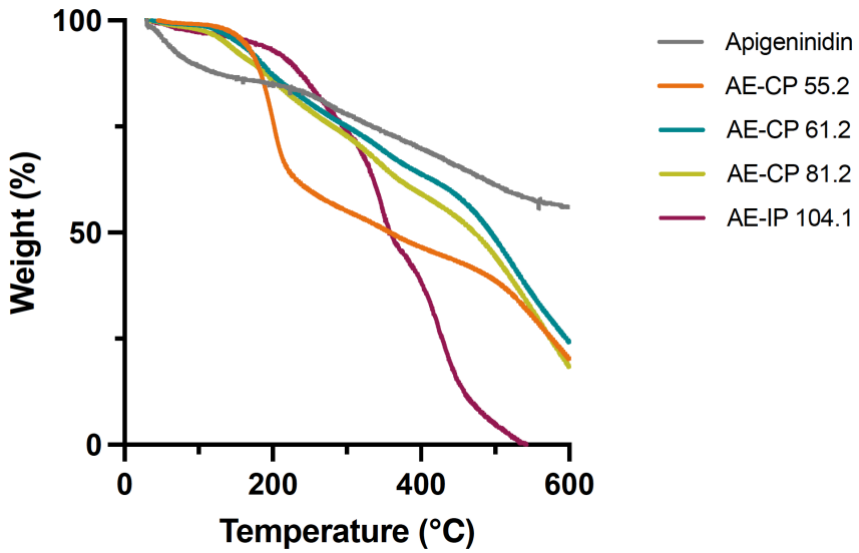

Figure S2.5. Thermogravimetric analysis of apigeninidin and apigeninidin polymers

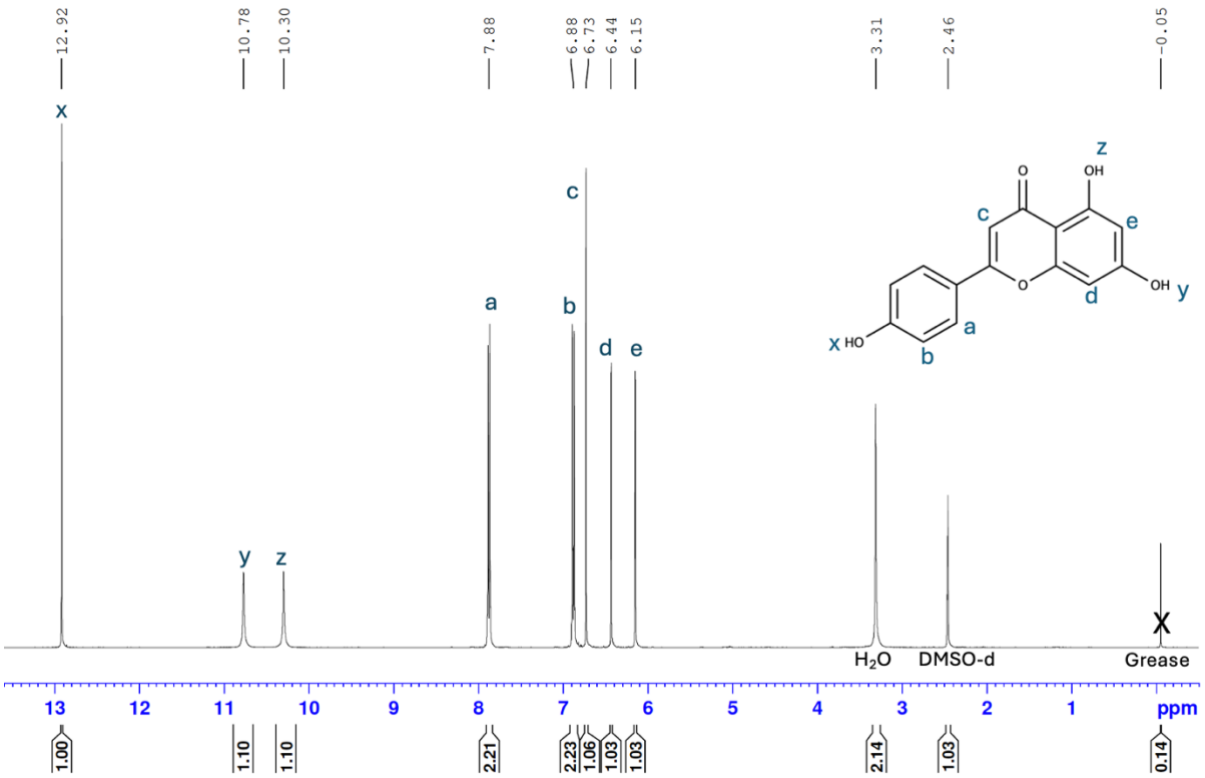

Figure S2.6. [1]HNMR spectra of apigenin

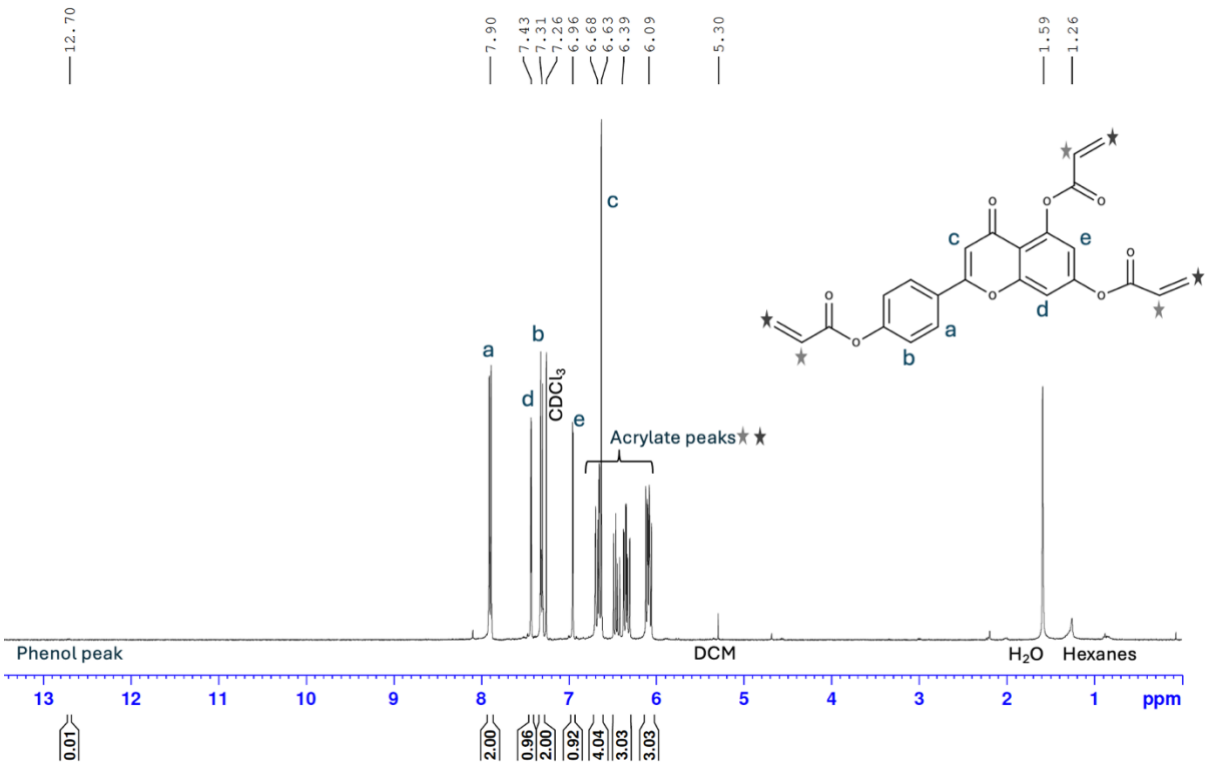

Figure S2.7. [1]HNMR spectra of apigenin acrylate

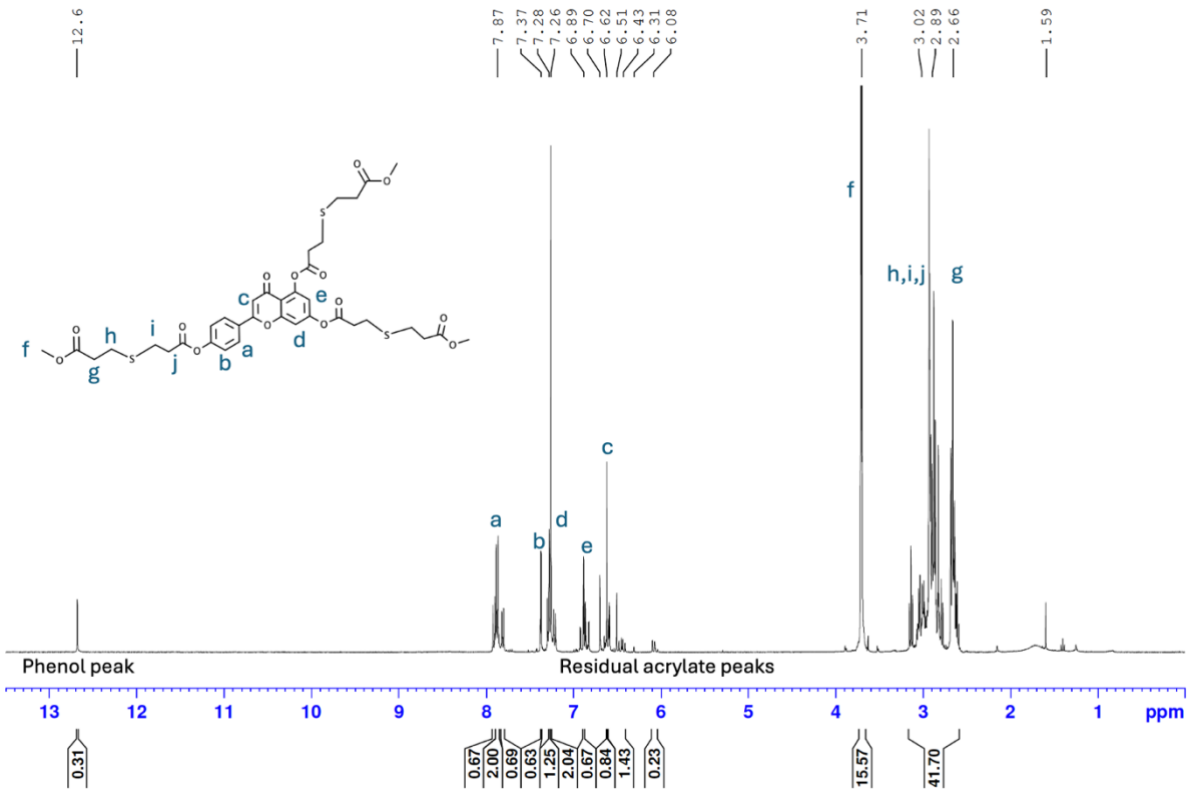

Figure S2.8. [1]HNMR spectra of apigenin-MMP

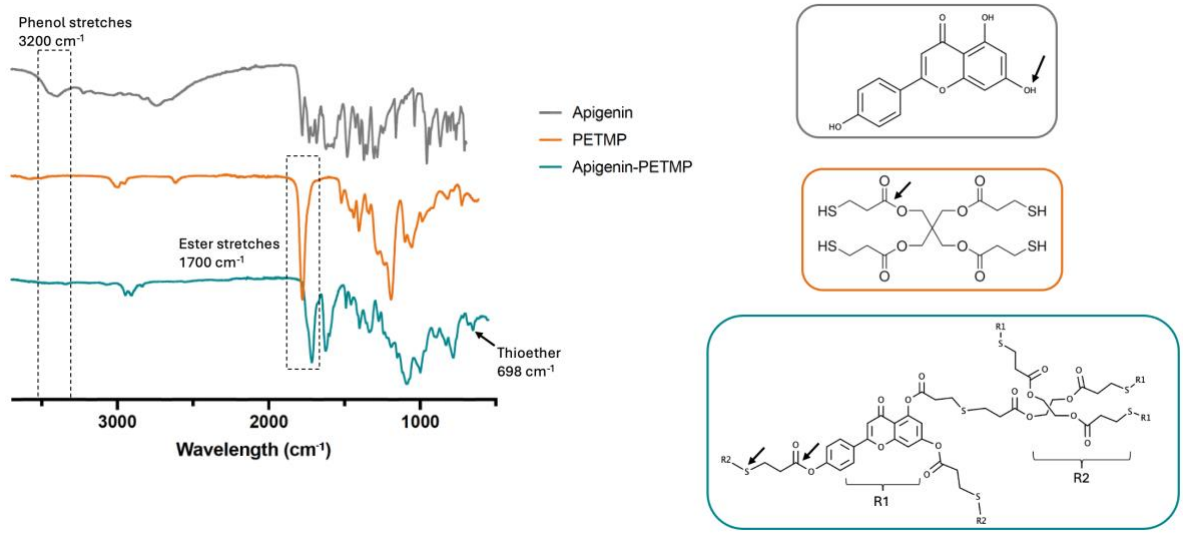

Figure S2.9. FTIR spectra of apigenin-PETMP, showing the starting material (apigenin), reactant (PETMP) and product. The arrows represent the phenol, ester and thioether functional groups where the most changes are expected in the IR spectra of the 3 molecules.

References

(1) Nur, E.; Biemond, B. J.; Otten, H.-M.; Brandjes, D. P.; Schnog, J.-J. B.; CURAMA Study Group. Oxidative Stress in Sickle Cell Disease; Pathophysiology and Potential Implications for Disease Management. *Am. J. Hematol.* **2011**, *86* (6), 484–489. https://doi.org/10.1002/ajh.22012.

(2) Vona, R.; Sposi, N. M.; Mattia, L.; Gambardella, L.; Straface, E.; Pietraforte, D. Sickle Cell Disease: Role of Oxidative Stress and Antioxidant Therapy. *Antioxidants* **2021**, *10* (2), 296. https://doi.org/10.3390/antiox10020296.

(3) Rees, D. C.; Gibson, J. S. Biomarkers in Sickle Cell Disease. *Br. J. Haematol.* **2012**, *156* (4), 433–445. https://doi.org/10.1111/j.1365-2141.2011.08961.x.

(4) Gueye Tall, F.; Martin, C.; Ndour, E. hadji M.; Faes, C.; Déme Ly, I.; Pialoux, V.; Connes, P.; Gueye, P. M.; Ndiaye Diallo, R.; Renoux, C.; Diagne, I.; Diop, P. A.; Cissé, A.; Sall, P. L.; Joly, P. Influence of Oxidative Stress Biomarkers and Genetic Polymorphisms on the Clinical Severity of Hydroxyurea-Free Senegalese Children with Sickle Cell Anemia. *Antioxidants* **2020**, *9* (9), 863. https://doi.org/10.3390/antiox9090863.

(5) Pavitra, E.; Acharya, R. K.; Gupta, V. K.; Verma, H. K.; Kang, H.; Lee, J.-H.; Sahu, T.; Bhaskar, L.; Raju, G. S. R.; Huh, Y. S. Impacts of Oxidative Stress and Anti-Oxidants on the Development, Pathogenesis, and Therapy of Sickle Cell Disease: A Comprehensive Review. *Biomed. Pharmacother.* **2024**, *176*, 116849. https://doi.org/10.1016/j.biopha.2024.116849.

(6) Diaku-Akinwumi, I. N.; Olajide, D.; Adekunle, M. B.; Adebayo, A. B.; Bamiro, S.; Ofakunrin, A. O. D.; Ajonuma, L. C. Jobelyn, a Sorghum Bicolor Exract-Based Oral Supplement Reduces Oxidative Stress in School Aged Children with Sickle Cell Disease. *Blood* **2024**, *144* (Supplement 1), 5362. https://doi.org/10.1182/blood-2024-212305.

(7) McCarty, M. F. Potential Utility of Full-Spectrum Antioxidant Therapy, Citrulline, and Dietary Nitrate in the Management of Sickle Cell Disease. *Med. Hypotheses* **2010**, *74* (6), 1055–1058. https://doi.org/10.1016/j.mehy.2009.12.020.

(8) Cieri-Hutcherson, N. E.; Hutcherson, T. C.; Conway-Habes, E. E.; Burns, B. N.; White, N. A. Systematic Review of L-Glutamine for Prevention of Vaso-Occlusive Pain Crisis in Patients with Sickle Cell Disease. *Pharmacother. J. Hum. Pharmacol. Drug Ther.* **2019**, *39* (11), 1095–1104. https://doi.org/10.1002/phar.2329.

(9) Ibrahim, A.; and Muhammad, S. A. Antioxidant-Rich Nutraceutical as a Therapeutic Strategy for Sickle Cell Disease. *J. Am. Nutr. Assoc.* **2023**, *42* (6), 588–597. https://doi.org/10.1080/27697061.2022.2108930.

(10) Salinas Cisneros, G.; Thein, S. L. Recent Advances in the Treatment of Sickle Cell Disease. *Front. Physiol.* **2020**, *11*. https://doi.org/10.3389/fphys.2020.00435.

(11) Umukoro, S.; Oluwole, O. G.; Eduviere, A. T.; Adrian, O. I.; Ajayi, A. M. Jobelyn® Exhibited Anti-Inflammatory, Antioxidant, and Membrane-Stabilizing Activities in Experimental Models. *J. Basic Clin. Physiol. Pharmacol.* **2015**, *26* (5), 501–508. https://doi.org/10.1515/jbcpp-2014-0113.

(12) Bešlo, D.; Golubić, N.; Rastija, V.; Agić, D.; Karnaš, M.; Šubarić, D.; Lučić, B. Antioxidant Activity, Metabolism, and Bioavailability of Polyphenols in the Diet of Animals. *Antioxidants* **2023**, *12* (6), 1141. https://doi.org/10.3390/antiox12061141.

(13) Rudrapal, M.; Rakshit, G.; Singh, R. P.; Garse, S.; Khan, J.; Chakraborty, S. Dietary Polyphenols: Review on Chemistry/Sources, Bioavailability/Metabolism, Antioxidant Effects, and Their Role in Disease Management. *Antioxidants* **2024**, *13* (4), 429. https://doi.org/10.3390/antiox13040429.

(14) Smoliga, J. M.; Blanchard, O. Enhancing the Delivery of Resveratrol in Humans: If Low Bioavailability Is the Problem, What Is the Solution? *Molecules* **2014**, *19* (11), 17154–17172. https://doi.org/10.3390/molecules191117154.

(15) Pardo, M. R.; Garicano Vilar, E.; San Mauro Martín, I.; Camina Martín, M. A. Bioavailability of Magnesium Food Supplements: A Systematic Review. *Nutrition* **2021**, *89*, 111294. https://doi.org/10.1016/j.nut.2021.111294.

(16) Ehlert, J.; Kronemann, J.; Zumbrägel, N.; Preller, M. Lipase-Catalyzed Chemoselective Ester Hydrolysis of Biomimetically Coupled Aryls for the Synthesis of Unsymmetric Biphenyl Esters. *Molecules* **2019**, *24* (23), 4272. https://doi.org/10.3390/molecules24234272.

(17) Angeli, L.; Imperiale, S.; Ding, Y.; Scampicchio, M.; Morozova, K. A Novel Stoichio-Kinetic Model for the DPPH• Assay: The Importance of the Side Reaction and Application to Complex Mixtures. *Antioxidants* **2021**, *10* (7), 1019. https://doi.org/10.3390/antiox10071019.

(18) Bandeira, P. T.; Dalmolin, M. C.; de Oliveira, M. M.; Nunes, K. C.; Garcia, F. P.; Nakamura, C. V.; de Oliveira, A. R. M.; Piovan, L. Synthesis, Antioxidant Activity and Cytotoxicity of *N*-Functionalized Organotellurides. *Bioorg. Med. Chem.* **2019**, *27* (2), 410–415. https://doi.org/10.1016/j.bmc.2018.12.017.

(19) Lagreca, E.; Onesto, V.; Di Natale, C.; La Manna, S.; Netti, P. A.; Vecchione, R. Recent Advances in the Formulation of PLGA Microparticles for Controlled Drug Delivery. *Prog. Biomater.* **2020**, *9* (4), 153–174. https://doi.org/10.1007/s40204-020-00139-y.

(20) Murphy, N. P.; Lampe, K. J. Fabricating PLGA Microparticles with High Loads of the Small Molecule Antioxidant N-Acetylcysteine That Rescue Oligodendrocyte Progenitor Cells from Oxidative Stress. *Biotechnol. Bioeng.* **2018**, *115* (1), 246–256. https://doi.org/10.1002/bit.26443.

(21) Lefol, L. A.; Bawuah, P.; Zeitler, J. A.; Verin, J.; Danede, F.; Willart, J. F.; Siepmann, F.; Siepmann, J. Drug Release from PLGA Microparticles Can Be Slowed down by a Surrounding Hydrogel. *Int. J. Pharm. X* **2023**, *6*, 100220. https://doi.org/10.1016/j.ijpx.2023.100220.

(22) Jusu, S. M.; Obayemi, J. D.; Salifu, A. A.; Nwazojie, C. C.; Uzonwanne, V.; Odusanya, O. S.; Soboyejo, W. O. Drug-Encapsulated Blend of PLGA-PEG Microspheres: In Vitro and in Vivo Study of the Effects of Localized/Targeted Drug Delivery on the Treatment of Triple-Negative Breast Cancer. *Sci. Rep.* **2020**, *10* (1), 14188. https://doi.org/10.1038/s41598-020-71129-0.

(23) de Toledo, M. C. M. C.; Abreu, A. da S.; Carvalho, J. A.; Ambrósio, J. A. R.; Godoy, D. da S.; dos Santos Pinto, B. C.; Beltrame Junior, M.; Simioni, A. R. Zinc Phthalocyanine Tetrasulfonate-Loaded Polyelectrolytic PLGA Nanoparticles for Photodynamic Therapy Applications. *Photodiagnosis Photodyn. Ther.* **2020**, *32*, 101966. https://doi.org/10.1016/j.pdpdt.2020.101966.

(24) Roberts, R.; Smyth, J. W.; Will, J.; Roberts, P.; Grek, C. L.; Ghatnekar, G. S.; Sheng, Z.; Gourdie, R. G.; Lamouille, S.; Foster, E. J. Development of PLGA Nanoparticles for Sustained Release of a Connexin43 Mimetic Peptide to Target Glioblastoma Cells. *Mater. Sci. Eng. C* **2020**, *108*, 110191. https://doi.org/10.1016/j.msec.2019.110191.

(25) Geera, B.; Ojwang, L. O.; Awika, J. M. New Highly Stable Dimeric 3-Deoxyanthocyanidin Pigments from Sorghum Bicolor Leaf Sheath. *J. Food Sci.* **2012**, *77* (5), C566-572. https://doi.org/10.1111/j.1750-3841.2012.02668.x.

(26) Oyinbo, C. A.; Robert, F. O.; Avwioro, O. G.; Igbigbi, P. S. Jobelyn Suppresses Hippocampal Neuronal Apoptosis and Necrosis in Experimental Alcohol-Induced Brain Stress. *Pathophysiology* **2018**, *25* (4), 317–325. https://doi.org/10.1016/j.pathophys.2018.05.002.

(27) Gulrajani, S.; Snyder, S.; Hackenberg, J. D.; Uhrich, K. Effect of pH on Salicylic Acid-Based Poly(Anhydride-Ester): Implications for Polymer Degradation and Controlled Salicylic Acid Release. *J. Bioact. Compat. Polym.* **2022**, *37* (6), 469–479. https://doi.org/10.1177/08839115221121844.

(28) Prudencio, A.; Schmeltzer, R. C.; Uhrich, K. E. Effect of Linker Structure on Salicylic Acid-Derived Poly(Anhydride−esters). *Macromolecules* **2005**, *38* (16), 6895–6901. https://doi.org/10.1021/ma048051u.

(29) Schmeltzer, R. C.; Anastasiou, T. J.; Uhrich, K. E. Optimized Synthesis of Salicylate-Based Poly(Anhydride-Esters). *Polym. Bull.* **2003**, *49* (6), 441–448. https://doi.org/10.1007/s00289-003-0123-6.

(30) Byrd, H. C. M.; McEwen, C. N. The Limitations of MALDI-TOF Mass Spectrometry in the Analysis of Wide Polydisperse Polymers. *Anal. Chem.* **2000**, *72* (19), 4568–4576. https://doi.org/10.1021/ac0002745.

(31) Sugui, J. A.; Bonham, C.; Lo, S.-C.; Wood, K. V.; Nicholson, R. L. Maldi-Tof Analysis of Mixtures of 3-Deoxyanthocyanidins and Anthocyanins. *Phytochemistry* **1998**, *48* (6), 1063–1066. https://doi.org/10.1016/S0031-9422(98)00087-9.

(32) Wu, Y.; Yu, X.; Ding, W.; Xin, M.; Zhang, X.; Wang, L.; Wang, H.; Wang, J. Macroporous Resins Combined with UPLC-QTRAP-MS/MS for the Purification and Identification of 3-Deoxyanthocyanidins from Sorghum Bicolor L. Moench and Their Bioactivities. *J. Food Sci.* **2024**, *89* (12), 9120–9136. https://doi.org/10.1111/1750-3841.17526.

(33) Nair, D. P.; Podgórski, M.; Chatani, S.; Gong, T.; Xi, W.; Fenoli, C. R.; Bowman, C. N. The Thiol-Michael Addition Click Reaction: A Powerful and Widely Used Tool in Materials Chemistry. *Chem. Mater.* **2014**, *26* (1), 724–744. https://doi.org/10.1021/cm402180t.

(34) Fu, K. L.; Yao, M. Y.; Wang, D. B.; Zhao, H. C.; Cheng, G. W.; Yang, S. Removal of Hg2+ from Flue Gas by Petroleum Thioether. *IOP Conf. Ser. Earth Environ. Sci.* **2019**, *354* (1), 012094. https://doi.org/10.1088/1755-1315/354/1/012094.

(35) Amini, S. M.; Mohammadi, E.; Askarian-Amiri, S.; Azizi, Y.; Shakeri-Zadeh, A.; Neshastehriz, A. Investigating the in Vitro Photothermal Effect of Green Synthesized

Apigenin-Coated Gold Nanoparticle on Colorectal Carcinoma. *IET Nanobiotechnol.* **2021**, *15* (3), 329–337. https://doi.org/10.1049/nbt2.12016.

(36) Choi, S.; Kang, B. S.; Choi, G.; Kang, M.; Park, H.; Kim, N.; Chang, P.; Kwak, M. K.; Jeong, H. E.; Jung, H.-S. Multichamber PLGA Microparticles with Enhanced Monodispersity and Encapsulation Efficiency Fabricated by a Batch-Microfluidic Hybrid Approach. *Adv. NanoBiomed Res.* **2023**, *3* (10), 2300044. https://doi.org/10.1002/anbr.202300044.

(37) Ryu, S.; Park, S.; Lee, H. Y.; Lee, H.; Cho, C.-W.; Baek, J.-S. Biodegradable Nanoparticles-Loaded PLGA Microcapsule for the Enhanced Encapsulation Efficiency and Controlled Release of Hydrophilic Drug. *Int. J. Mol. Sci.* **2021**, *22* (6), 2792. https://doi.org/10.3390/ijms22062792.

(38) Jindal, A. B. Nanocarriers for Spleen Targeting: Anatomo-Physiological Considerations, Formulation Strategies and Therapeutic Potential. *Drug Deliv. Transl. Res.* **2016**, *6* (5), 473–485. https://doi.org/10.1007/s13346-016-0304-0.

(39) Wang, F.; Lou, J.; Gao, X.; Zhang, L.; Sun, F.; Wang, Z.; Ji, T.; Qin, Z. Spleen-Targeted Nanosystems for Immunomodulation. *Nano Today* **2023**, *52*, 101943. https://doi.org/10.1016/j.nantod.2023.101943.

(40) Fang, Y.; Zhang, N.; Li, Q.; Chen, J.; Xiong, S.; Pan, W. Characterizing the Release Mechanism of Donepezil-Loaded PLGA Microspheres *in Vitro* and *in Vivo*. *J. Drug Deliv. Sci. Technol.* **2019**, *51*, 430–437. https://doi.org/10.1016/j.jddst.2019.03.029.

(41) Shibin, V. P.; Nair, B. R. Formulation and Characterization of Quercetin-Loaded Gelatin Microspheres for Drug Delivery and Their Evaluation. *Polym. Bull.* **2024**, *81* (16), 14975–14997. https://doi.org/10.1007/s00289-024-05401-y.

(42) Dinarvand, R.; Moghadam, S. H.; Mohammadyari-Fard, L.; Atyabi, F. Preparation of Biodegradable Microspheres and Matrix Devices Containing Naltrexone. *AAPS PharmSciTech* **2003**, *4* (3), 34. https://doi.org/10.1208/pt040334.

(43) Waeterschoot, J.; Gosselé, W.; Lemež, Š.; Casadevall i Solvas, X. Artificial Cells for in Vivo Biomedical Applications through Red Blood Cell Biomimicry. *Nat. Commun.* **2024**, *15* (1), 2504. https://doi.org/10.1038/s41467-024-46732-8.

(44) Mishra, K.; Ojha, H.; Chaudhury, N. K. Estimation of Antiradical Properties of Antioxidants Using DPPH Assay: A Critical Review and Results. *Food Chem.* **2012**, *130* (4), 1036–1043. https://doi.org/10.1016/j.foodchem.2011.07.127.

(45) Zhao, F.; Liu, Z.-Q.; Wu, D. Antioxidative Effect of Melatonin on DNA and Erythrocytes against Free-Radical-Induced Oxidation. *Chem. Phys. Lipids* **2008**, *151* (2), 77–84. https://doi.org/10.1016/j.chemphyslip.2007.10.002.

(46) Tsia, P.-L.; Hu, M.-K. Free Radical Scavenging and Antioxidative Activity of Melatonin Derivatives. *J. Pharm. Pharmacol.* **2003**, *55* (12), 1655–1660. https://doi.org/10.1211/0022357022250.

(47) Sun, X.-Y.; Wang, J.-M.; Ouyang, J.-M.; Kuang, L. Antioxidant Activities and Repair Effects on Oxidatively Damaged HK-2 Cells of Tea Polysaccharides with Different Molecular Weights. *Oxid. Med. Cell. Longev.* **2018**, *2018* (1), 5297539. https://doi.org/10.1155/2018/5297539.

(48) Wu, C.; Wang, L.; Fang, Z.; Hu, Y.; Chen, S.; Sugawara, T.; Ye, X. The Effect of the Molecular Architecture on the Antioxidant Properties of Chitosan Gallate. *Mar. Drugs* **2016**, *14* (5), 95. https://doi.org/10.3390/md14050095.

(49) Flieger, J.; Flieger, M. The [DPPH●/DPPH-H]-HPLC-DAD Method on Tracking the Antioxidant Activity of Pure Antioxidants and Goutweed (Aegopodium Podagraria L.) Hydroalcoholic Extracts. *Molecules* **2020**, *25* (24), 6005. https://doi.org/10.3390/molecules25246005.

(50) Tian, C.; Liu, X.; Chang, Y.; Wang, R.; Lv, T.; Cui, C.; Liu, M. Investigation of the Anti-Inflammatory and Antioxidant Activities of Luteolin, Kaempferol, Apigenin and

Quercetin. *South Afr. J. Bot.* **2021**, *137*, 257–264. https://doi.org/10.1016/j.sajb.2020.10.022.

(51) Ali, H. M.; Almagribi, W.; Al-Rashidi, M. N. Antiradical and Reductant Activities of Anthocyanidins and Anthocyanins, Structure–Activity Relationship and Synthesis. *Food Chem.* **2016**, *194*, 1275–1282. https://doi.org/10.1016/j.foodchem.2015.09.003.

Chapter 3: Multifunctional Chitosan Hydrogels Targeting Sickle Cell Leg Ulcers

3.1 Introduction

Chronic non-healing wounds are known to affect approximately 1–2% of the world's population. These wounds are classified as chronic based on their inability to heal within an expected time frame[1]. They typically occur due to complications from other diseases such as sickle cell anemia, diabetes, neuropathies and arterial insufficiency. Other factors that influence their formation include burns, trauma and surgical complications[1]. Among chronic wounds, sickle cell leg ulcers (SCLUs) are particularly challenging to treat due to their complexity and unique pathophysiology. Their pathophysiology stems from the underlying driver of sickle cell disease (SCD) – vaso-occlusion; where vascular blockages, low nitric oxide (NO) bioavailability and hemolysis trigger and prolong ulceration. SCLU manifestation evolves from random pain to subcutaneous necrosis, blister formation, and then epidermis destruction which is known to persist for up to 20 years[2,3]. They are also found on the lower extremities of the body – regions already predisposed to poor blood circulation, which exacerbates delayed healing and increases the risk of chronicity[1]. Furthermore, these wounds are often heavily colonized by skin microflora such as *Staphylococcus aureus* and *Pseudomonas aeruginosa*, which become opportunistic pathogens and contribute to their longevity.

The gold standard for SCLU treatment largely involves therapies that primarily target bacterial colonization while failing to address the underlying pathophysiology. These include hydrocolloids, silver- and iodine-based dressings, and standard protective bandages[4]. While infection control is critical, addressing only this component overlooks vaso-occlusion that leads to SCLU persistence. Recent work by Caterina Minniti has aimed to address this through the use of topical sodium nitrite as a vasodilator and nitric oxide (NO) donor, to improve blood flow in SCLUs and target vaso-occlusion[5,6]. However, topical applications face significant limitations, including poor control with dosage, the need for frequent reapplication, and a lack of sustained release. These limitations highlight the need for an integrated therapy – one that

provides sustained antimicrobial and vasodilatory effects while remaining biocompatible with the mechanically active skin of the lower extremities. In this work, we present a hydrogel system engineered to meet this urgent clinical need through a unified, multifunctional design[7].

Hydrogels in Wound Care

Hydrogels are cross-linked 3D polymeric networks that can absorb large amounts of water. In research for enhanced wound care, hydrogels have become promising candidates for wound dressings due to their hydrophilicity, biocompatibility and their mechanical properties. Hydrogels are ideal because of their ability to meet various wound healing requirements such as adequate moisture retention and mechanical strength. Beyond their traditional role as passive wound coverings, they can also be engineered for multifunctionality to include controlled drug delivery, anti-inflammatory activity and stimuli responsiveness[8–10]. Currently, only a few bioengineered approaches have been taken to reduce the burden of SCLUs. These include the use copper-impregnated wound dressings and hydro-responsive dressings. However, these interventions have been tailored to promoting angiogenesis and the regrowth of granular tissue while reducing microbial colonization to improve healing, leaving the need to address vaso-occlusion unmet[4,11,12].

To address this need, we developed a multifunctional chitosan-based hydrogel with intrinsic antimicrobial properties, capable of achieving sustained release of a vasodilator to promote wound healing. Our hydrogel was fabricated from chitosan methacrylate (CHIMA) and poly (ethylene) glycol diacrylate (PEGDA) which offers tunability by adjusting polymer composition to achieve varying mechanical properties. This adaptability is crucial for wound dressings applied around the lower extremities of the legs, where dorsiflexion and mechanical strain demand an elastic modulus that accommodates movement. CHIMA and PEGDA were chosen as our hydrogel precursors due to their low cost, commercial availability, and ease of synthesis, making them promising candidates for scalable and affordable wound care solutions,

especially in resource-limited settings. The hydrogel was embedded with doxycycline, a broad-spectrum antibiotic effective against Gram-positive and Gram-negative bacteria, as well as aerobic and anaerobic pathogens[13]. SCLUs are commonly colonized by *S. aureus*, *P. aeruginosa*, Group A *Streptococci*, and, in some cases, anaerobic bacteria such as *E. coli*. These pathogens fall within the antimicrobial spectrum of both chitosan and doxycycline. In addition, we incorporated amlodipine, a vasodilator known to increase NO bioavailability and enhance blood flow. The goal of this strategy was to address blood vessel occlusion – the driving force of these ulcer persistence. We evaluated the ability of our engineered network to not only release these therapeutics, but also to act as a natural antimicrobial agent due to chitosan's ability to disrupt bacterial cell growth. Furthermore, we assessed its wound closure abilities, adhesive properties and in vitro biocompatibility, using NIH mouse 3T3 fibroblasts to validate its clinical relevance.

3.2 Materials and methods

Chitosan, 85% DA, 1526.5 g/mol (Thermo Scientific) polyethylene glycol, 3350 g/mol (integra chemicals), methacryloyl chloride (Anhydrous, Sigma, 97%), acryloyl chloride (Sigma, $\geq$ 97%), triethylamine (TEA, sigma, $\geq$ 99%), dichloromethane (DCM, Thermo Scientific, $\geq$99.5%), acetic acid (macron fine chemicals, 99%), sodium hydroxide (Fisher, 97%), deuterated solvents; $CDCl_3$, 99.8%, D_2O, 99.8% and TFA-d, 99% (Acros organics), Irgacure 2959 (TCI, >98%), methanol (Fisher, 99.8%), Miller's LB broth, (Fisher Scientific), *Staphylococcus aureus* (SA113 WT) and P. aeruginosa (PA01 WT) Dulbecco's phosphate-buffered saline, dPBS (VWR), PrestoBlue cell viability reagent and live/dead viability kits (Biotium), 4′,6-Diamidino-2-phenylindole dihydrochloride (DAPI, Sigma-Aldrich), phalloidin-iFluor 488 conjugate (AAT Bioquest), paraformaldehyde (Acros organics), triton x-100 (Fisher), Dulbecco's modified eagle medium (DMEM, Gibco), antibiotic-antimycotic (Anti-Anti, Gibco), bovine calf serum (BCS, Sigma-Aldrich), trypsin-EDTA (Gibco), mouse 3T3 fibroblasts cells (obtained from NIH), doxycycline (Fisher, 95%), amlodipine (TCI,

>98%). Solvents used for chemical synthesis were purified under argon; DCM was distilled over calcium hydride and stored under Ar in a dry air-free flask. TEA was distilled over potassium hydroxide pellets and stored under Ar. Acryloyl chloride was distilled in the presence of 2-methyl resorcinol to inhibit polymerization stored under Ar in a dry flask.

3.2.1 Chemical synthesis techniques

Synthesis of chitosan methacrylate (CHIMA)

CHIMA was synthesized by dissolving chitosan (1.0 g, 0.33 mmol) in a 4% v/v acetic acid solution (20 mL) for five hours. Next, the pH was adjusted to pH 7 using a sodium hydroxide solution and inert gas was bubbled through the solution for 15 minutes. To target two to three amine groups for functionalization, methacryloyl chloride (0.2 mL, 2 mmol) was added dropwise to the reaction mixture and allowed to react overnight, in the dark. The resulting solution was dialyzed at room temperature against deionized water for 24 hours and freeze-dried with a lyophilizer to yield white foam-like compound (0.92 g, 85.3%) [14,15].

Synthesis of poly (ethylene glycol) diacrylate (PEGDA)

PEGDA was synthesized following previously established methods[16,17]. Briefly, poly (ethylene) glycol 3350 (10 g, 3.0 mmol) was dissolved in 15 mL dry DCM and mixed with TEA (1.25 mL, 9.00 mmol). Acryloyl chloride (0.5 mL, 7.2 mmol) was added dropwise to the reaction mixture and allowed to react overnight. The resulting mixture was washed in a 2 M solution of K_2CO_3, dried over $MgSO_4$ and concentrated to a slurry using a rotary evaporator. The product was precipitated into a powder with 200 mL of cold ether. The resulting solid was a pure white compound collected via vacuum filtration and stored under inert gas (9.00 g, 86.8%).

Synthesis of CHIMA and PEGDA hydrogels

To synthesize the CHIMA/ PEGDA hydrogels, prepolymer stock solutions were prepared as follows: CHIMA (at concentrations of 5, 10, 15 w/w% in 4% acetic acid solution), PEGDA (31.25 w/w% in either water or dPBS for cell culture), and the photo-initiator, Irgacure (10 w/w% in methanol). The selected CHIMA concentrations were determined based on solubility, with the maximum solubility limit of CHIMA being 15 w/w%. The final CHIMA concentrations in each hydrogel were calculated and categorized into three experimental groups: 0.8, 3.2, and 7.2 w/w% CHIMA hydrogels. For comparative analysis, PEGDA-only hydrogels (20 w/w%) were also synthesized[18]. The prepared stock solutions were mixed in specified ratios to form a 1 mL hydrogel solution (**Table 3.1**). The hydrogel solution was placed between glass slides with a 2 mm spacer, and cured under UV light (365 nm) for 10 to 15 minutes to form gels with a 2 mm thickness. The hydrogels were precisely cut to 2 × 6 mm discs using a biopsy punch. For reference and method reproducability, the final weight concentrations of each component in the hydrogel is detailed in **supplemental table S3.1**

Table 3. 1. A table showing the CHIMA/ PEGDA hydrogel formulation. Therapeutics for release studies were typically added to the water composition of the hydrogel. I2959 stands for Irgacure 2959.

	Weight percent (w/w%)			**Volume in solution (%)**		
	0.8 CHIMA	*3.2 CHIMA*	*7.2 CHIMA*	*0.8 CHIMA*	*3.2 CHIMA*	*7.2 CHIMA*
CHIMA	5	10	15	16	32	48
PEGDA	31.25	31.25	31.25	48	32	16
I2959	10	10	10	10	10	10
H_2O	26	26	26	26	26	26

3.2.2 In vitro mechanical characterization of hydrogels

Elastic modulus and swelling ratio

The mechanical characteristics of the hydrogel were evaluated to determine the CHIMA/PEGDA composition with optimal strength, elasticity and water retention ability. For these experiments, the hydrogels were cut into a 2 × 6 mm cylindrical discs (2 mm height and 6 mm diameter). The elastic moduli of the hydrogels were calculated from the slope of the linear region of the resulting stress-strain curves, defined between 0% and -30% compressive strain. A dynamic mechanical analyzer (Q-800, TA Instruments – New Castle, DE, USA) was employed to achieve these results. A uniaxial compression test was employed. The initial preload force was set to 0.001 N and the initial strain was set to -0.5%. The system ramped the strain at 10%/min to a maximum strain of -100%.

The mass swelling ratios were calculated by determining the wet mass of the hydrogels after equilibrium swelling at 48 h and the dry mass after lyophilization. The *in vitro* swelling behavior was further evaluated over 72 h. The wet and dry mass of the hydrogels were determined at different time points (0, 2, 12, 24, 48, 72 h). The swelling ratio (q) was calculated using the equation below.

$$\text{Mass swelling ratio (q)} = \frac{\text{Ws} - \text{Wd}}{\text{Wd}} \qquad Eq.\ (1)$$

where W_s refers to the mass of the swollen hydrogel and W_d refers to the mass of the dry hydrogel.

Chitosan hydrogel mesh size (ξ)

The mesh size of a hydrogel describes the average distance between each crosslink in its structure[19]. The swelling ratio of chitosan hydrogels change with respect to the mesh size and ionic interactions between the charged molecules on the chitosan structure. Placing these factors into consideration, the mesh size was calculated using the series of equations below[20].

The equilibrium swelling ratio (Q_m) was calculated as follows with the polymer mass considered[21]

$$Q_m = \frac{M_s - M_d}{M_d} \qquad Eq.\ (2)$$

where M_s is the mass of the swollen hydrogel at equilibrium swelling and M_d is the mass of the dried hydrogel after freeze drying. The volumetric swelling ratio, Q_v was then calculated using the swelling ratio based on hydrogel mass.

$$Q_v = 1 + \left(\frac{\rho_{BD}}{\rho_S}\right) * (Q_m - 1) \qquad Eq.(3)$$

where ρ_{BD} is the polymer bulk density and ρ_s is the solvent density. The ρ_{BD} of chitosan and PEGDA are 1 and 1.2 g/cm^3 respectively, and the average bulk density was calculated based on the weight percentage of each polymer in the hydrogel. The polymer volume fraction in equilibrium swollen hydrogel ($v_{2,s}$) was calculated as:

$$v_{2,s} = \frac{1}{Q_v} \qquad Eq.(4)$$

the specific volume of the polymer is.

$$v = \frac{\rho_S}{\rho_{BD}} \qquad Eq.(5)$$

The Peppas-Merrill equation was then used to determine the number average molecular weight between crosslinks, M_c

$$M_c = \frac{1}{\left(\frac{2}{M_n}\right) - \left(\frac{\frac{v}{v1} * \left(\log(1 - v_{2,s}) + X1 * {v_{2,s}}^2\right)}{{v_{2,s}}^{\frac{1}{3}} - \frac{v_{2,s}}{2}}\right)} \qquad Eq.(6)$$

Here, M_n is the number average molecular weight of the un-crosslinked polymer, V1 is the molar volume of the swelling medium, 18 cm^3/mol for water, and X1 is the Flory polymer-solvent interaction parameter, 0.426. The number of links in the chain (N) was calculated with equation 7.

$$N = \frac{2 * M_c}{M_r} \qquad Eq.(7)$$

Where the molecular weight of PEGDA repeating units was 44.05 g/mol and the repeating units (M_r) of CHIMA was determined based on the degree of deacetylation: 161.2 (DD) + 203 (1-DD). The root mean square end to end distance of the polymer chains between two crosslinks ($(r0^2)^{\frac{1}{2}}$) was determined to conclude the mesh size calculations.

$$(r0^2)^{\frac{1}{2}} = l * (C_n * N)^{\frac{1}{2}} \qquad Eq.(8)$$

The carbon-carbon bond length (l) is estimated as 1.54 A and the Flory specific characteristic ratio (C_n) is 19[22]. Finally, to account for the electrostatic repulsion caused by the charged nature of chitosan, the calculated mesh size was multiplied by $f_{\text{electrostatic}}$, a term estimated by comparing the swelling ratio of the polyelectrolyte hydrogel to that of a neutral counterpart (CHIMA and PEGDA in this case)[23,24].

$$f_{electrostatic} = \frac{Q_{polyelectrolyte}}{Q_{neutral}} \qquad Eq.(9)$$

According, the mesh size (ξ) was calculated using the equation below:

$$\xi = {v_{2,s}}^{-\frac{1}{3}} * (r0^2)^{\frac{1}{2}} * {f^{\frac{1}{2}}}_{electrostatic} \qquad Eq.(10)$$

Since hydrogel formulations were based on varying ratios of CHIMA and PEGDA, each parameter was calculated by factoring in the weight percent of both polymers used in each hydrogel formulation.

3.2.3 Antimicrobial susceptibility testing

To assess the intrinsic antimicrobial properties of the chitosan hydrogels, we performed a zone of inhibition (ZOI) assay using two bacterial strains known to colonize SCLUs. The bacterial strains Staphylococcus aureus and Pseudomonas aeruginosa were used in this study. Briefly, overnight cultures of the bacterial strains were diluted to a density of 1×10^8 cfu/mL.

A sterile cotton swab was used to create a bacterial lawn over the surface of sterile Luria-Bertani (LB) agar. Using a sterile biopsy punch, the hydrogels were cut out to have a diameter of 6 mm and placed carefully on the culture plates. The 6 mm diameter was chosen to replicate antibiotic discs used in literature for ZOI studies. The plates were incubated at 37°C for 18 h. After incubation, the diameters of the ZOI were measured. Each experiment was performed in triplicate and PEGDA hydrogels were used as controls.

3.2.4 In vitro cell compatibility studies

Supernatant cell assay

NIH 3T3 mouse fibroblasts were used for all cell compatibility studies. The cells were cultured in DMEM media supplemented with 10% bovine calf serum and 1% antibiotic-antimycotic. Cells were incubated at 37°C in a 5% CO_2 atmosphere. The hydrogels were synthesized following methods described previously with aseptic modifications by using sterile filtered solutions and dPBS instead of water. The sample 2 × 6 mm discs were cut out and incubated in 1 mL media till equilibrium swelling at 48 h. The cells were grown in a 75 cm^2 culture flask, trypsinized and passaged into 48-well plates at a density of 1×10^4 cells/cm^2.

After 24 h of cell growth, the media in the well plates were gently aspirated and replaced with 1 mL media from the equilibrated hydrogel, containing hydrogel supernatant. Control wells were replaced with fresh media. Cell viability was determined via a live/ dead stain assay™. After 24 h, the supernatant was aspirated, and the cells were fixed and stained in the dark using a solution of Ethidium Homodimer III (4μM) and Calcein AM (2μM) dispersed in sterile PBS. All samples were imaged with a fluorescence microscopy (Alexa Fluor λ^{Em} = 517 and mCherry λ^{Em} = 610, Axiovert Observer Z1, Zeiss). Analysis was done with the ImageJ software.

As an additional experiment to determine quantitative cell viability, a PrestoBlue metabolic assay was performed following the previously described cell culture protocol. Cells were seeded at a density of 3×10^3 cells/cm^2. After a 24h incubation of cells with media containing the hydrogel supernatant, the supernatant was replaced with 200µL of PrestoBlue solution followed by a 30-minute incubation in the dark. The absorbance read out was determined using a SpectraMax iD3 microplate reader [Ex: 530, Em: 585; gain 80]. The control for this experiment was cells incubated with media containing no hydrogel supernatant. The absorbance readout from these wells was used as a reference for 100% viability when plotting cell viability graphs (**Fig S3.5**)

2D cell seeding

A 2D cell seeding assay was performed to study the adhesive nature of the hydrogel groups. First, the cells were seeded on the hydrogels at a density of 1×10^4 cells per scaffold and placed in 48-well plates containing 1 mL medium. The cells were left to proliferate for 24 h and imaged afterwards. The viability of cells were also visualized via a live/dead stain assay. Using the same live/dead stain protocol stated above, the seeded hydrogels were stained and imaged. The results from these experiments were used to narrow down the optimal hydrogel formulation for further experimental analysis.

3.2.5 Hydrogel adhesion testing: in vitro analysis on cells and tissues

Based on the mechanical characterizations and initial cell studies, we were able to identify the hydrogel experimental group that desired properties such as modulus that can accommodate use within lower extremities and high cell viability (3.2% CHIMA). To confirm that the hydrogels from this group will not adhere to cells and disrupt healing, we performed a hydrogel-cell adhesion study using NIH 3T3 mouse fibroblasts. In this experiment, cells were

plated on 24-well plates to achieve a density of 5×10^4 cells/cm^2. After 24h cell growth, old media was removed, and the hydrogels were then placed directly on the layer of cells then supplemented with fresh media. At 24 and 48-hour time points, the media was aspirated, and the gels were gently detached from the well plates containing cells. The cells were fixed with 4% paraformaldehyde and permeabilized with 0.1% triton x-100 then stained with Fluorescein-isothiocyanate-conjugated phalloidin and DAPI to visualize the cytoskeleton and nuclei of the cells. For these experiments, cells with no gels and 15% (w/w), GelMA were used as negative and positive controls respectively, and all experimental groups were tested in triplicate.

Next, to confirm that the hydrogel will not stick to tissue and impede the wound healing process, we observed the interactions between the hydrogel and tissue over time by performing a surface contact test. Here, two rectangular porcine lung tissues were cut using a scalpel blade (1 cm x 2 cm) and fixed onto glass slides with super glue. A hydrogel slab with a 2 mm height was cut out using a scalpel blade to achieve a dimension of 1 cm × 1 cm). The hydrogel was then placed in between the tissue and adhesion was observed for 20 minutes[25].

Finally, the adhesive characteristics of the hydrogel were studied by using a wound closure test (ASTM F2458-05) and a modified lap shear test (ASTM F2255-05) to determine the adhesion strength and shear strength respectively. In the wound closure test, two rectangular porcine lung tissues were cut using a scalpel blade (1 cm × 2 cm) and fixed onto glass slides with super glue. The tissues were brought together and the groove in between each tissue was covered with 3.2% CHIMA solution, covering a total surface area of 1 cm^2. Next, the hydrogel solution was crosslinked under UV_{365nm} light for a total of 10 minutes. The amount of prepolymer solution used was 200 µL, added in 100 µL increments, because of low solution viscosity. A mechanical tester (Instron 5943) with a 100 N load cell was employed to determine the failure point of the hydrogel while being pulled at a strain rate of 1 mm/min[26]. A lap shear test modified by replacing the standard gelatin coat on a glass slide with tissue was also performed. Here, two rectangular porcine lung tissues (1 cm × 2 cm) were fixed onto glass

slides with super glue. Next, 200 μL of the 3.2% CHIMA solution was pipetted and photo-crosslinked between the two tissue samples. To address difficulties in crosslinking the prepolymer solution with UV light, we first partially cured a small volume of the hydrogel directly onto each tissue surface. The tissues were then brought together, and an additional layer of the prepolymer solution was applied at the interface and fully crosslinked under UV light[25].

3.2.6 Kinetic release of therapeutics from the hydrogel

The release kinetics of the active components embedded in the hydrogel, doxycycline (DOX) and amlodipine (AML) were determined by performing an *in vitro* release study. Briefly, the hydrogels were fabricated using methods described earlier (**Section 3.2.2**), the drug-loaded hydrogels were synthesized by replacing the water composition with stock solutions of either doxycycline or amlodipine, at pre-determined concentrations (**Table 3.2**). The gels were cut out into 2 × 6 mm hydrogel disks and placed in 0.5 mL deionized water. At 0.5 h, 2 h, 8 h, 12 h, 25 h, 37 h, 45 h, 72 h, and 100 h time point intervals, aliquots were taken and freeze dried for analysis using an LCT Premier TOF LC/MS (Waters, Milford, MA, USA). Each time point included one blank hydrogel sample as a control and three drug-loaded samples. The freeze-dried aliquots were dispersed in 0.1 mL filtered HPLC grade water and analyzed using an optimized LC-MS acquisition method. Here, the concentration of unknown samples were determined using a standard curve.

Table 3. 2 Showing the Drug stock concentrations for each therapeutic and the final amount in each hydrogel disc

	Drug stock concentration (µg/mL)	Volume in entire hydrogel (µl)	Amounts in 2x6mm hydrogel
Doxycycline	2000	260	29.38µg
Amlodipine	2900	260	42.60µg

3.2.7 Calibration and accuracy

The calibration curve for doxycycline and amlodipine were validated with a series of standard samples in the range of 0 – 35 µg/mL and 27 – 50 µg/mL for DOX and AML respectively. AML samples had an LC-MS limit of detection at a concentration of 27 µg/mL. The linearity of the standard curve was created by plotting the area under the peak intensity curves over the analyte concentration and fitted by a simple linear regression. The calibration curve was obtained by analyzing triplicates of each standard sample. (**Fig S3.7)**

3.2.8 Instrumentation and chromatographic/ spectrometry conditions

The chromatographic system used for DOX and AML detection were different based on varying wavelengths, solvent and column affinities. For DOX, samples were infused using direct loop injection on a Waters Acquity UPLC system, using an Acquity BEH C18 1.7µm column (50 × 2.1 mm). The mobile phase consisted of an isocratic mixture of acetonitrile and water (5:95, *v/v*) with 0.2% formic acid. The UV detection wavelength was set at 278nm, with a flow rate of 0.1mL/min and an injection volume of 5µl. For AML, samples were infused using direct loop injection on a Waters Acquity UPLC system, using an Agilent Zorbax Eclipse XDB fluoro-phenyl column (2.1 × 50 mm) . The mobile phase consisted of a gradient mixture of acetonitrile and water (2:98, *v/v* to 98:2) with 0.2% formic acid. The UV detection wavelength was set at 370nm, with a flow rate of 0.3mL/min and an injection volume of 5µl. The total run

time for each samples was 10 minutes. ESI-TOF measurements were carried out on a Waters LCT-Premier XE Time of Flight Instrument controlled by MassLynx 4.1 software (Waters Corporation, Milford MA). The instrument was equipped with the Multi Mode Ionization source operated in the electrospray mode. A solution of Leucine Enkephalin (Sigma Chemical, L9133) was used in the Lock-Spray.

3.2.9 Statistical analysis

All data are presented as mean ± standard deviation unless otherwise stated. Statistical comparisons between groups were conducted using unpaired, two-tailed Student's t-tests. An alpha level of 0.05 was used to determine significance. Graph generation and statistical analyses were performed using Microsoft Excel and GraphPad Prism.

3.3 Results and discussion

3.3.1 Synthesis of chitosan methacrylate (CHIMA) and polyethylene glycol diacrylate (PEGDA)

CHIMA was synthesized based on established protocols, with a minor modification[15]. Methacrylic anhydride is commonly used for this reaction, however we switched this to methacryloyl chloride due to its higher electrophilicity, improved selectivity for amine functionalization. This modification led to better functionalization[15,27]. One of the incentives for using chitosan in this work was to leverage its intrinsic antimicrobial properties while developing a hydrogel with optimal mechanical performance. To develop a mechanically robust hydrogel, we regulated the crosslinking density by using low molecular weight chitosan and limiting functionalization to two to three methacrylate groups per polymer chain. This was achieved by calculating the amount of methacryloyl chloride required to functionalize the chitosan NH_2 groups. Our functionalization was kept at a range of 10 – 30% methacrylation

(**Scheme 1**). *^{1}H NMR (400 MHz, D_2O) δ = 5.96 and 5.56 (vinyl protons, 2H, CH_2), 5.56 (s, H, CH_2), 3.01 – 3.65 (m, 63H), 1.90 (s, 3H, CH_3), 1.74 (s, 3H, CH_3)* (**Fig S3.1**). PEGDA synthesis was also achieved using established protocols[16,17]. The acrylation degree was 70 % or higher for all batches synthesized. *^{1}H NMR (400 MHz, $CDCl_3$) δ = 6.41 (d, 2H, CH_2), 6.14 (m, 2H, CH_2), 5.82 (d, 2H, CH_2), 4.30 (t, 4H), 3.64 – 3.73 (m, 320H)* (**Fig S3.2**).

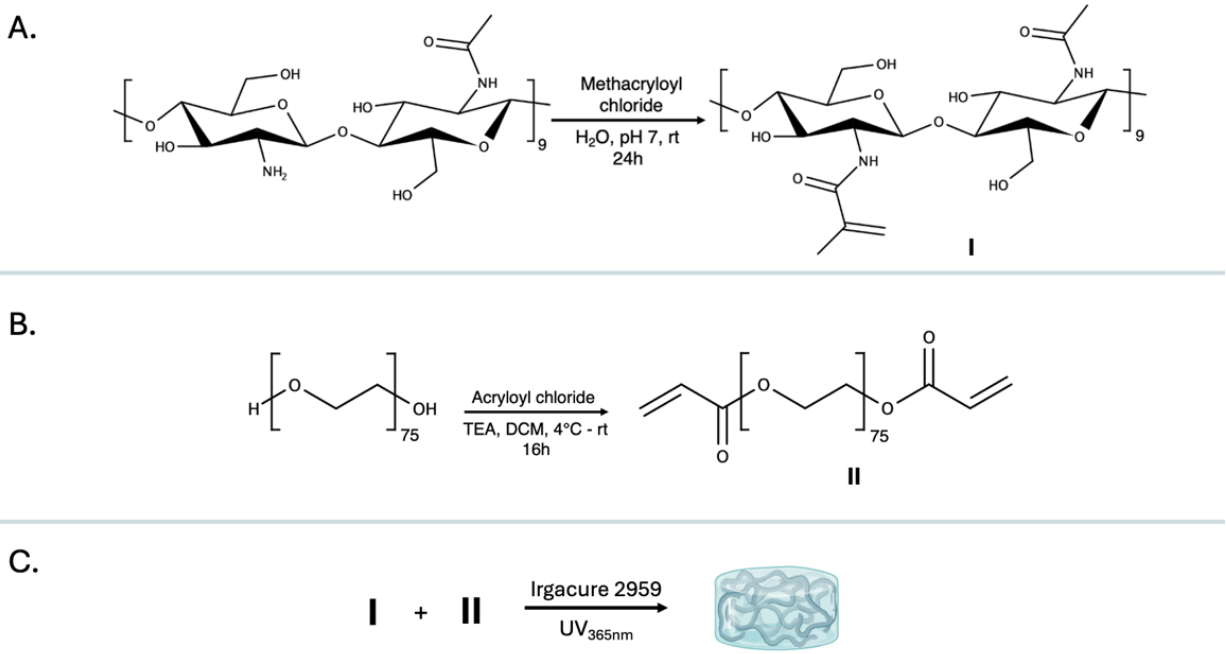

Scheme 3.1. A) Synthesis of chitosan methacrylate and B) Synthesis of polyethylene glycol diacrylate. C) Graphical representation of hydrogel synthesis, I and II in varying and pre-determined concentrations.

3.3.2 Mechanical characterization of the hydrogels

To determine the optimal hydrogel composition for our specific application, the modulus, swelling ratio and mesh size of our hydrogels were calculated. The elastic modulus of the hydrogels decreased with increasing CHIMA concentrations. Control (20% PEGDA), 0.8%, 3.2% and 7.2% CHIMA exhibited moduli of 285 ± 2.86 kPa, 175 ± 0.97 kPa, 51 ± 8.38 kPa and 15 ± 0.70 kPa respectively (**Fig. 3.1A**). Next, we evaluated both the equilibrium and

time-dependent swelling behavior of the hydrogels. Since the material is intended as a wound dressing precursor, high and sustained water retention is desirable. As expected, swelling ratios increased with higher CHIMA content, indicating enhanced water absorption over time. The equilibrium swelling for each hydrogel was reached after 48 h. Control (20% PEGDA), 0.8%, 3.2% and 7.2% CHIMA showed ratios of 6.7 ± 0.06, 8.9 ± 0.24, 24.8 ± 2.5, 94.3 ± 11 (**Fig. 3.1A**).

Overall, the mechanical properties of the different gel compositions show that higher CHIMA concentrations produce gels with enhanced water retention and reduced mechanics. Regarding the mechanical strength, gels with moduli between 40 – 55 kPa are optimal because this is the recorded modulus of the skin and tissues around the ankles. This makes 3.2% CHIMA a good candidate for future experiments[28,29]. These results also highlight the advantage of tuning the mechanical properties of the hydrogel by adjusting its composition. We also recorded a 388% relative swelling capacity (RSC) in the 3.2% CHIMA gel composition, showing its ability to absorb a good amount wound exudate early on without compromising its structural integrity. When compared to the 0.8% and 7.2% gels, we recorded a 104% and 1844% RSC respectively, which are either too low, not absorbing enough initial moisture or too high, compromising the gel's strength.

$$RSC\ (\%) = \frac{Swelling\ ratio\ at\ equilibrium\ swelling\ - Swelling\ ratio\ at\ 0\ h}{Swelling\ ratio\ at\ 0h} \quad Eq.(11)$$

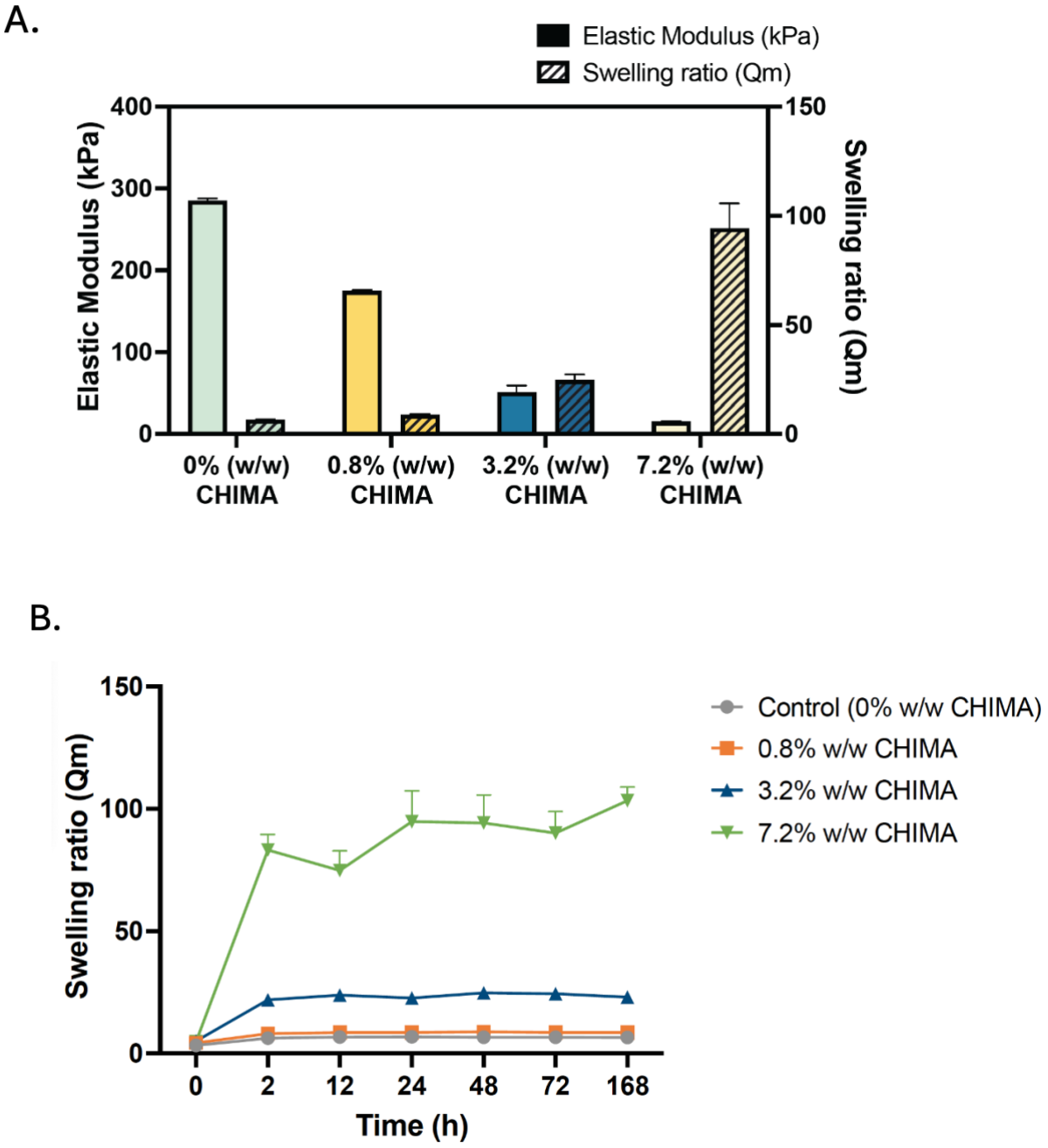

Figure 3. 1. A) Elastic modulus and swelling ratio trends of CHIMA hydrogels. B) Time-dependent swelling ratio of CHIMA hydrogels.

Finally, **Table 3.3** also shows the mesh size values of the synthesized hydrogels. Mesh size was initially estimated using conventional methods widely applied in chitosan-based hydrogels, namely the Flory-Rehner theory and Peppas-Merrill equations[21]. These models relate the equilibrium swelling behavior of polymer networks to their molecular architecture,

allowing an indirect calculation of network mesh size. However, these equations were originally developed for neutral polymers and do not account for the polyelectrolye nature of chitosan. Chitosan contains protonated amine groups in acidic or aqueous environments that introduce electrostatic repulsion between polymer chains. This results in enhanced swelling and altered chain conformations compared to neutral hydrogels. Therefore, applying neutral network theory to such systems introduces limitations and can lead to inaccurate mesh size estimations. To address this, we incorporated an electrostatic correction method described in literature, which relates mesh size to the swelling ratio of polyelectrolyte hydrogels compared to a neutral hydrogel (for this study, CHIMA and PEGDA were used)[23,30,31]. This adjustment introduces a factor, $f_{electrostatic}$ derived from the ratio of swelling in charged vs. uncharged gels, and is used to modify the mesh size estimate accordingly. This approach allowed us to better account for the contributions of charge-mediated swelling while still applying classical theory.

Nonetheless, determining the actual mesh size in polyelectrolyte hydrogels remains challenging. Theoretical estimates may not reflect the true nanoscale architecture of the network. Studies have shown that experimental techniques such as scanning electron microscopy (SEM), and dynamic light scattering (DLS) offer more reliable and direct measurements of hydrogel mesh structure[32,33]. For example, Lopez *et al*. demonstrated a significantly lower crosslinking density in theoretical predictions, when compared to experimental models. Here, we aimed to address these limitations by using swelling-based electrostatic corrections. Overall trends observed was an increase in hydrogel mesh size as the chitosan composition increases. This matches with the stated hypothesis that charge-to-charge repulsion seen in polyelectrolyte networks can increase mesh size and water uptake[34].

Table 3. 3. A table showing the estimated mesh size of the hydrogel groups in correlation to their respective water retention ability.

Experimental group	Mesh size (Å)	Relative swelling capacity (%)
Control (0% CHIMA; w/w)	53.0 ± 0.16	101.0
0.8% CHIMA (w/w)	66.0 ± 1.5	104.0
3.2% CHIMA (w/w)	165 ± 13	388.0
7.2% CHIMA (w/w)	394 ± 41	1844

3.3.3 Antimicrobial properties of CHIMA hydrogels

Chitosan is known as a nontoxic, natural antimicrobial polymer which is GRAS certified (Generally Recognized as Safe by the FDA). Therefore, we evaluated the ability of our hydrogels to display these intrinsic antimicrobial behaviors in the absence of any added antimicrobials[35]. The PEGDA control and 0.8% CHIMA groups displayed no antimicrobial behavior ZOIs with recorded at 0 mm. However, as the concentration of chitosan increased, an increase in the antimicrobial activity was observed in both *S. aureus* and *P. aeruginosa* cultures. In *S. aureus* cultures, ZOIs of 8.3 ± 0.6 mm and 9.7 ± 0.6 mm were seen for 3.2 and 7.2 CHIMA hydrogels respectively. Higher microbicidal activities were seen in *P. aeruginosa* cultures with ZOIs of 9.7 ± 0.6 mm and 12 ± 1 mm for 3.2 and 7.2 CHIMA hydrogels respectively (**Fig. 3.2B**). These values are comparable to the ZOIs of commercially available antibiotics used against *S. aureus* and *P. aeruginosa*. For instance, ceftriaxone (30 μg) exhibits a ZOI of 19 mm against *P. aeruginosa*, while erythromycin (5 μg) produces a ZOI of 10 mm against *S. aureus.* Notably, bacitracin (0.04 μg), a commonly used antibiotic for SCLU, shows no inhibition (0 mm ZOI) against *S. aureus*[36,37]. These results highlight the functionality of our construct and directly addresses the microbial colonization issues seen in SCLUs which increases the longevity of SCLUs.

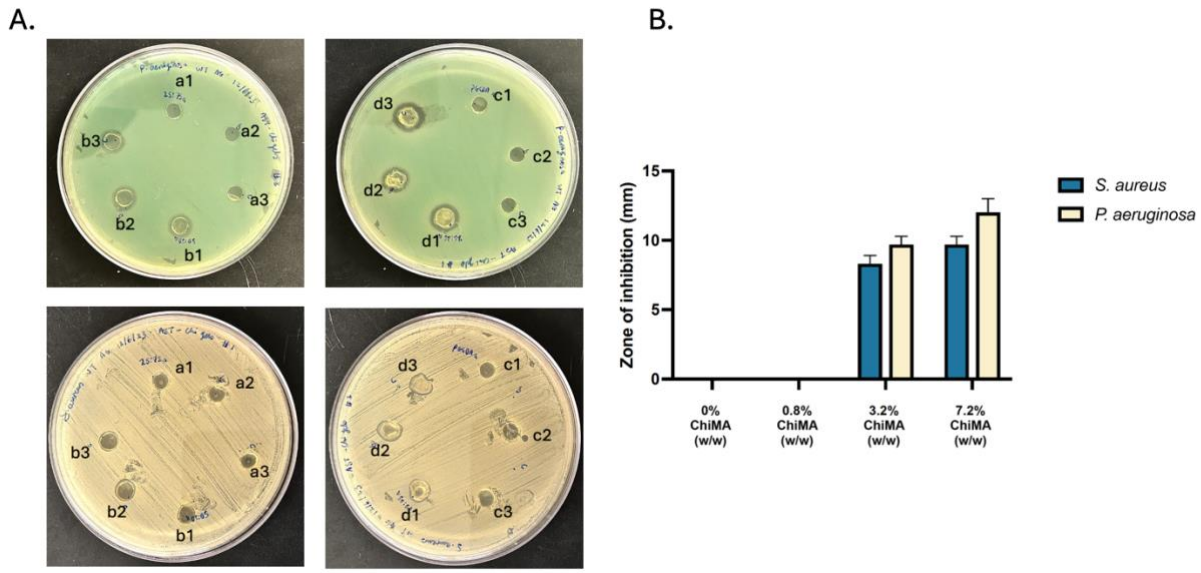

Figure 3. 2. A) Images of bacterial culture plates after ZOI experiments. B) Quantification of the ZOI studies. *Hydrogels made in triplicates where; a = 0.8% CHIMA gel, b = 3.2% CHIMA gel, c = 0% CHIMA/ control, d = 7.2% CHIMA gel. 0% CHIMA gels were set as the control*

3.3.4 *In vitro* cell viability

Supernatant cell assay

To assess the biocompatibility of the hydrogels, we performed a supernatant cell assay to evaluate how components released from the hydrogel may affect mammalian cell viability. In these experiments, we quantified the cytocompatibility of all the CHIMA experimental groups, 7.2% CHIMA, 3.2% CHIMA, 0.8% CHIMA and 0% CHIMA group (20% PEGDA). We observed an increase in cell viability as CHIMA concentration decreased with the 7.2% group having the lowest viability. However, when compared to the positive control which was cells grown with 100% fresh media and no hydrogel supernatant, we saw no significant differences in the 0.8 and 3.2 group. The cell viability of the 0.8 and 3.2 groups were 96% and 70% respectively (**Fig 3.3A, B**)

2D cell seeding

To further evaluate hydrogel-cell interactions, we performed an experiment to study adherence of cells to the hydrogel surface. This was done as the first proof-of-concept experiment to confirm that the hydrogel wound dressing will not adhere to cells and disrupt the wound healing process. Minimizing cell adhesion is critical for wound dressings, particularly in chronic wounds or ulcers, as excessive cell attachment to the dressing can mechanically disrupt re-epithelialization, damage newly formed granulation tissue during dressing changes, and worsen local inflammation. Recent studies have shown that non-adherent dressings are beneficial because they reduce trauma upon removal, support tissue regeneration, and help maintain a favorable environment for healing[38,39]. Here, we observed that as the concentration of CHIMA increased, there was a decrease in the number of cells on the surface of the hydrogels. For 20% PEGDA (control) and 7.2% CHIMA samples, there was an average of 2 and 3 cells/ gel surface respectively, showing low survival when cells are in direct contact with the gel. 0.8% CHIMA had the highest cell survival and adhesion with an average of 51 cells/gel surface. However, this increases the risk of cell adherence, making 3.2% CHIMA the best candidate with approximately 9.5 cells/ gel surface, showing good cell viability without high adherence as seen in the cell morphology (**Fig 3.3C, D**)

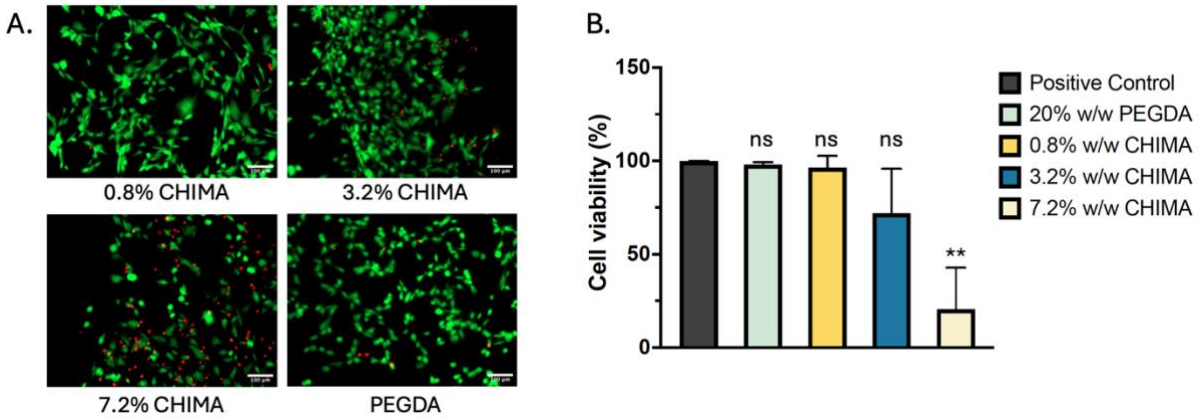

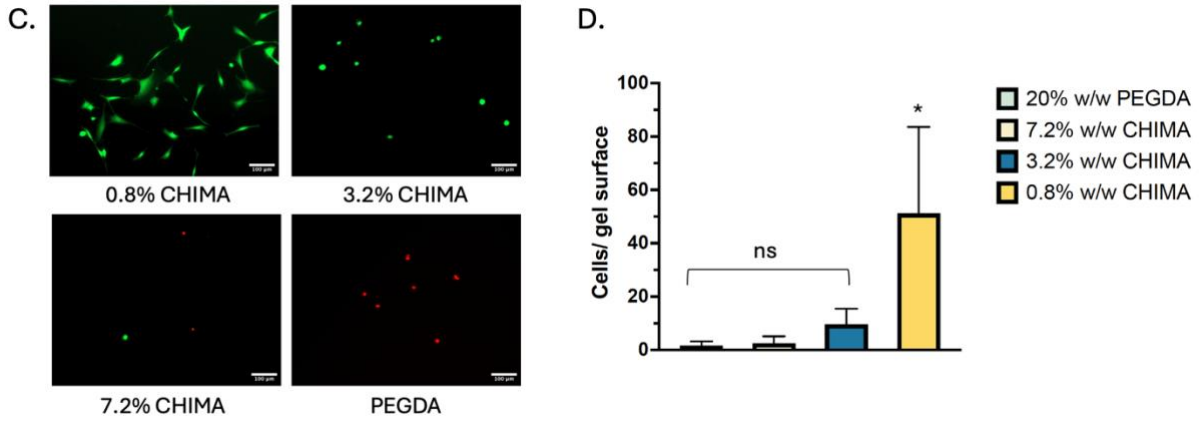

Figure 3. 3. Hydrogel-cell compatibility assays. A) Representative live/ dead images showing how cells respond in the presence of hydrogel supernatant after 24h. B) Quantification of cell proliferation in hydrogel supernatant after 24h. *Statistically significant differences in cell viability were seen between the 7.2 CHIMA group and the positive control, no statistical differences were found between the other groups and the control. Error bars indicate the standard error from the mean, asterisks mark significant levels (**P <0.05), and ns refers to no significance.* C) Representative live/ dead images showing the growth of cells on the surface of the hydrogels after 24h. D) Quantification of cell proliferation on hydrogel surface after 24h. For all experiments, control groups were cells treated with no hydrogel and cells treated with PEGDA hydrogels

3.3.5 Hydrogel adhesive properties

Cell adhesion

Building on the results of cell viability and mechanical characterization experiments, we further assessed the adhesive properties of the optimal hydrogel formulation, 3.2% CHIMA. These experiments worked to confirm the hydrogels' ability to act as a great wound dressing while avoiding the possibility of unwanted cell and tissue adhesion during the stages of wound healing[39]. We observed no cell adhesion in both hydrated and non-hydrated (freeze-dried) CHIMA gels (in contrast to GelMA hydrogels, which served as a negative control due to their

known tendency to adhere to cells). The non-hydrated gels were rehydrated for 24 h and observed at 24 hours (**Fig. 3.4A**) and 48 hours (**Fig. 3.4B**) after re-hydration. We observed a limited number of instances where the cells did not adhere to GelMA gels in the non-hydrated, 48 h timepoint. We hypothesize that this may be due to the amount of time that the cells spent in culture (96 h). At 96 h, the cells are close to confluency leading to increased cell-cell interactions, secretion of more ECM proteins like collagen and presence of stronger focal adhesion (**Fig S3.4)**

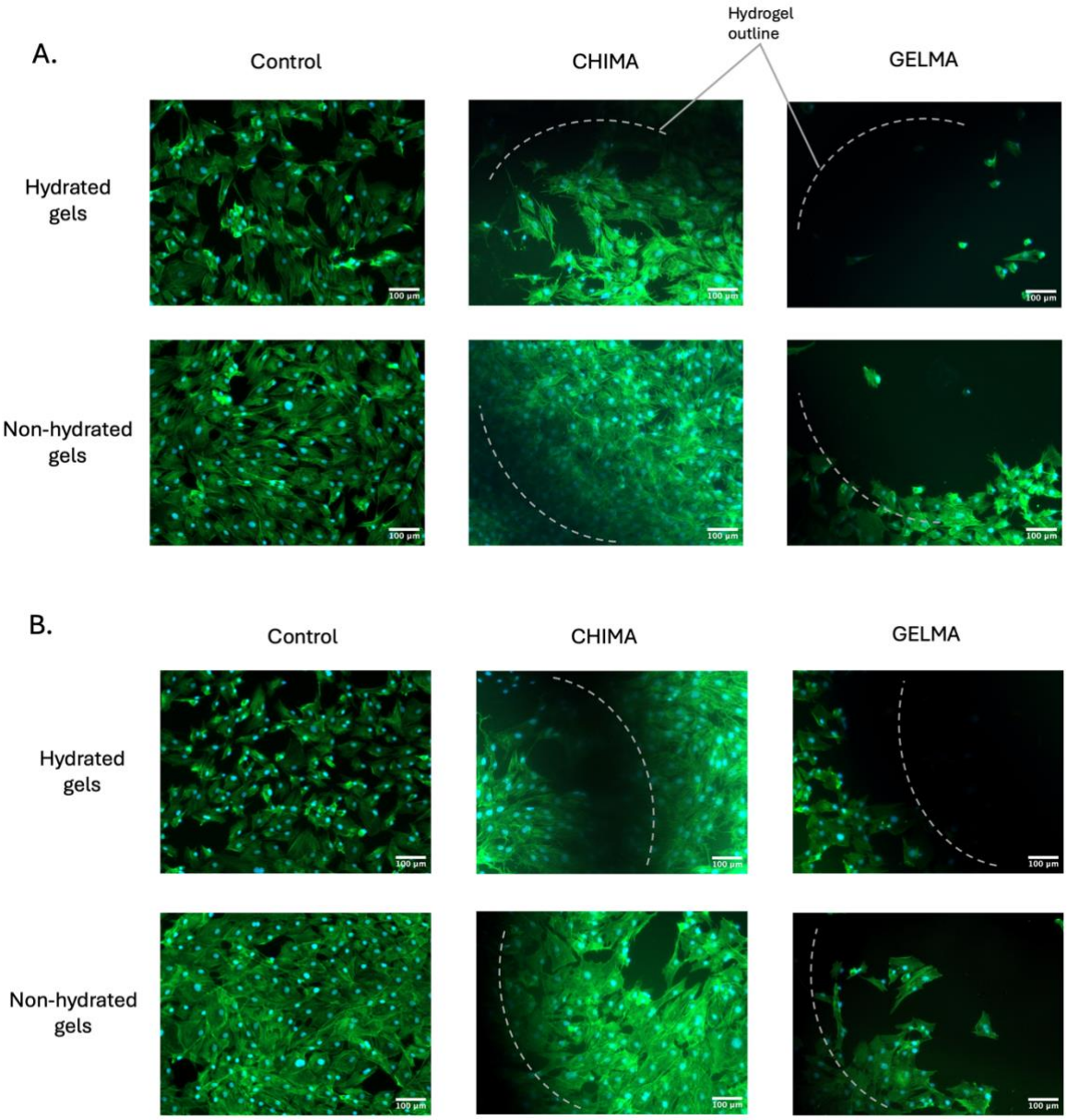

Figure 3. 4. Hydrogel cell-adhesion assay. A) Phalloidin/ DAPI stained cells showing hydrogel adhesion to cells after a 24h incubation. B) showing adhesion after a 48h incubation. Control

groups were cells treated with no hydrogel (negative control) and cells treated with GelMA hydrogels (positive control). *The outline shows where the hydrogels were placed, this was confirmed with markings made at the bottom of the well plates through phase and brightfield images (**Fig. S3.3)***

Tissue adhesion

The adhesive characteristics of the 3.2% CHIMA gels were studied on the basis standard adhesion tests provided by American Society for Testing and Materials (ASTM). Particularly, a wound closure test (ASTM F2458-05) and modified lap shear test (ASTM F2255-05) were used to determine the adhesion strength and shear strength respectively. The tissue adhesive strength was determined at the point of failure as hydrogel-sealed tissues were pulled apart with a mechanical tester (Instron 5943) at a strain rate of 1 mm/min. The set up for both the wound closure and modified lap shear tests are shown in **Fig 3.5**. The results of this experiment showed an average adhesion strength of 5.84 ± 2.04 kPa and a shear strength of 9.32 ± 0.6 kPa. These numbers are significantly low when compared to FDA-approved tissue sealants such as Co-SEAL which has an adhesion and shear strength of 69 and 19 kPa respectively[25,40]. For context, these sealants are designed for surgical settings to achieve homeostasis, so a high adhesion strength is desirable. For our hydrogels however, adhesion to an open or healing ulcer may cause more damage by disrupting the formation of new tissue and overall the wound healing process[41]. This trend is important to study in hydrogel wound dressings since it can affect the wound healing process. Particularly, acrylated and methacrylated hydrogels such as PEGDA and GelMA have been reported to form covalent and non-covalent bonds with tissue, through intermolecular hydrogen bonding interactions between oxygen atoms on the hydrogel and amine, carboxyl and hydroxyl groups on tissues[26,38]. However, we hypothesize that the lack of this property is due to the high relative swelling capacity of the hydrogel and its high water content, creating a diffusion barrier and reducing direct interaction between the cells or tissue and the gel. Additionally, we performed a surface

contact test where the cured hydrogel and tissue were observed for any interactions. This showed that the hydrogels do not form any non-covalent bonds nor stick to tissue after a 20 minutes.

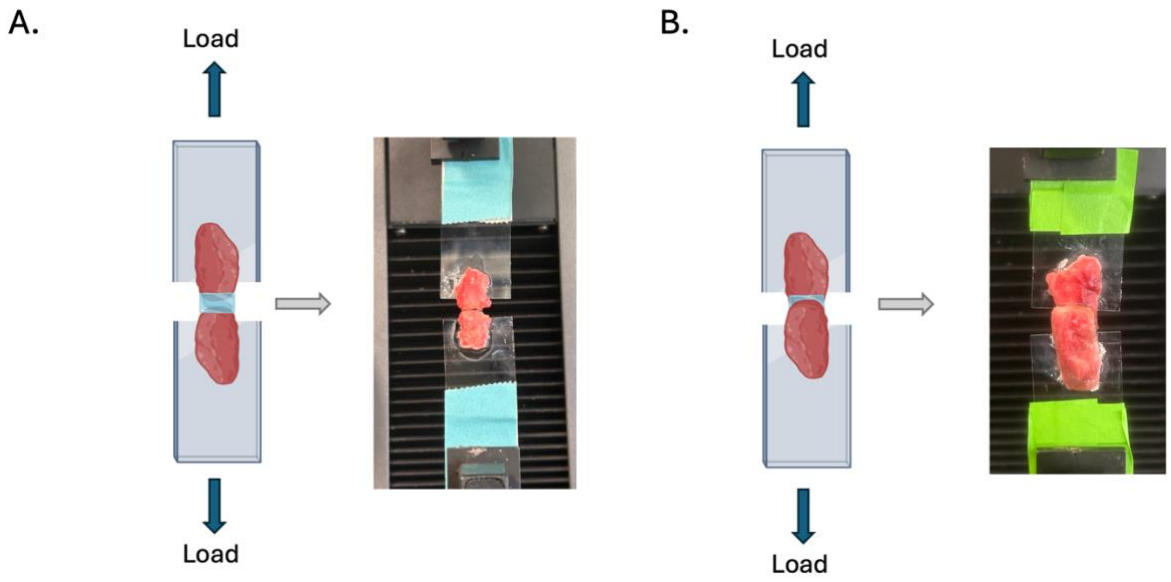

Figure 3. 5. *In vitro* adhesive properties of 3.2% CHIMA gels using pig lung tissue. A) schematic and actual representation of the wound closure test (ASTM F2458-05), B) schematic and actual representation of the modified lap shear test (ASTM F2255-05)

3.3.6 Kinetic release profiles of doxycycline and amlodipine from CHIMA hydrogels

Release of embedded therapeutics from the hydrogel was evaluated using an optimized LC-MS method. Amlodipine was best separated and detected using a fluoro-phenyl column due to its high selectivity for halogenated compounds[42]. Its presence in each LC trace was confirmed via electrospray ionization mass spectrometry (ESI-MS), as shown in **Fig S.3.6.** However, there were two challenges faced when working with doxycycline namely its incorporation into the hydrogel network and its detection. For DOX incorporation, we observed that when a stock solution of DOX was added to the hydrogel formulation, a weaker gel that had a longer crosslinking time was formed. We hypothesized that it stemmed from either the presence of hydroxyl groups on its structure or

its light absorption. Respectively, these two phenomena may occur by hydroxyl group scavenging of free radicals formed from the photoinitiator (irgacure 2959) or by competition of light absorption between DOX and irgacure 2959. To test the latter, we attempted polymerization using a redox initiation system (APS and TEMED), thereby eliminating the possibility that doxycycline was competing for light absorption during photoinitiation. Here we observed that switching from a photoinitiator to a redox initiator did not change polymerization outcomes, suggesting that changes in polymerization may stem from radical scavenging activity of DOX. To investigate this, we made 0.5% increments in the photoinitiator concentration during hydrogel synthesis and observed improvements in polymerization time and hydrogel mechanical properties. To ensure that after DOX incoporation, hydrogel mechanical properties remained consistent with the blank hydrogels, the changes in elastic modulus were monitored. These results are summarized in **Table 3.4**, which shows how varying initiator concentrations influenced the modulus of the gels. Moving forward with release studies, we used hydrogels synthesized with 1.35% photoinitiator as the modulus observed falls within our desired range.

Table 3. 4. Effect of Irgacure 2959 concentration on the modulus of DOX and AML-loaded hydrogels compared to blank unloaded gels.

I2959 stock concentration (%)	Elastic modulus (kPa)
1.20	25
1.25	31
1.30	37
1.35	40
1.40	27.9
Blank gel (1.00)	51 ± 8.4

Next, DOX detection from the hydrogels also proved to be a challenge. The initial detection method was an adapted HPLC method from Vemula *et al*, involving the seperation of amlodipine and doxycycline in a 40:60 acetonitrile: phosphate buffer pH3 (v/v) solution. The seperation and detection of calibration standards worked well with this method[43]. However, both AML and DOX detection concentrations were inconsistent. To further optimize the detection of DOX alone, we pivoted to LC-MS methods, to eliminate equipment error. In the LC-MS methods, we made mobile phase changes by increasing polarity in efforts to

increase detection, because of the high solubility of DOX in water. **Table S3.1** details the changes in detection methods. We hypothesize that these challenges might be due to an interesting property seen in tetracycline-class antibiotics, such as doxycycline, where they undergo hydrolytic degradation in aqueous media. According to work by Xu et al, doxycycline exhibits pH and temperature dependent hydrolysis that can affect its stability in solution. This degradation typically results in the formation of various cleavage products, including epitetracycline and isotetracycline, which could impact drug release kinetics[44]. The formation of these degradation products *in vitro* could be a limitation when using our LC-MS methods that were established based on DOX standards, as these analyses depend on detecting specific molar masses. Although we have not yet conducted analytical confirmation of this degradation pathway in our hydrogel system, it is one direction for ongoing and future studies.

In contrast to DOX, the optimization of amlodipine detection was successful. We observed a burst release profile that plateaued after 48 hours (**Figure 3.7**), which is suitable for wound dressings intended for replacement every 2-3 days. It is important to note that concentrations of AML lower than 27 μg/ml were non-detectable using LC-MS. To overcome this challenge, each sample was freeze-dried and dissolved in the lowest dissolvable amount of HPLC water (200 μL). Regardless, the data set for lower concentrations may still exhibit some degree of variability.

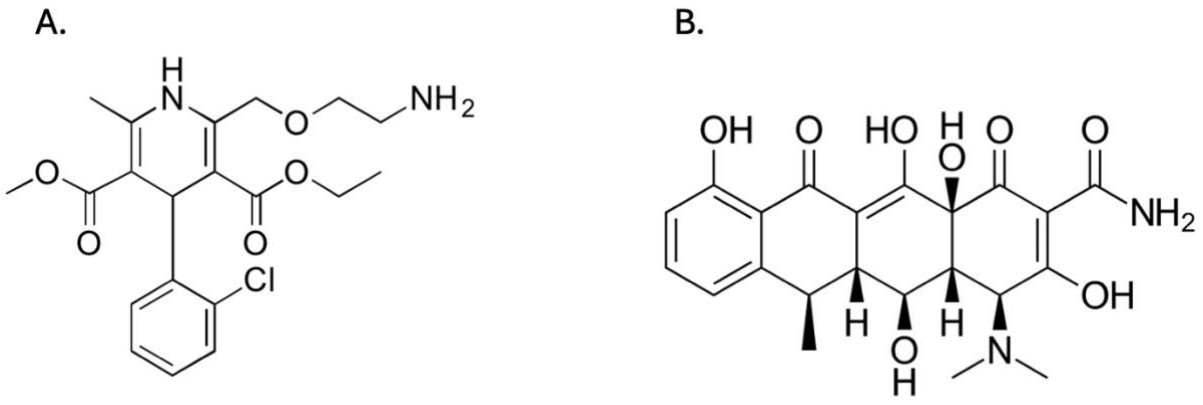

Figure 3. 6. Chemical structures of A) amlodipine and B) doxycycline

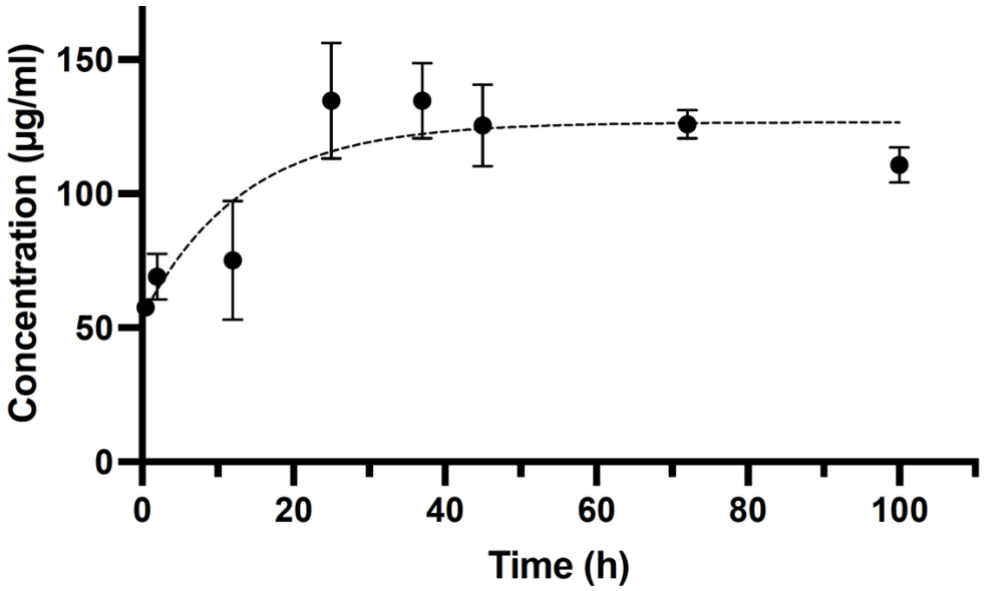

Figure 3. 7. *In vitro* kinetic release of amlodipine from chitosan hydrogels. Concentrations at each timepoint was obtained using an LC-MS standard curve of AUC over concentration (**Fig S3.7**)

3.4 Conclusions

In this work, we have successfully synthesized a hydrogel designed for the enhanced care of sickle cell leg ulcers. Given that chitosan is a widely accessible biopolymer, and considering the demographic most affected by sickle cell anemia, our goal was to develop a therapy that is not only effective but also readily available worldwide. To meet these objectives, we ensured the mechanical robustness of the hydrogel. Since these ulcers typically occur on the lower extremities, daily activities such as walking, running, and engaging in sports can impede healing. A durable hydrogel dressing addresses this challenge by providing mechanical stability in dynamic environments. Additionally, the hydrogel's inherent antimicrobial properties, even in the absence of added antimicrobial agents, create opportunities for versatile applications—with or without supplementary antibiotics. Moreover, its ability to perform optimally in both hydrated and non-hydrated conditions allows for flexible storage and an option for marketing in either wet or dry form. Overall, the biocompatibility of the engineered CHIMA hydrogels

supports their potential translation into clinical use as a viable wound dressing for sickle cell leg ulcers.

3.5 Supplemental information

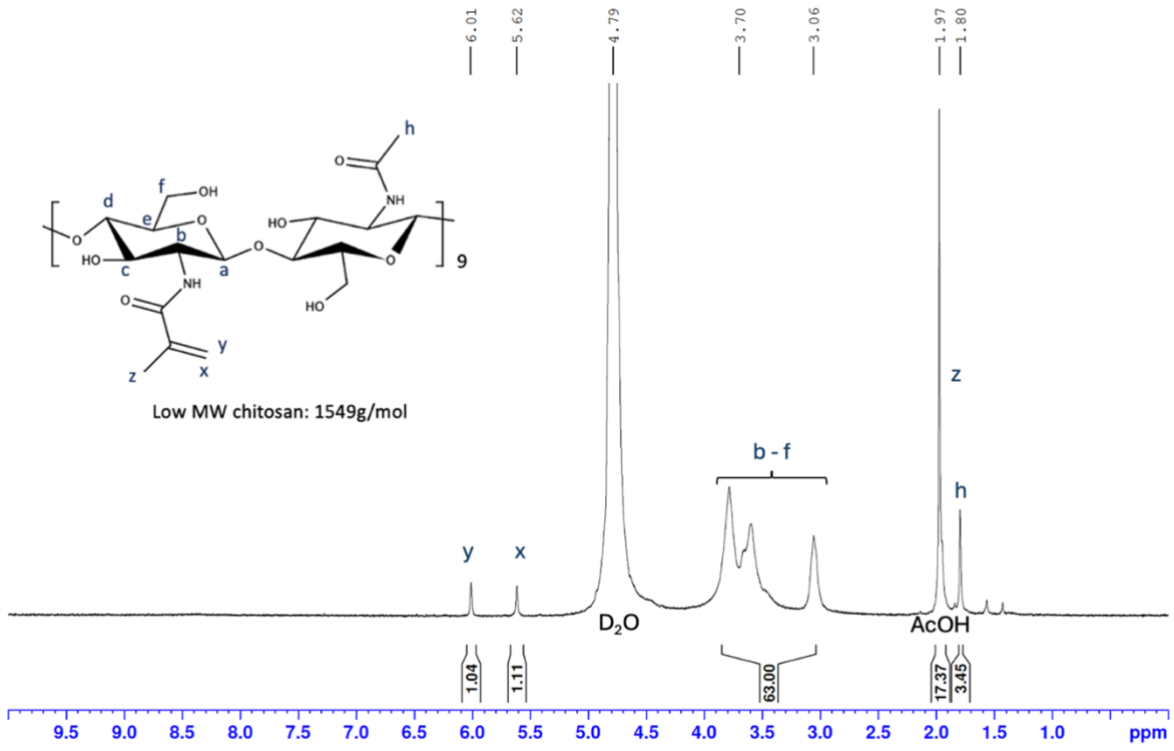

Figure S3.1. [1]HNMR spectrum of chitosan methacrylate (CHIMA). *Methacrylation = 12.2%*

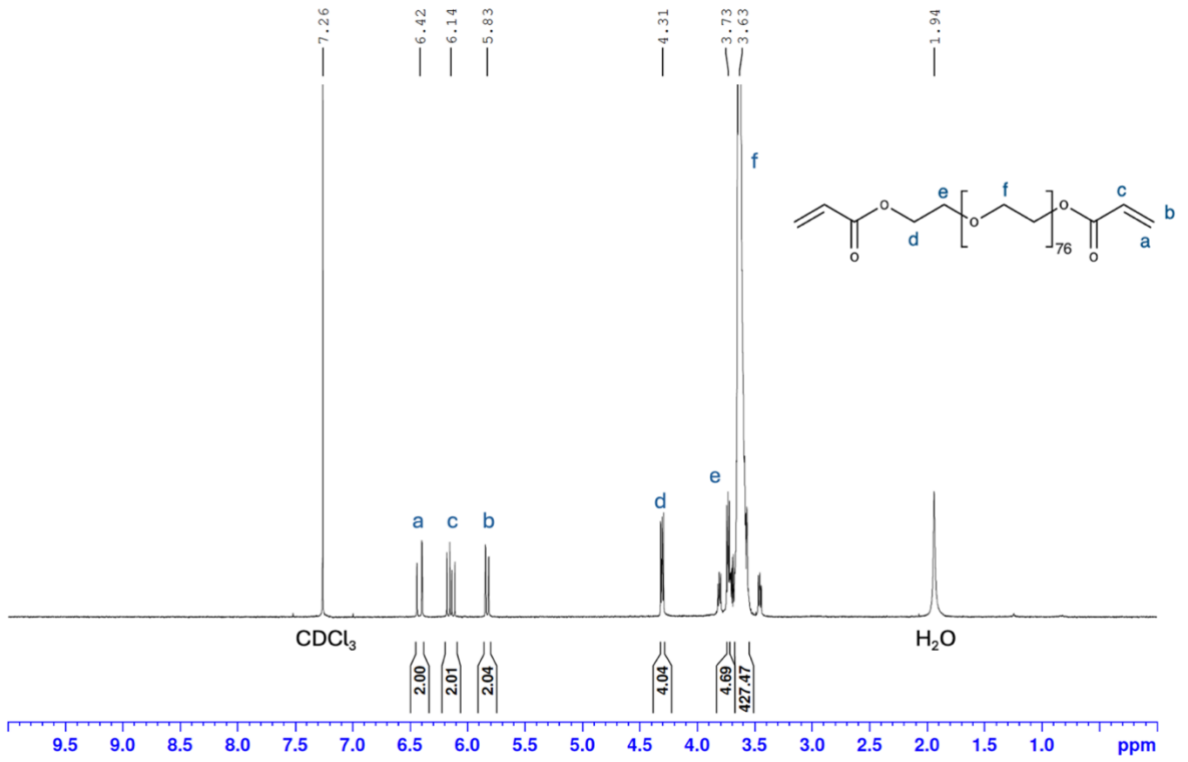

Figure S3.2: [1]HNMR spectrum of poly (ethylene) glycol diacrylate (PEGDA). *Acrylation = 70.3%*

Table S3.1: Final weight percent concentrations of each hydrogel component across all CHIMA hydrogel formulations

Component	**0.8% CHIMA gel**	**3.2% CHIMA gel**	**7.2% CHIMA gel**
CHIMA	0.8	3.2	7.2
PEGDA	15	10	5
Irgacure 2959	0.1	0.1	0.1

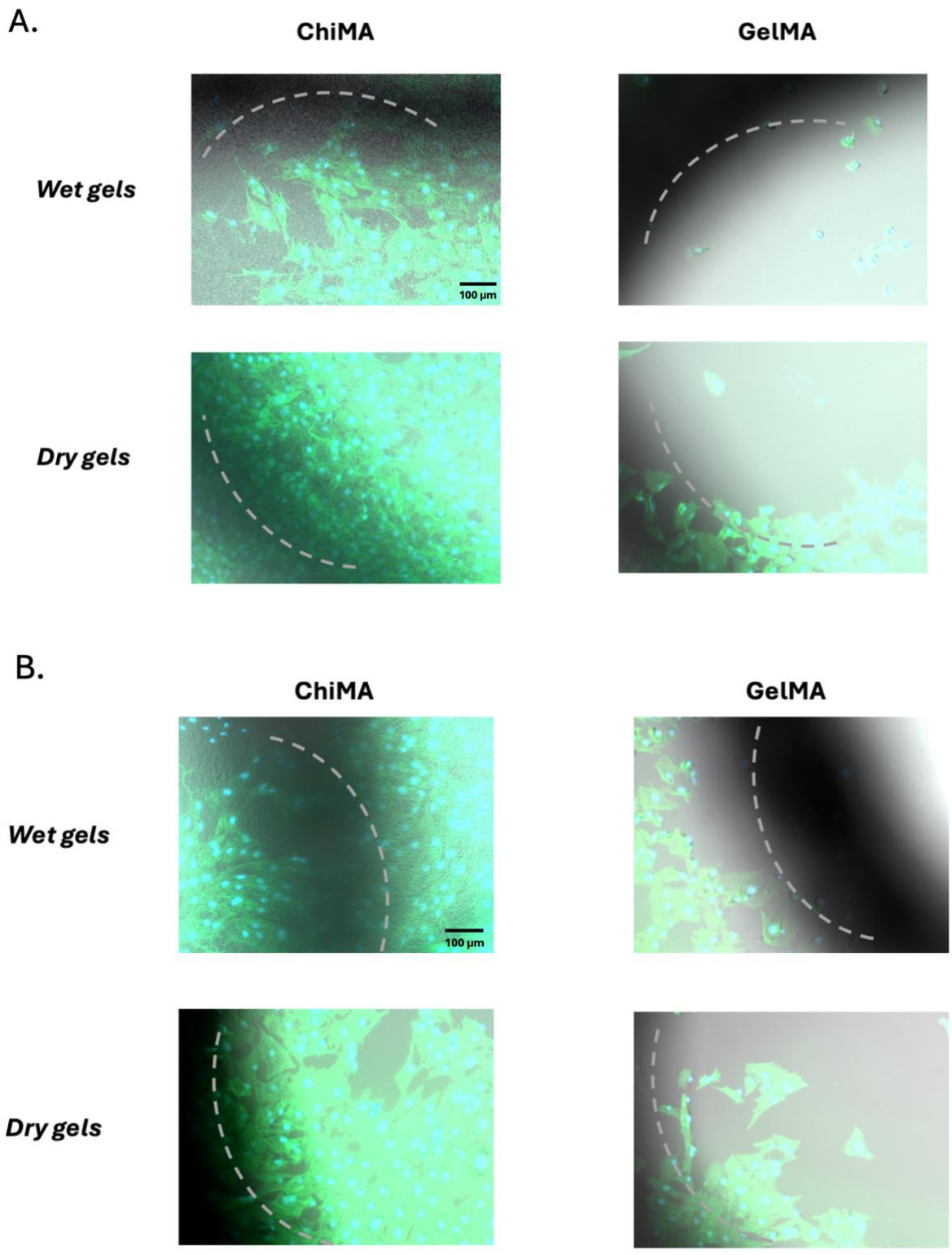

Figure S3.3: Reference phase images showing the outline of hydrogels made by markings before the hydrogel was detached from the cells on the well plate. A) 24-hour timepoint. B) 48-hour timepoint

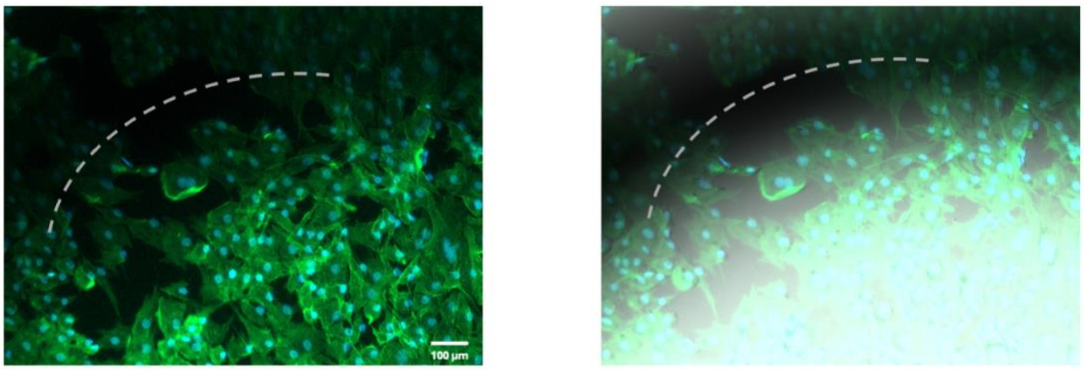

Figure S3.4: Fluorescent microscope images (with phase on the right) showing 48h GelMA samples where cells did not adhere to the gel.

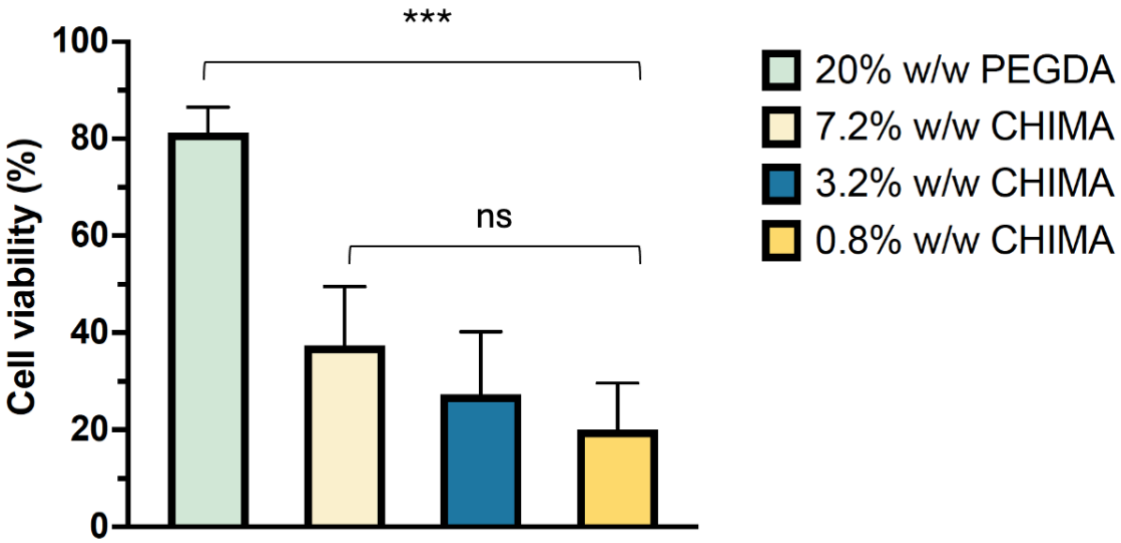

Figure S3.5: PrestoBlue cell viability assay after 24h incubation. Cell viability expressed as a percentage of cell control viability. *Statistically significant differences were found between PEGDA and all CHIMA groups (***P <0.001), no statistical difference was found between the CHIMA groups.*

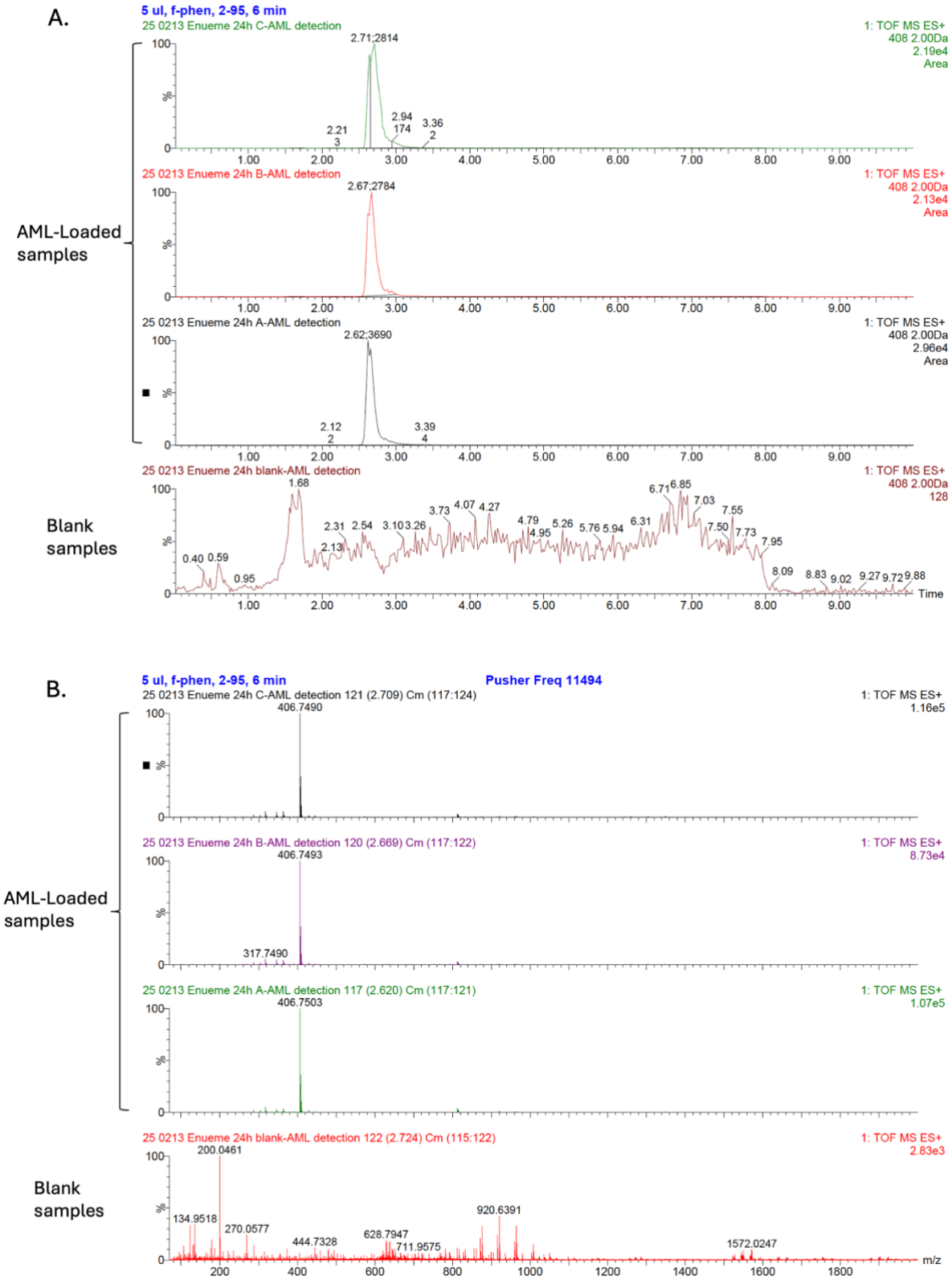

Figure S3.6. An examples of LC curves (A) and MS traces (B) of amlodipine release samples at 24 hours.

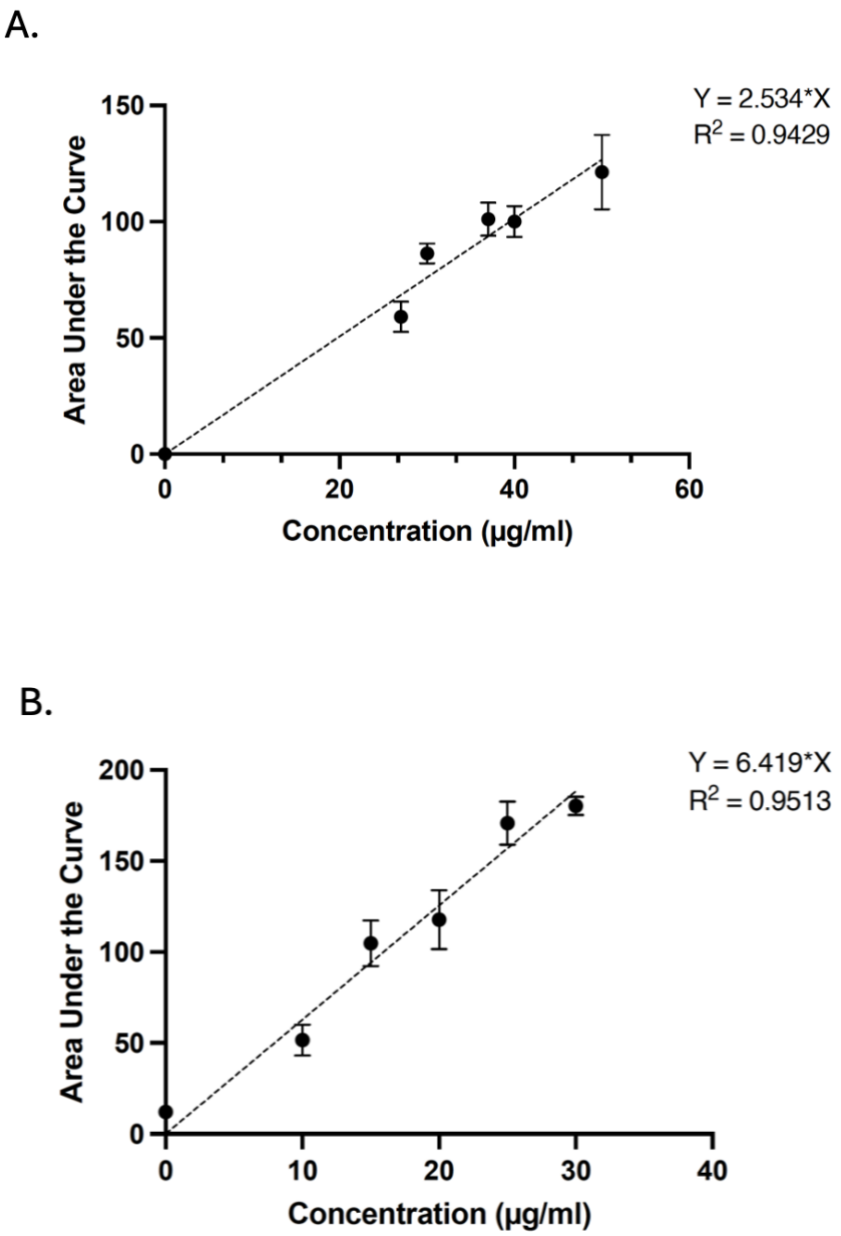

Figure S3.7. LC-MS Calibration curves of amlodipine (A) and doxycycline (B)

Table S3.1. Optimization of doxycycline detection parameters across HPLC and LC-MS methods. This table summarizes the progression of method optimization for doxycycline detection, comparing mobile phase composition, column type, injection volume, flow rate, and detection wavelength across one HPLC and four adapted LC-MS methods. The HPLC, first and third LC-MS method detected doxycycline in standards but not doxycycline released from the hydrogels. The fourth LC-MS method detected amlodipine perfectly[40,42].

HPLC method	**1st adapted LC-MS method**	**2nd adapted LC-MS method**	**3rd adapted LC-MS method**	**4th adapted LC-MS method**
Mobile phase: Acetonitrile: phosphate buffer pH3 40:60 + 0.1% TFA	Mobile phase: Acetonitrile: water 40:60 + 0.2% formic acid	Mobile phase: Gradient Acetonitrile: water 95:5 to 5:95	Mobile phase: Acetonitrile: water 5:95 + 0.2% formic acid	Mobile phase: Gradient Acetonitrile: water 2:98 to 98:2
C18 column	C18 column	C18 column	C18 column	Fluoro-phenyl column
Injection volume: 20ul	Injection volume: 0.5 – 7.5µl (depending on sample conc.)	Injection volume: 0.5 – 7.5µl	Injection volume: 0.5 – 7.5µl	Injection volume: 1 – 5µl
Flow rate: 1 ml/min	Flow rate: 0.1 ml/min	Flow rate: 0.1 ml/min	Flow rate: 0.1 ml/min	Flow rate: 0.3 ml/min
Wavelength: 354nm	Wavelength: 354nm	Wavelength: 354nm	Wavelength: 278nm	Wavelength: 354nm

References

(1) Falanga, V.; Isseroff, R. R.; Soulika, A. M.; Romanelli, M.; Margolis, D.; Kapp, S.; Granick, M.; Harding, K. Chronic Wounds. *Nat. Rev. Dis. Primer* **2022**, *8* (1), 1–21. https://doi.org/10.1038/s41572-022-00377-3.

(2) Catella, J.; Guillot, N.; Nader, E.; Skinner, S.; Poutrel, S.; Hot, A.; Connes, P.; Fromy, B. Controversies in the Pathophysiology of Leg Ulcers in Sickle Cell Disease. *Br. J. Haematol.* **2024**, *205* (1), 61–70. https://doi.org/10.1111/bjh.19584.

(3) Rahim, K.; Saleha, S.; Zhu, X.; Huo, L.; Basit, A.; Franco, O. L. Bacterial Contribution in Chronicity of Wounds. *Microb. Ecol.* **2017**, *73* (3), 710–721. https://doi.org/10.1007/s00248-016-0867-9.

(4) Monfort, J.-B.; Senet, P. Leg Ulcers in Sickle-Cell Disease: Treatment Update. *Adv. Wound Care* **2020**, *9* (6), 348–356. https://doi.org/10.1089/wound.2018.0918.

(5) Minniti, C. P.; Gorbach, A. M.; Xu, D.; Hon, Y. Y.; Delaney, K.-M.; Seidel, M.; Malik, N.; Peters-Lawrence, M.; Cantilena, C.; Nichols, J. S.; Mendelsohn, L.; Conrey, A.; Grimes, G.; Kato, G. J. Topical Sodium Nitrite for Chronic Leg Ulcers in Patients with Sickle Cell Anaemia: A Phase 1 Dose-Finding Safety and Tolerability Trial. *Lancet Haematol.* **2014**, *1* (3), e95–e103. https://doi.org/10.1016/S2352-3026(14)00019-2.

(6) Minniti, C. P.; Kato, G. J.; Garrett, M. E.; Ashley-Koch, A. E.; Telen, M. J. A Phase 2 Prospective Randomized Trial of Topical Sodium Nitrite in Patients with Sickle Cell Disease and Leg Ulcers. *Blood* **2024**, *144*, 2512. https://doi.org/10.1182/blood-2024-199793.

(7) Lipsky, B. A.; Hoey, C. Topical Antimicrobial Therapy for Treating Chronic Wounds. *Clin. Infect. Dis.* **2009**, *49* (10), 1541–1549. https://doi.org/10.1086/644732.

(8) Gounden, V.; Singh, M. Hydrogels and Wound Healing: Current and Future Prospects. *Gels* **2024**, *10* (1), 43. https://doi.org/10.3390/gels10010043.

(9) Lin, X.; Zhang, X.; Wang, Y.; Chen, W.; Zhu, Z.; Wang, S. Hydrogels and Hydrogel-Based Drug Delivery Systems for Promoting Refractory Wound Healing: Applications and Prospects. *Int. J. Biol. Macromol.* **2025**, *285*, 138098. https://doi.org/10.1016/j.ijbiomac.2024.138098.

(10) Serpico, L.; Dello Iacono, S.; Cammarano, A.; De Stefano, L. Recent Advances in Stimuli-Responsive Hydrogel-Based Wound Dressing. *Gels* **2023**, *9* (6), 451. https://doi.org/10.3390/gels9060451.

(11) Rippon, M. G.; Ousey, K. Hydro-Responsive Wound Dressing (HRWD): Clinical and Scientific Monograph.

(12) Zhou, W.; Zi, L.; Cen, Y.; You, C.; Tian, M. Copper Sulfide Nanoparticles-Incorporated Hyaluronic Acid Injectable Hydrogel With Enhanced Angiogenesis to Promote Wound Healing. *Front. Bioeng. Biotechnol.* **2020**, *8*. https://doi.org/10.3389/fbioe.2020.00417.

(13) Sadler, G. M.; Wallace, H. J.; Stacey, M. C. Oral Doxycycline for the Treatment of Chronic Leg Ulceration. *Arch. Dermatol. Res.* **2012**, *304* (6), 487–493. https://doi.org/10.1007/s00403-011-1201-5.

(14) De Mori, A.; Di Gregorio, E.; Kao, A. P.; Tozzi, G.; Barbu, E.; Sanghani-Kerai, A.; Draheim, R. R.; Roldo, M. Antibacterial PMMA Composite Cements with Tunable Thermal and Mechanical Properties. *ACS Omega* **2019**, *4* (22), 19664–19675. https://doi.org/10.1021/acsomega.9b02290.

(15) Zanon, M.; Chiappone, A.; Garino, N.; Canta, M.; Frascella, F.; Hakkarainen, M.; Pirri, C. F.; Sangermano, M. Microwave-Assisted Methacrylation of Chitosan for 3D Printable Hydrogels in Tissue Engineering. *Mater. Adv.* **2022**, *3* (1), 514–525. https://doi.org/10.1039/D1MA00765C.

(16) Käpylä, E.; Delgado, S. M.; Kasko, A. M. Shape-Changing Photodegradable Hydrogels for Dynamic 3D Cell Culture. *ACS Appl. Mater. Interfaces* **2016**, *8* (28), 17885–17893. https://doi.org/10.1021/acsami.6b05527.

(17) Pumford, E. A.; Jackson Hoffman, B. A.; Kasko, A. M. Nontoxic Initiator Alternatives to TEMED for Redox Hydrogel Polymerization. *ACS Appl. Bio Mater.* **2024**, *7* (4), 2264–2271. https://doi.org/10.1021/acsabm.3c01264.

(18) Song, A.; Rane, A. A.; Christman, K. L. Antibacterial and Cell-Adhesive Polypeptide and Poly(Ethylene Glycol) Hydrogel as a Potential Scaffold for Wound Healing. *Acta Biomater.* **2012**, *8* (1), 41–50. https://doi.org/10.1016/j.actbio.2011.10.004.

(19) Berger, J.; Reist, M.; Mayer, J. M.; Felt, O.; Peppas, N. A.; Gurny, R. Structure and Interactions in Covalently and Ionically Crosslinked Chitosan Hydrogels for Biomedical Applications. *Eur. J. Pharm. Biopharm.* **2004**, *57* (1), 19–34. https://doi.org/10.1016/S0939-6411(03)00161-9.

(20) Vigata, M.; Meinert, C.; Bock, N.; Dargaville, B. L.; Hutmacher, D. W. Deciphering the Molecular Mechanism of Water Interaction with Gelatin Methacryloyl Hydrogels: Role of Ionic Strength, pH, Drug Loading and Hydrogel Network Characteristics. *Biomedicines* **2021**, *9* (5), 574. https://doi.org/10.3390/biomedicines9050574.

(21) Uyanga, K. A.; Daoud, W. A. Carboxymethyl Cellulose-Chitosan Composite Hydrogel: Modelling and Experimental Study of the Effect of Composition on Microstructure and Swelling Response. *Int. J. Biol. Macromol.* **2021**, *181*, 1010–1022. https://doi.org/10.1016/j.ijbiomac.2021.04.117.

(22) Li, C.-P.; Weng, M.-C.; Huang, S.-L. Preparation and Characterization of pH Sensitive Chitosan/3-Glycidyloxypropyl Trimethoxysilane (GPTMS) Hydrogels by Sol-Gel Method. *Polymers* **2020**, *12* (6), 1326. https://doi.org/10.3390/polym12061326.

(23) Huang, J.; Zajforoushan Moghaddam, S.; Maroni, P.; Thormann, E. Swelling Behavior, Interaction, and Electrostatic Properties of Chitosan/Alginate Dialdehyde Multilayer Films with Different Outermost Layer. *Langmuir* **2020**, *36* (14), 3782–3791. https://doi.org/10.1021/acs.langmuir.0c00330.

(24) Hasan, S.; Boddu, V. M.; Viswanath, D. S.; Ghosh, T. K. Chitosan Characterization. In *Chitin and Chitosan: Science and Engineering*; Hasan, S., Boddu, V. M., Viswanath, D. S., Ghosh, T. K., Eds.; Springer International Publishing: Cham, 2022; pp 51–78. https://doi.org/10.1007/978-3-031-01229-7_3.

(25) Shirzaei Sani, E.; Kheirkhah, A.; Rana, D.; Sun, Z.; Foulsham, W.; Sheikhi, A.; Khademhosseini, A.; Dana, R.; Annabi, N. Sutureless Repair of Corneal Injuries Using Naturally Derived Bioadhesive Hydrogels. *Sci. Adv.* **2019**, *5* (3), eaav1281. https://doi.org/10.1126/sciadv.aav1281.

(26) Ghovvati, M.; Baghdasarian, S.; Baidya, A.; Dhal, J.; Annabi, N. Engineering a Highly Elastic Bioadhesive for Sealing Soft and Dynamic Tissues. *J. Biomed. Mater. Res. B Appl. Biomater.* **2022**, *110* (7), 1511–1522. https://doi.org/10.1002/jbm.b.35012.

(27) Cebe, T.; Ahuja, N.; Monte, F.; Awad, K.; Vyavhare, K.; Aswath, P.; Huang, J.; Brotto, M.; Varanasi, V. Novel 3D-Printed Methacrylated Chitosan-Laponite Nanosilicate Composite Scaffolds Enhance Cell Growth and Biomineral Formation in MC3T3 Pre-Osteoblasts. *J. Mater. Res.* **2020**, *35* (1), 58–75. https://doi.org/10.1557/jmr.2018.260.

(28) Kalra, A.; Lowe, A.; Al-Jumaily, A. Mechanical Behaviour of Skin: A Review. *J. Mater. Sci. Eng.* **2016**.

(29) Saeki, J.; Ikezoe, T.; Nakamura, M.; Nishishita, S.; Ichihashi, N. The Reliability of Shear Elastic Modulus Measurement of the Ankle Plantar Flexion Muscles Is Higher at Dorsiflexed Position of the Ankle. *J. Foot Ankle Res.* **2017**, *10* (1), 18. https://doi.org/10.1186/s13047-017-0199-0.

(30) Annaka, M.; Tanaka, T. Multiple Phases of Polymer Gels. *Nature* **1992**, *355* (6359), 430–432. https://doi.org/10.1038/355430a0.

(31) Bajpai, A. K.; Shukla, S. K.; Bhanu, S.; Kankane, S. Responsive Polymers in Controlled Drug Delivery. *Prog. Polym. Sci.* **2008**, *33* (11), 1088–1118. https://doi.org/10.1016/j.progpolymsci.2008.07.005.

(32) Goycoolea, F. M.; Heras, A.; Aranaz, I.; Galed, G.; Fernández-Valle, M. E.; Argüelles-Monal, W. Effect of Chemical Crosslinking on the Swelling and Shrinking Properties of Thermal and pH-Responsive Chitosan Hydrogels. *Macromol. Biosci.* **2003**, *3* (10), 612–619. https://doi.org/10.1002/mabi.200300011.

(33) Lopez, C. G.; Lohmeier, T.; Wong, J. E.; Richtering, W. Electrostatic Expansion of Polyelectrolyte Microgels: Effect of Solvent Quality and Added Salt. *J. Colloid Interface Sci.* **2020**, *558*, 200–210. https://doi.org/10.1016/j.jcis.2019.07.042.

(34) Lai, F.; Li, H. Transient Modeling of the Reversible Response of the Hydrogel to the Change in the Ionic Strength of Solutions. *Mech. Mater.* **2011**, *43* (6), 287–298. https://doi.org/10.1016/j.mechmat.2011.03.001.

(35) Yan, D.; Li, Y.; Liu, Y.; Li, N.; Zhang, X.; Yan, C. Antimicrobial Properties of Chitosan and Chitosan Derivatives in the Treatment of Enteric Infections. *Molecules* **2021**, *26* (23), 7136. https://doi.org/10.3390/molecules26237136.

(36) (PDF) The Combination Effect of Curcumin with Different Antibiotics against Staphylococcus Aureus. *ResearchGate* **2024**.

(37) *(PDF) Natural extracts and honey based impregnated gauze wound dressing preparation and in vitro antibacterial efficacy*. ResearchGate. https://www.researchgate.net/publication/323560534_Natural_extracts_and_honey_based_impregnated_gauze_wound_dressing_preparation_and_in_vitro_antibacterial_efficacy (accessed 2025-04-10).

(38) Yao, H.; Wu, M.; Lin, L.; Wu, Z.; Bae, M.; Park, S.; Wang, S.; Zhang, W.; Gao, J.; Wang, D.; Piao, Y. Design Strategies for Adhesive Hydrogels with Natural Antibacterial Agents as Wound Dressings: Status and Trends. *Mater. Today Bio* **2022**, *16*, 100429. https://doi.org/10.1016/j.mtbio.2022.100429.

(39) Liang, Y.; Li, Z.; Huang, Y.; Yu, R.; Guo, B. Dual-Dynamic-Bond Cross-Linked Antibacterial Adhesive Hydrogel Sealants with On-Demand Removability for Post-

Wound-Closure and Infected Wound Healing. *ACS Nano* **2021**, *15* (4), 7078–7093. https://doi.org/10.1021/acsnano.1c00204.

(40) Liu, X.; Qin, S.; Xu, L.; Fu, G.; Huang, Y.; Yu, C.; Cheng, G.; Li, Y.; He, Y.; Qi, Y.; Sun, D. A Tough and Mechanically Stable Adhesive Hydrogel for Non-Invasive Wound Repair. *Front. Bioeng. Biotechnol.* **2023**, *11*. https://doi.org/10.3389/fbioe.2023.1173247.

(41) Farahani, M.; Shafiee, A. Wound Healing: From Passive to Smart Dressings. *Adv. Healthc. Mater.* **2021**, *10* (16), 2100477. https://doi.org/10.1002/adhm.202100477.

(42) Amoura, C.; Larvor, F.; Marchand, P.; Bizec, B. L.; Cariou, R.; Bichon, E. Quantification of Chlorinated Paraffins by Chromatography Coupled to High-Resolution Mass Spectrometry – Part B: Influence of Liquid Chromatography Separation. *Chemosphere* **2024**, *352*, 141401. https://doi.org/10.1016/j.chemosphere.2024.141401.

(43) Vemula, K.; Ponnuswamy, N. K. Method Development And Validation For Simultaneous Estimation Of Amlodipine Besylate And Telmisartan In Bulk And Pharmaceutical Formulation By RP-HPLC. *World J. Pharm. Res. 8* (13).

(44) Zhong, S.-F.; Yang, B.; Xiong, Q.; Cai, W.-W.; Lan, Z.-G.; Ying, G.-G. Hydrolytic Transformation Mechanism of Tetracycline Antibiotics: Reaction Kinetics, Products Identification and Determination in WWTPs. *Ecotoxicol. Environ. Saf.* **2022**, *229*, 113063. https://doi.org/10.1016/j.ecoenv.2021.113063.

Chapter 4: Hydrogel Wound Dressings for Prolonged Field Care in Austere Environments

4.1 Introduction

Extremity injuries remain the most common cause of battlefield trauma and the leading cause of long-term disability secondary to diminished function, infection and delayed amputation[1]. One of the major demands in battlefield trauma care is minimizing the time between critical injury and definitive care. This has been partly addressed by the "golden hour policy" where transport time for treatment in these scenarios have been halved. However, the evacuation of significantly injured military personnel to a treatment facility within 60 minutes is often not possible for those who are deployed to remote & austere locations for prolonged periods[2]. These limitations have led to the advent of prolonged field care (PFC), a strategy that provides on-site medical intervention to stabilize patients until they can be successfully transported to a medical facility[3].

One of the primary concerns in battlefield wounds is susceptibility to infection. Bacterial species, primarily *Staphylococcus aureus*, *Escherichia coli*, and *Pseudomonas spp*. are known to colonize battlefield wounds either on-site, en route to treatment facilities, or from the patient's own micro-flora[4,5]. Furthermore, these microbes can co-exist and display synergistic interactions which enhances colonization and persistence, increasing risk of amputation and mortality[6–8]. Another major challenge is hemorrhage which accounts for ~50% of preventable combat-related deaths. Treatment can be particularly difficult as evacuation from the combat zone may be delayed. Additionally, pain management strategies typically rely on intramuscular morphine, which has been found inadequate for severe wounds and can cause respiratory depression with repeated dosing[9]. Addressing these challenges in PFC requires solutions that prevent infection, control hemorrhage and provide both immediate and sustained pain relief under real-world constraints[10,11].

For PFC wound dressings to be effective, they should be lightweight, form almost instantaneously, conform to the wound bed, and be rugged and durable. Hydrogels have a great potential to serve simultaneously as PFC wound dressings and drug delivery vehicles. As detailed in **section 3.1**, they are highly tunable, biocompatible and have adequate moisture retention which are great components to enhance wound healing. PEG-based hydrogels in particular, have gained attention for their ability to mimic the chemical and physical properties of the native extracellular matrix, making them excellent candidates for active wound healing[12,13]. By tuning the properties of hydrogels (such as cross-link density or mesh-size), the diffusion of entrapped therapeutic agents out of the wound dressing can be tailored, thus allowing the delivery of therapeutic agents in a sustained manner. To address the potential for polymicrobial infections, dual-antibiotic therapy can be employed using a combination of tobramycin and vancomycin[14]. When used together, these antibiotics have also demonstrated increased bone defect re-ossification, particularly relevant for blast injuries associated with fracture[15]. Additionally, tranexamic acid (TXA), an antifibrinolytic agent can be employed to reduce blood loss, significantly reducing mortality in trauma patients with bleeding[16,17]. For pain management local anesthetics such as lidocaine provide an alternative to opioids, eliminating risks of addiction and abuse while also avoiding the bleeding complications associated with nonsteroidal anti-inflammatory drugs.

This study aims to utilize hydrogel engineering methods as discussed in Chapter 3, to address challenges in battlefield trauma. The proposed system - a field polymerizable hydrogel capable of multi-drug delivery (with vancomycin, tobramycin, TXA and lidocaine) offers a robust, multifunctional wound dressing for PFC applications. By bridging polymer design, *in vivo* validation, and large animal studies (**Fig. 4.1**), this work seeks to translate biomaterial research into practical solutions for battlefield trauma care.

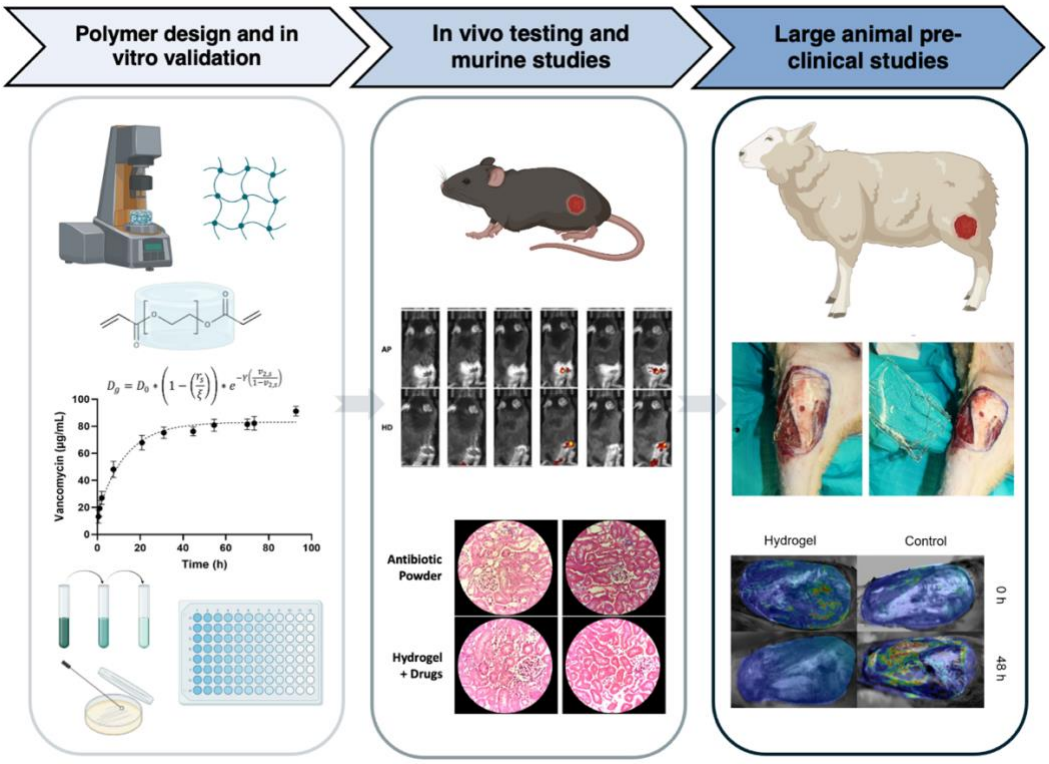

Figure 4. 1. Research workflow diagram illustrating the sequential steps to develop and validate our hydrogel platform.

4.2 Materials and methods

Polyethylene glycol 3350 g/mol (Integra Chemicals), acryloyl chloride (Sigma, ≥97%), triethylamine (Sigma, ≥ 99%), dichloromethane (Fisher Scientific, ≥99.5%), potassium carbonate (K_2CO_3, Fisher Scientific, 99.3%), anhydrous magnesium sulfate ($MgSO_4$, Fisher Scientific), ether (Fisher Scientific, 99%), deuterated chloroform (Fisher Scientific, 99.8%), ammonium persulfate (APS, Amresco, ACS Grade), tetramethylethylenediamine (TEMED, Amresco, ≥99%), vancomycin (Fisher Scientific, ≥80%), lidocaine (Fisher Scientific), tranexamic acid (Fisher Scientific, ≥98%), tobramycin (Fisher Scientific, ≥94%), LB broth, Miller (Fisher BioReagents), phosphate buffered saline, PBS (VWR), acetonitrile, HPLC grade (Fisher scientific, 99.95%), water, HPLC grade (Fisher scientific), trifluoroacetic acid, TFA (Avantor, 99.5%).

4.2.1 Synthesis of poly (ethylene glycol) diacrylate (PEGDA) and PEGDA hydrogels

PEGDA was synthesized using the same procedure discussed in **section 3.2.2**. Each batch was individually tested to ensure at least 75% conversion and a gelation time of ≤ 2 minutes (**Fig. S4.1**). For PEGDA hydrogel synthesis, final concentrations of PEGDA, and initiators (APS and TEMED) were kept consistent for *in vitro* and *in vivo* experiments. For all hydrogels, final reagent concentrations were: 24.14 wt% PEGDA, 30 mM APS, and 30 mM TEMED. PEGDA was diluted to 35.5 wt% in DI H_2O and vortexed until dissolved. TEMED and APS were diluted to 1 M, prepared fresh prior to each use. To prepare a 1 mL hydrogels precursor solution, 680 µL 35.5 wt% PEGDA and 260 µL DI H_2O or drug stock solution were combined in an Eppendorf tube. To initiate crosslinking, 30 µL 1 M TEMED and 30 µL 1 M APS were added. For murine and large animal experiments, hydrogel volumes were changed to scaled up to 300 µL and 35 mL respectively.

4.2.2 Drug stock solutions

Fresh aqueous stock solutions were prepared for each therapeutic agent. The drugs concentrations were determined based on detectability for in vitro experiments while in vivo dosages were adjusted according to animal weight. For *in vitro* experiments, the following concentrations were used 5.2 mg/mL vancomycin, 92.9 mg/mL tobramycin, 191.6 mg/mL tranexamic acid, 10.5 mg/mL lidocaine. For *in vivo* murine studies, each hydrogel contained 4 mg vancomycin, 4.57 mg tobramycin, 5.56 mg tranexamic acid, and 1.38 mg lidocaine. The mass of each therapeutic agent added was kept constant, regardless of final hydrogel volume. For i*n vivo* Merino sheep studies, the hydrogel formulations included 537.5 mg vancomycin, 638.98 mg tobramycin, 777.87 mg tranexamic acid, and 192.5 mg lidocaine. The amount of therapeutics administered in animal studies was calculated based on published therapeutic dosing guidelines and the weight (kg) of each animal.

4.2.3 Characterization of Hydrogels

Mechanical characterization was performed on hydrogels fabricated using a range of PEGDA molecular weights to evaluate elastic moduli and swelling ratios. Mass swelling ratios were calculated by taking the ratio of swollen hydrogel mass to the dry hydrogel mass following lyophilization. A dynamic mechanical analyzer (Q-800, TA Instruments – New Castle, DE, USA) was used to measure the elastic modulus of hydrogels. Using a uniaxial compression test, the initial preload force was set to 0.001 N and the initial strain was set to 0.5%, and the system ramped the strain 2.5%/min to a maximum strain of -20%. The linear region of the stress-strain curve was used to calculate elastic modulus. This aspect of our collaborative work was done solely by Dr. Elizabeth Pumford (PhD).

4.2.4 *In vitro* release study of embedded therapeutics

The release of vancomycin, lidocaine, tranexamic acid and tobramycin from hydrogels were evaluated using an *in vitro* release study model. 1 mL PEGDA hydrogels were synthesized with the specified reagents and concentrations detailed in **section 4.2.1**. To prevent premature polymerization, the pre-polymer solution was prepared by sequentially adding the following components in the specified order – PEGDA solution, water or drug stock solution, APS solution and then the TEMED solution . The solution was then quickly mixed and cast between a glass slide with a 2mm thickness. After gelation, the hydrogels were precisely cut into 2 x 6 mm cylindrical discs using a biopsy punch. Each hydrogel disc was placed in 48-well plates and incubated in 1 mL deionized water at room temperature. At predetermined time points, the hydrogel supernatant was collected and absorbance was measured using a UV-visible spectrophotometer (Biomate 3S, Thermo Scientific – Waltham, MA, US). The drug concentration in each hydrogel was determined using a standard curve (**Fig. S4.1)** . Each time point was done in triplicate and blank hydrogels (drug-free) served as controls. Tobramycin

and tranexamic acid lack UV absorbing chromophores, necessitating alternative detection approaches. A ferric chloride assay was used to detect tobramycin and tranexamic acid. This work was done in collaboration with Dr. Elizabeth Pumford (PhD).

4.2.5 Assessing multi-drug release: HPLC and Mass Spectrometry analysis

To confirm the ability of our hydrogels to simultaneously release multiple therapeutics, we employed chromatographic and spectrometric techniques for analysis. The hydrogels used for this study was synthesized as described above, with the only modification being the incorporation of all therapeutics into each 1 mL hydrogel. The chromatographic system consisted of Jasco (Tokyo, Japan) PU-2087 dual plunger pump, a high pressure dynamic mixer (Jasco, MX-2080-32) and a UV-visible tunable absorbance detector (Jasco UV-2075). The chromatograms were recorded using ChromNAV software (Jasco, Japan) to quantify peak heights and entire data analysis and processing. The separation of the therapeutics (vancomycin and lidocaine) were achieved using a 4.6 x 250 mm, 5 μm particle size, C18 column. The mobile phase consisted of a 70:30 (v/v) isocratic mixture of HPLC-grade water and acetonitrile. The mobile phase was mixed with 0.1% trifluoroacetic acid and degassed via sonication for 30 minutes at room temperature. The flow rate was set at 0.5 mL/min. The UV detection wavelength was set at 240 nm (an average between UV_{max} of vancomycin and lidocaine). The injection volume was 20 μL with a total run time of 15 minutes[18–20].

For mass spectrometry analysis, the samples were infused using a direct-loop injection on a Waters Acquity UPLC system, separated using an Acquity BEH 50 x 2.1 mm, 1.7 um particle size C18 column, and eluted with a gradient of 3 – 95% solvent A and B over 15 min (solvent A: water, solvent B: acetonitrile, with 0.3% and 0.2% formic acid respectively (v/v)). Mass spectra were recorded from a mass of 300–2000 Da. To ensure accuracy and optimal calibration of these methods, standard curves for each therapeutic were plotted (**Fig. S4.2)**. ESI-TOF measurements were carried out on a Waters LCT-Premier XE Time of Flight

Instrument controlled by MassLynx 4.1 software (Waters Corporation, Milford MA). The instrument was equipped with the Multi Mode Ionization source operated in the electrospray mode. A solution of Leucine Enkephalin (Sigma Chemical, L9133) was used in the Lock-Spray.

4.2.6 Calibration and accuracy

Calibration curves for each therapeutic was generated using a series of standard samples with pre-determined concentrations relevant to the expected release. The linearity of the standard curve was created by plotting absorbance (for UV-vis) or the peak area (for HPLC) against the analyte concentration. These curves were fitted by a simple linear regression. (**Fig. S4.1, S4.2**)

4.2.7 Efficacy of released antibiotics: A broth microdilution assay

A broth microdilution assay was conducted to confirm that antibiotics released from the hydrogel system retained their antimicrobial activity. Hydrogels containing no drugs, vancomycin (V), tobramycin (T), or a combination of vancomycin and tobramycin (V+T) in PEGDA hydrogels were prepared following previously described methods. To quantify antibiotic release, hydrogel sample discs were incubated at room temperature in 500 μL PBS for 5 days. The concentration of vancomycin and tobramycin released from each disc was quantified using UV-Vis spectroscopy. This measured drug concentrations were used as the starting point for the assay. Subsequent well plates contained nine serial dilutions of the total drug released from the gel (**Fig. S4.3**) The eluents were then tested in an LB broth microdilution assay using *E. coli* (MG1655) and *S. aureus* (SA113) at an initial burden of 5×10^5 CFU/mL, with sterile media control and growth controls included. After incubating at 37°C for 18 h, the plates were examined to determine the minimum inhibitory concentration (MIC). The MICs of tobramycin and vancomycin released from hydrogels containing each antibiotic alone were

quantified for *E. coli* and *S. aureus*, respectively. These were then compared to the MICs of antibiotics released from the dual-antibiotic-loaded hydrogels[21]. This work was done in collaboration with Dr. Elizabeth Pumford (PhD).

4.2.8 Efficacy of drug release

To test the efficacy of drug release, hydrogels used for murine infection studies were explanted and evaluated for the presence of unreleased therapeutics. To accomplish this, the hydrogels were subjected to three extraction cycles and analyzed via HPLC and mass spectrometry. Briefly, the gels were placed in Eppendorf tubes containing 500 µl ethanol as an extraction solvent for 24 hours. The tubes were capped, covered with parafilm to prevent evaporation and incubated at 8°C. After 24 hours, ethanol was removed and replaced with 500 µl methanol for 2 hours at 8°C, this was repeated twice to complete the second and third extraction cycles. The collected extraction solvents were then concentrated using a rotary evaporator and redispersed in HPLC solvents for analysis. The samples received from our collaborators in the Bernthal group included an infected group and a sterile group which were murine open fracture models inoculated with and without *S. aureus*, *E. coli*, and *P. aeruginosa* respectively.

4.3 Results and discussion

4.3.1 Synthesis of PEGDA hydrogels

The PEGDA hydrogels used in this study were scaled up from *in vitro* experiments, where 56.5µl hydrogels were used, to *in vivo* animal studies which required 300 µl for murine experiments and 35mL hydrogels for sheep studies. For the sheep studies, our collaborators in the Wenke group developed a trapezoidal full-thickness wound model with a surface area of 35 cm^2. To ensure effective and timely curing of the hydrogels to the wound bed, we designed

a polyoxymethylene mold using Fusion 360 (Autodesk, USA) and fabricated it via (Computer Numerical Control) CNC machining for high precision. The 3D model design was developed collaboratively with James Popoli and Shannon Li (**Fig. 4.2a**). Gelation times for the 35 mL hydrogels were consistently within 3 minutes. Notably, blank hydrogels exhibited faster gelation compared to drug-loaded hydrogels (**Fig. 4.2b, c**). We presume that this is due to factors like steric hindrance caused by high-molecular weight therapeutics such as vancomycin (1,449.3 g/mol), which may obstruct the proximity required for polymer chains to cross-link potentially slowing down the polymerization process[22,23].

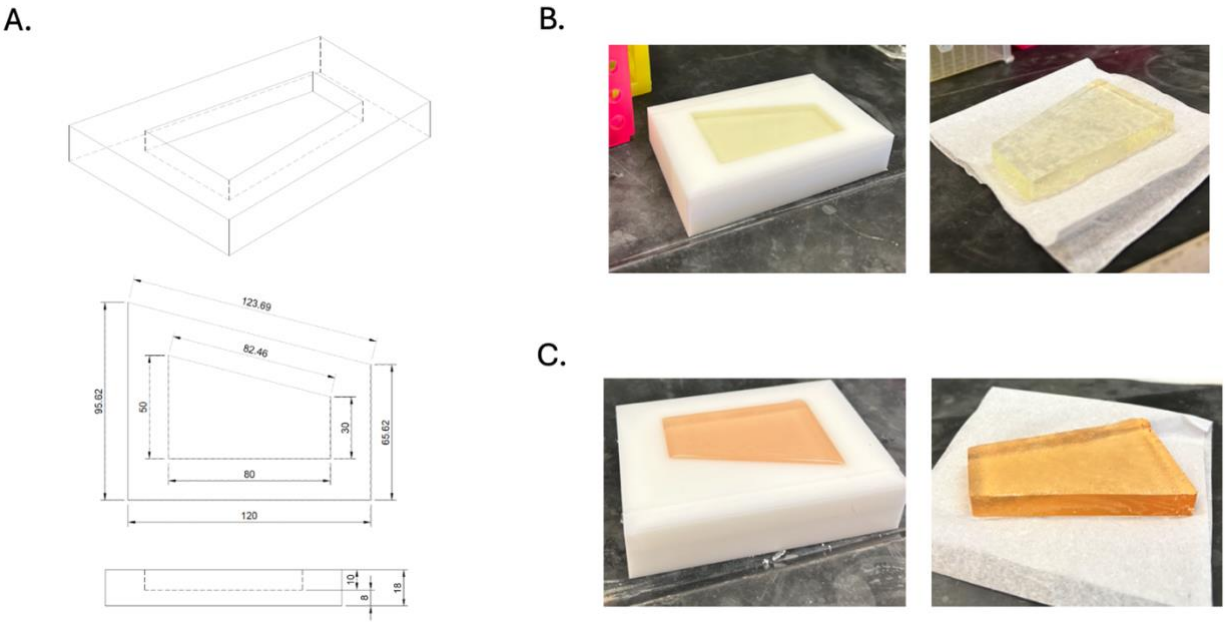

Figure 4. 2. Design and synthesis of 35mL hydrogels for large animal studies. A) Fusion 360 design of 3D mold. B) Blank hydrogels cured in the polyoxymethylene mold. C) Drug-loaded hydrogels

4.3.2 Mechanical characterization of PEGDA hydrogels

Due to variations that can be seen between predicted and observed hydrogel mesh sizes, more accurate release profiles can be obtained by experimentally determining hydrogel mesh

size. PEGDA of varying molecular weights was crosslinked using the redox initiating system of APS and TEMED, which produce free radicals when mixed in solution. Elastic moduli and swelling ratios can be used to estimate hydrogel mesh size, which determines diffusion rates of therapeutic agents. Elastic moduli decrease as a function of increasing PEGDA molecular weight, which is consistent with computational models. Conversely, mass swelling ratios (Q_m) increased with PEGDA molecular weight. The Flory-Rehner theory was also used to calculate volumetric swelling ratios, Q_v, of hydrogels fabricated using different molecular weight PEGDA[24]. Q_m, Q_v, and mesh size increased as a function of PEGDA molecular weight. The elastic moduli, swelling ratios and mesh size, as well as the estimated hydrodynamic radii of each therapeutic agent, are summarized in **Table 4.1**. Overall, PEGDA 3350 was chosen as the optimal molecular weight because of its moderate elastic modulus similar to that of the skin (~150 kPa). Additionally, its light-weight solid form offers handling advantages. As mentioned earlier, the applications for these hydrogels will require a durable wound dressing precursor. The calculated mesh size of 50.6 ± 0.20 nm was also desirable as this is moderate enough to absorb wound exudate present in large wounds, yet not too large to compromise the mechanical integrity of the hydrogel making it too weak for rigorous applications such as use in battlefield scenarios.

Table 4. 1. Showing the experimental and derived mechanical properties of the different molecular weight PEGDA hydrogels. The equilibrium swelling ratio (Q_m), volumetric swelling ratio (Q_V) and mesh size were calculated using the Flory-Rehner theory.

PEGDA	Elastic Modulus (kPa)	Q_m	Q_v	Mesh size (nm)	Therapeutic Agent	r_s (nm)
700	519 ± 24.9	4.41 ± 0.06	4.88 ± 0.07	18.8 ± 0.09	Tranexamic acid	0.49
2000	382 ± 21.6	5.88 ± 0.04	6.95 ± 0.05	35.2 ± 0.09	Lidocaine	0.55

3350	175 ± 11.4	7.82 ± 0.09	9.25 ± 0.11	50.6 ± 0.20	Tobramycin	0.69
4600	118 ± 20.8	10.9 ± 0.35	12.9 ± 0.43	68.4 ± 0.76	Vancomycin	1.00

4.3.3 Therapeutic release – drug release profiles

In vitro kinetic release profiles (**Fig. 4.3**) show that vancomycin is slowly released over a four-day period. Tobramycin releases faster, with cumulative concentration plateauing after approximately 24 h. The sustained release of both antibiotics is desirable for extended treatment of bacterial challenges. Lidocaine diffuses out of the hydrogel over a 2.5-day period, with 80% release within 8 h. This balance of relatively quick initial release with continual release over several days is beneficial, as sufficient lidocaine will be released to provide pain relief quickly, but the intermediate duration of efficacy of lidocaine necessitates controlled relief for extended pain management. Finally, TXA exhibits burst release, which is ideal for controlling bleeding quickly. The observed release trends can be attributed to the relationship between the hydrogels' mechanical properties, particularly its mesh size (nm) and the estimated hydrodynamic radii (r_s) embedded therapeutics. In this case, vancomycin having the highest r_s value, exhibited a more sustained release when compared to other therapeutics. This trend remained constant across all tested therapeutics (**Table 4.1**).

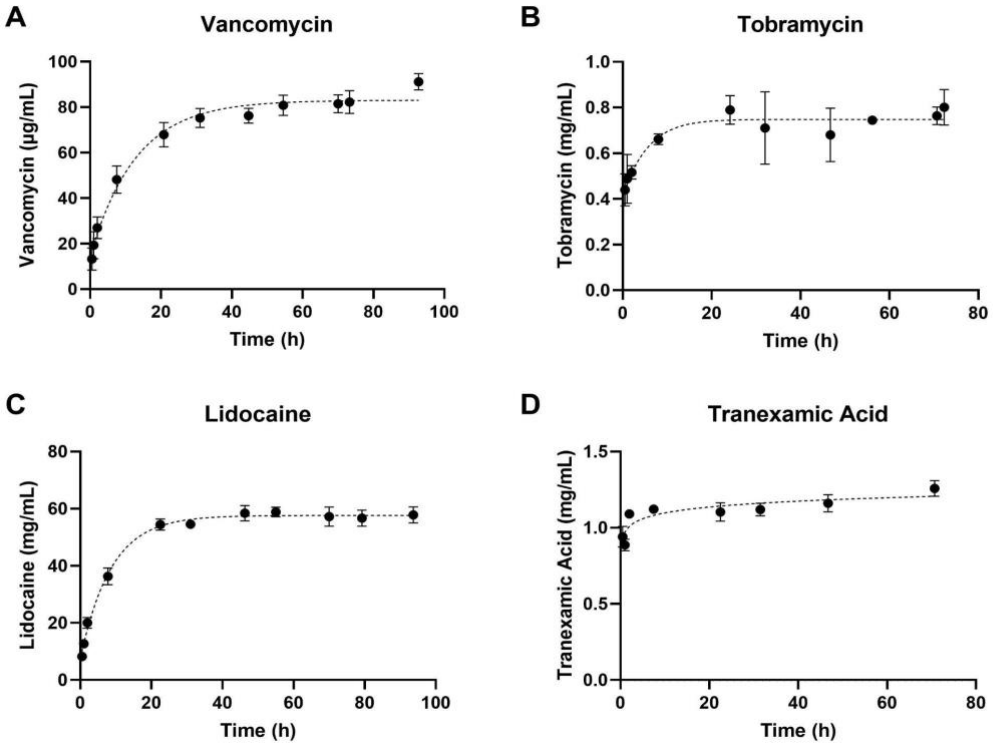

Figure 4. 3. Kinetic release profiles of therapeutic agents from PEGDA 3350 hydrogels: A) vancomycin, B) tobramycin, C) lidocaine, and D) TXA.

4.3.4 Validation of multi-drug release

An important component of our hydrogel design is the ability to release multiple therapeutics addressing bacterial colonization of wounds, hemorrhage and pain. To ensure that multi-drug loading does not affect the observed hydrogel release kinetics in single drugs, HPLC and mass spectrometry were used to validate release. Vancomycin was used as the model drug in these experiments. First, retention times for vancomycin and lidocaine were determined using a mixture of all therapeutic agents in HPLC solvents (**Fig. 4.4A**). Following this, HPLC was performed on eluent from a hydrogel containing all therapeutic agents (**Fig. 4.4B**). The results indicate that 98% of vancomycin was released from the multi-drug loaded hydrogel after a 48-hour incubation period. This finding is in alignment with our previous study where a 96% release of vancomycin was observed from the single-drug hydrogel (**Fig. 4.3A**). This

comparative analysis suggests that the kinetics of vancomycin release are not significantly influenced by the presence of additional therapeutic agents within the hydrogel matrix. The results of this study support our hypothesis that multi-drug loading does not adversely affect the release kinetics of vancomycin. This observation is critical for the development of combination therapy (with vancomycin, lidocaine, TXA and tobramycin). It implies that the pharmacokinetic profiles of individual drugs may remain intact even when administered in conjunction with the other therapeutics. Finally, efficacy of our separation method was validated by ESI-MS, which confirmed the presence of vancomycin.

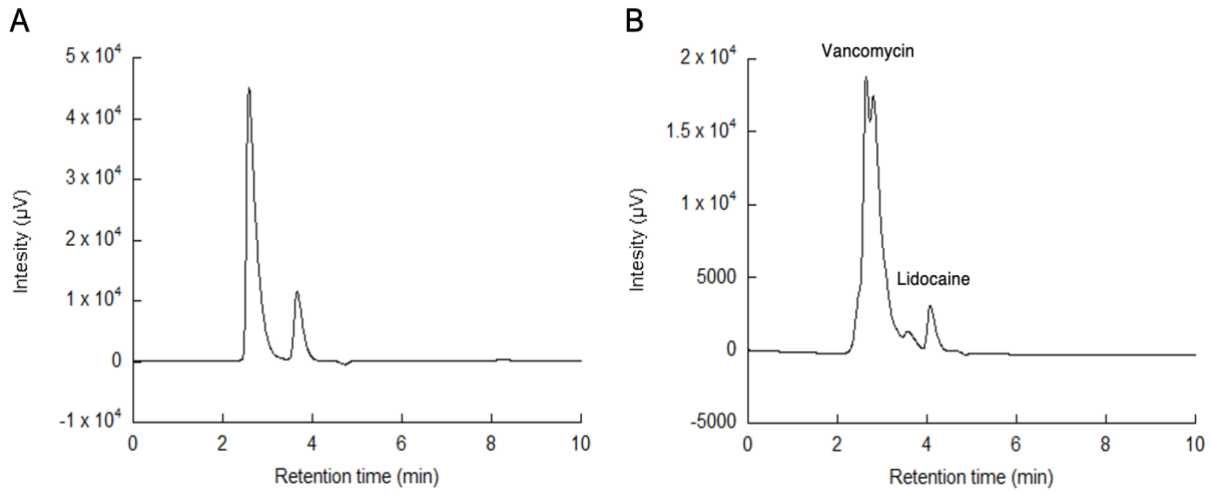

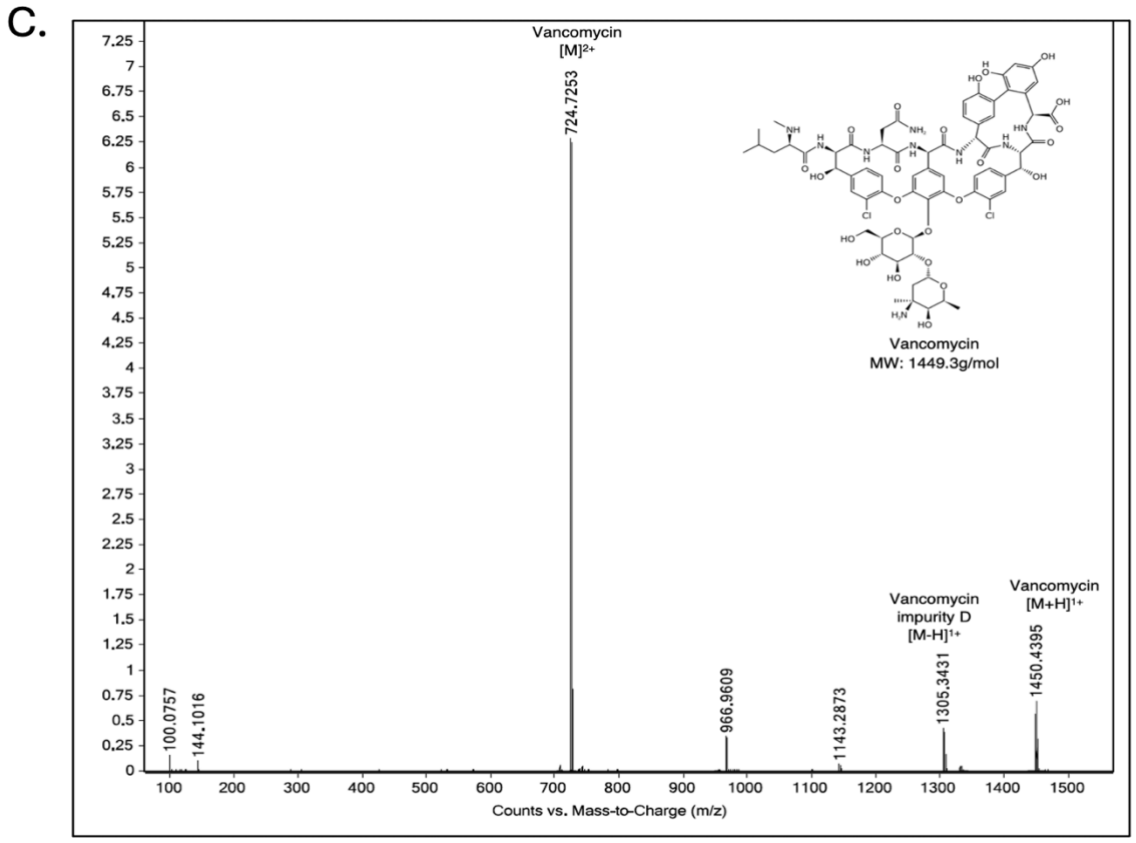

Figure 4. 4. HPLC chromatograms A) showing the retention times of vancomycin and lidocaine; B) showing the detection and separation of vancomycin and lidocaine from a hydrogel system containing all therapeutics. Retention times: Vancomycin; 2.6 – 3 min. Lidocaine; 3.7 – 4.2 min. C) Mass spectrum (electrospray ionization) of vancomycin, isolated from a hydrogel system containing all therapeutics. *Sample collected post-HPLC separation*.

4.3.5 Efficacy of antibiotic release

Broth microdilution assay is one of the most commonly used techniques to determine the minimum inhibitory concentration (MIC) of antimicrobial agents including antibiotics. The incentive of having dual release of vancomycin and tobramycin is to target both gram positive and gram negative bacteria known to colonize wounds in battlefield scenarios. After a 5 day incubation in PBS, we recorded ~177.5 µg vancomycin and ~239.3 µg tobramycin release from the hydrogel discs. These values were used to calculate the MIC after broth microdilution. The

MIC of vancomycin and tobramycin were evaluated individually (**Fig. 4.5A**), and simultaneously from a hydrogel loaded with both antibiotics (**Fig. 4.5B**). Vancomycin released from the hydrogels had an MIC of 4.6 ± 1.5 μg/mL against *S. aureus*, and released tobramycin had a MIC of 7.5 ± 1.7 μg/mL against *E. coli*. We observed that the MICs of dual-antibiotic-loaded hydrogels were actually lower than that of single-antibiotic gels or it remained approximately unchanged (**Table 4.2**). Compared to the standard concentrations published by the Clinical and Laboratory Standards Institute (CLSI), the recorded MIC values for the hydrogel-released antibiotic were of the same order of magnitude, demonstrating its ability to remain effective against bacteria after five days of release. The dual-antibiotic-loaded hydrogels exhibited a slightly higher efficacy. While no statistically significant differences were observed between these values, the enhanced efficacy may be attributed to the potential synergistic interactions between the mechanisms of action of the two antibiotics. Vancomycin primarily inhibits bacterial cell wall synthesis, while aminoglycosides like tobramycin are typically less effective against Gram-positive bacteria. However, increased cell membrane permeability can enhance tobramycin's effectiveness against *S. aureus*, contributing to the improved bacterial inhibition observed. For *E. coli*, although tobramycin is its primary antibiotic, vancomycin may still play a minor role by increasing membrane permeability, making *E. coli* more susceptible to tobramycin[14,25].

Table 4. 2. Showing the MIC of antibiotics released from the hydrogel against *S. aureus* and *P. aeruginosa*

	MIC (CLSI/Lit.)	**Tobramycin Hydrogel**	**Vancomycin Hydrogel**	**Tobramycin + Vancomycin Hydrogel**
S. Aureus	≤ 2 μg/mL	–	4.60 ± 1.50 μg/mL	3.60 ± 0.30 μg/mL
E. Coli	≤1 μg/mL	7.48 ± 1.70 μg/mL	–	5.37 ± 0.50 μg/mL

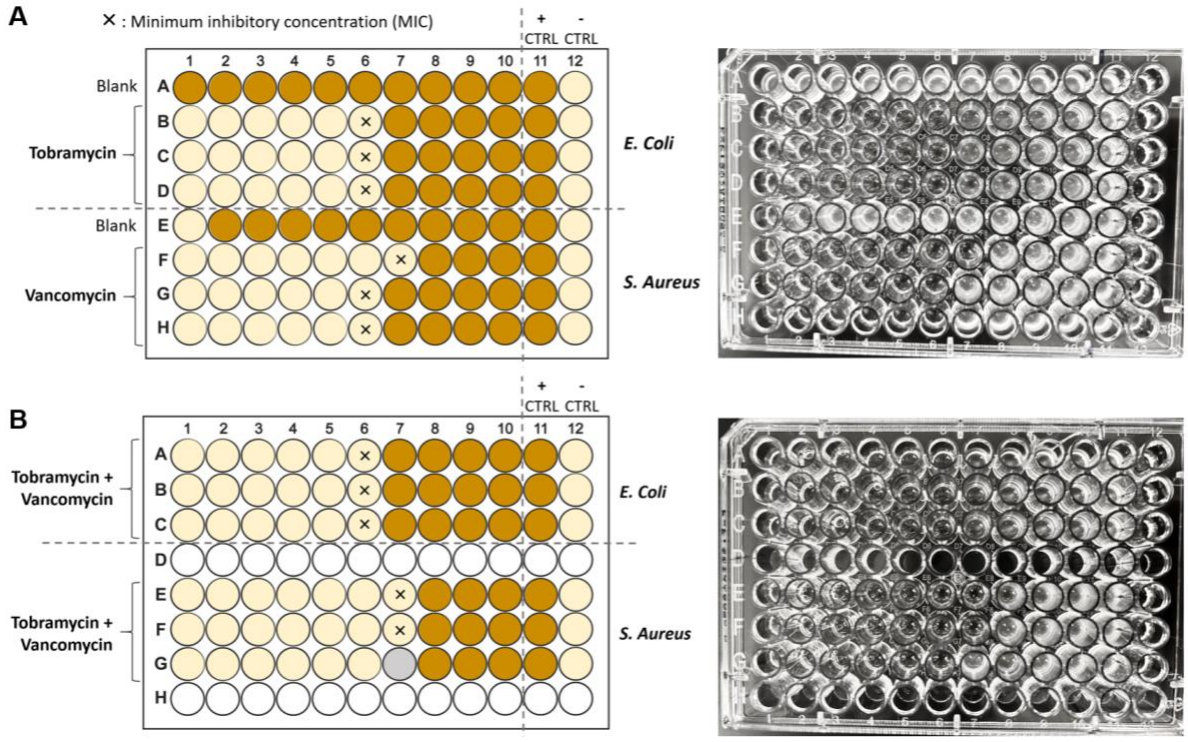

Figure 4. 5. Minimum inhibitory concentration (MIC) assay for PEGDA 3350 hydrogels A) loaded separately with tobramycin and vancomycin and B) loaded with both tobramycin and vancomycin, against *E. coli* and *S. aureus*. MIC results are graphically depicted on the *left*, with the original scanned plates shown on the *right*.

4.3.6 *In vivo* efficacy of drug release

To test the efficacy of the drug loaded hydrogels in preventing infection in *in vivo* models, our collaborators in the Bernthal group applied the hydrogels to murine open fractures inoculated with bioluminescent *S. aureus*, *E. coli*, and *P. aeruginosa*. In these group of experiments, the infectious burden was tracked via bioluminescence. Control mice were treated with antibiotic powder during surgery or with a hydrogel containing no antibiotics. *In vivo* longitudinal bioluminescence demonstrated that the unloaded hydrogel group had the highest bioluminescent signal followed by the infected control group. (**Fig. 4.6A**). As expected, with the addition of any foreign body in an infected environment, infectious burden was increased with an "empty" polymer without embedded antimicrobial agents. Alternatively, the drug

loaded hydrogel group demonstrated a gradual decrease in bioluminescent signal over three days until it reached the sterile control line, indicating the consistent elution of antibiotics over this period. The antibiotic powder group demonstrated no bioluminescent signal throughout the post-operative period. On post-operative day 5 (POD5), the hydrogel infected group had the highest fluorescent signal, indicating the most granulocytes recruited and inflammatory burden (**Fig. 4.6B**). Granulocyte recruitment did not differ between infected control, antibiotic powder, and drug loaded hydrogel groups. Sterile mice recruited the least number of granulocytes, but this finding was not statistically significant. Of the thirty mice who received either antibiotic powder or drug loaded hydrogel, all mice were culture negative at the end of the experiment (**Fig. 4.6C** and **4.6D**). When comparing the infected control group to our unloaded hydrogel group, the presence of hydrogel alone seemed to increase the bacterial burden of both gram-positive and gram-negative species harvested from implants and tissue. Following this experiment, the hydrogels were explanted from the murine wound model and total drug release was evaluated. Vancomycin was used as the model drug because of our established HPLC and mass spectrometry methods. Here we confirmed little to no therapeutics entrapped within the hydrogel matrix with a calculated average of 96.9% release in infected samples and 94.8% in sterile samples.

Finally, the Bernthal group performed *Ex vivo* Thromboelastography (TEG) assays to validate the release of TXA. The results demonstrate that hydrogels do not induce coagulopathy when co-incubated with blood for 24 hours and can effectively elute TXA to stabilize clots and prevent thrombolysis in the presence of tPa, a robust thrombolytic agent. Histological analyses also showed no evidence of renal toxicity (**Fig. S4.4, S4.5**).

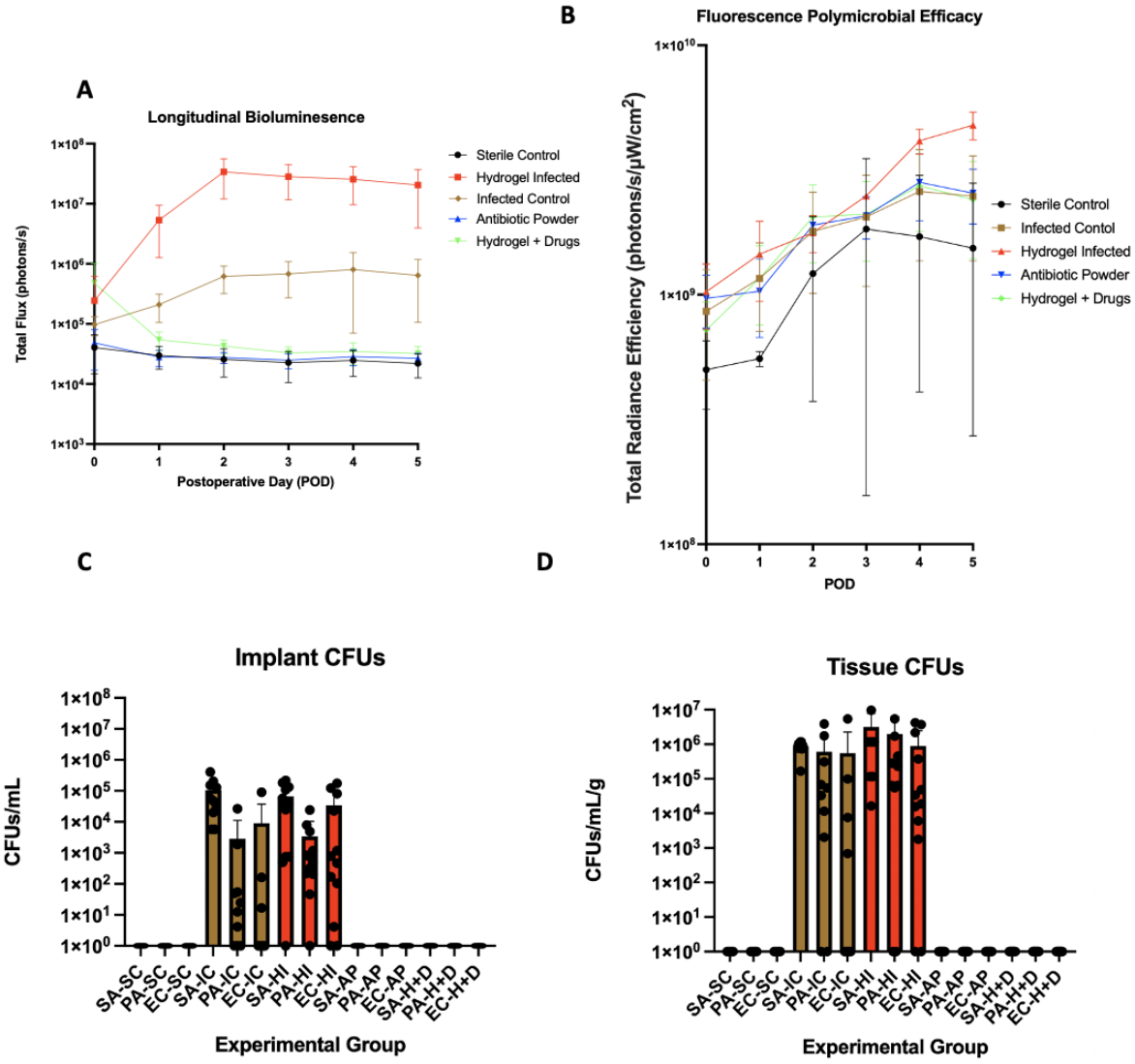
A
Longitudinal Bioluminesence
Total Flux (photons/s)
Postoperative Day (POD)
Sterile Control
Hydrogel Infected
Infected Control
Antibiotic Powder
Hydrogel + Drugs
B
Fluorescence Polymicrobial Efficacy
Total Radiance Efficiency (photons/s/μW/cm²)
POD
Sterile Control
Infected Contol
Hydrogel Infected
Antibiotic Powder
Hydrogel + Drugs
C
Implant CFUs
CFUs/mL
Experimental Group
SA-SC
PA-SC
EC-SC
SA-IC
PA-IC
EC-IC
SA-HI
PA-HI
EC-HI
SA-AP
PA-AP
EC-AP
SA-H+D
PA-H+D
EC-H+D
D
Tissue CFUs
CFUs/mL/g
Experimental Group

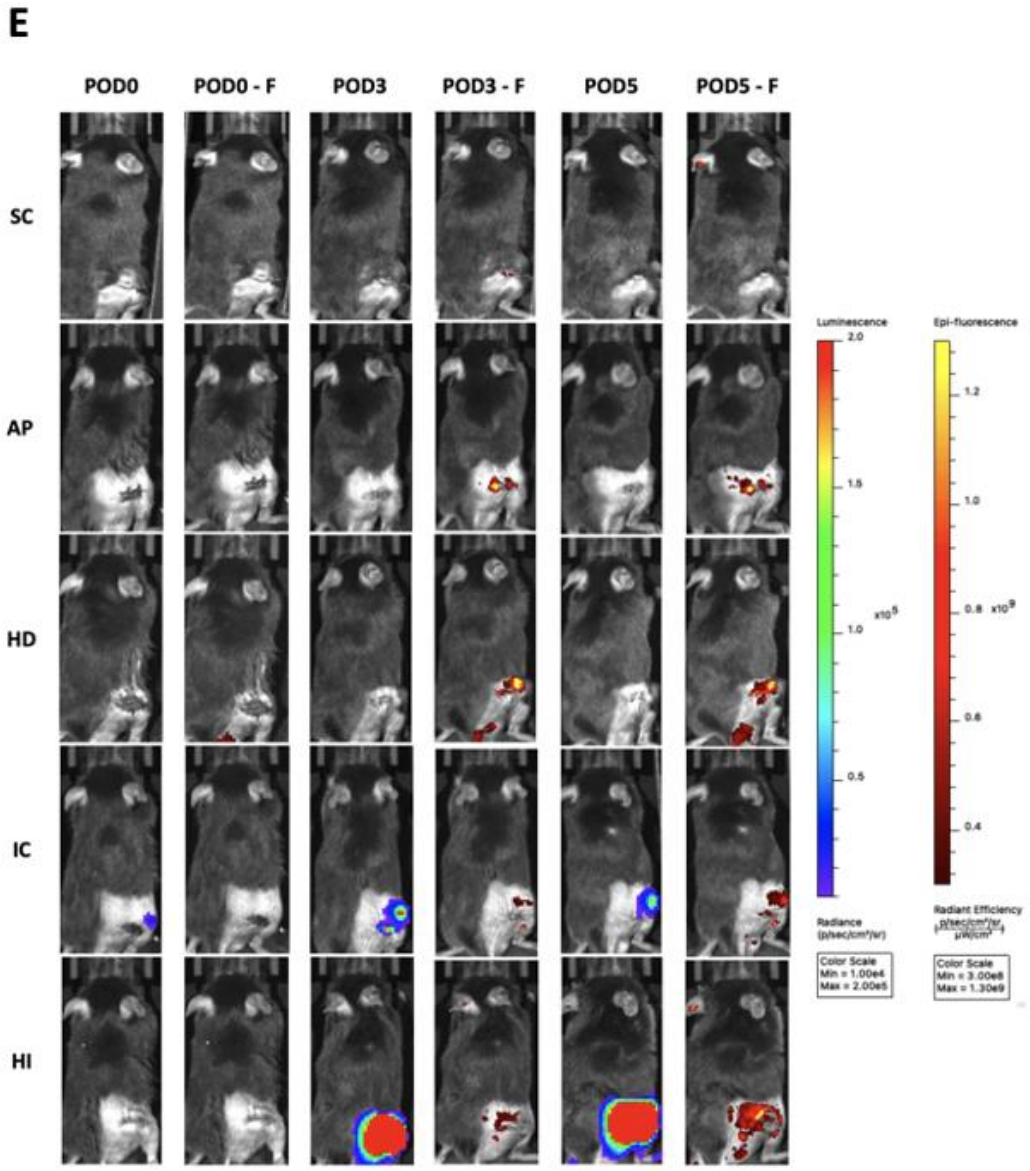

Figure 4. 6. In vivo efficacy of drug release in murine models. SC = sterile control. IC = infected control. HI = hydrogel infected. AP = antibiotic powder. H+D = Hydrogel + drugs. A) Longitudinal bioluminescence representing bacterial burden over 5 postoperative days. B) Longitudinal fluorescence representing neutrophil recruitment to surgical site over 5 postoperative days. C) Implant CFUs from Xen36, Xen41, and Xen14 which were isolated and selectively grown per experimental group. D) Tissue CFUs from Xen36, Xen41, and Xen14 which were isolated and selectively grown per experimental group. E) Representative *in vivo*

images demonstrating bioluminescent (bacterial) and fluorescent (neutrophil) signals in representative mice from each experimental group on PODs 1, 3, and 5.

4.3.7 Large animal studies: Merino sheep wound model

The large animal studies were performed in collaboration with the Wenke group at University of Texas Medical Branch. For these experiments, a trip was made to Texas to facilitate hydrogel synthesis and scale-up while the remaining surgeries were conducted by Dr Wenke and his team. An open fracture and complex wound of the proximal tibia was created in adult Merino female sheep and inoculated with *S. aureus* (1×10^8 CFU/ml) spread over the entirety of the wound surface (**Fig. 4.7A**). After a 6 h incubation, sheep underwent surgical wound debridement, and wound dressings were polymerized and subsequently applied (**Fig. 4.7B**). Control animals did not receive any treatment beyond debridement. The control- and hydrogel-treated groups were imaged with a photon-counting camera 0 h post-debridement and 48 h post-debridement (**Fig. 4.7C**). After 48 h, the control group (*grey*) exhibited an *S. aureus* burden of 632.1 ± 602.6% relative to pre-debridement levels (**Fig. 4.7D**). The hydrogel-treated group had a significantly lower burden of 8.1 ± 11.9% (*blue*). The large standard deviation of the hydrogel group is due to sheep #4, in which the hydrogel had slipped out of place; even in this instance, the bacterial burden was 25.8% relative to pre-debridement levels. Were this animal participant excluded from analysis, the hydrogel-treated group exhibits a burden of 2.3 ± 2.0%. These data suggest that these therapeutic releasing hydrogels can prevent infection and sepsis for at least 48 h post-traumatic injury. The results of this work validates the initial vision of translating benchtop research into preclinical models, bridging the gap between laboratory innovation and real-world application.

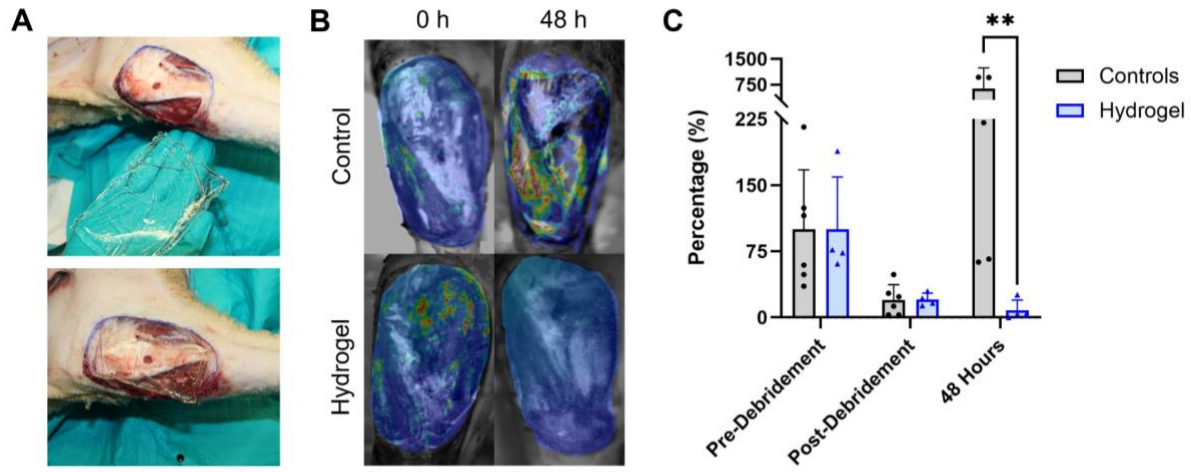

Figure 4. 7. *In vivo* efficacy in ovine models. A) Merino sheep complex musculoskeletal wound model, with injuries to the anterior tibia, muscle, fascia, and periosteum, hydrogel application in sheep model B) Images of bioluminescent bacteria within the wound 0 h and 48 h post-debridement C) *S. aureus* contaminated wounds were created in the ovine model and underwent debridement after 6 h. Photon counts were normalized with respect to the pre-debridement values of each respective group, for percentage of pre-debridement bacterial burden.

4.4 Conclusions

Hydrogel dressings are gaining attention as a promising tool for advanced wound care and treatment due to their ability to provide hydration and deliver therapeutics. In this work, through material design and optimization, a simple *in vitro* system was successfully translated into a model that demonstrated promising results in pre-clinical studies. The antibiotics in our system displayed release over a two-day period and demonstrated efficacy in both *in vitro* microbial assays and animal models. The pain and hemorrhage control component of our hydrogels were also effective. Notably, our findings indicate that the short polymerization time and the physical state of our hydrogel precursor make it well-suited for applications requiring

prolonged field care. Beyond the scope of this study, our hydrogel has potential in surgical, burn or chronic wounds. Furthermore, these PEGDA hydrogels provide a great foundation to build upon for wound healing, as other components like biodegradation can be incorporated through the use of hydrolyzable linkages.

4.5 Supplemental Information

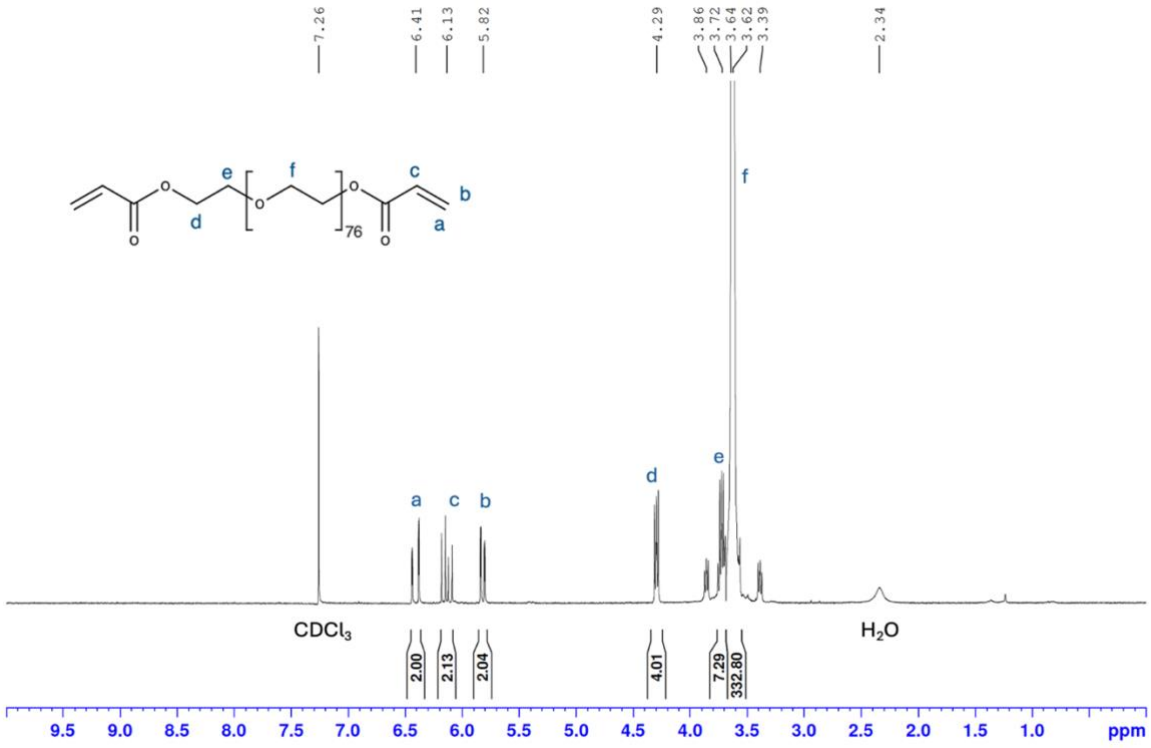

Figure S4.1: [1]HNMR spectrum of poly (ethylene) glycol diacrylate (PEGDA). *Acrylation = 90.7%*

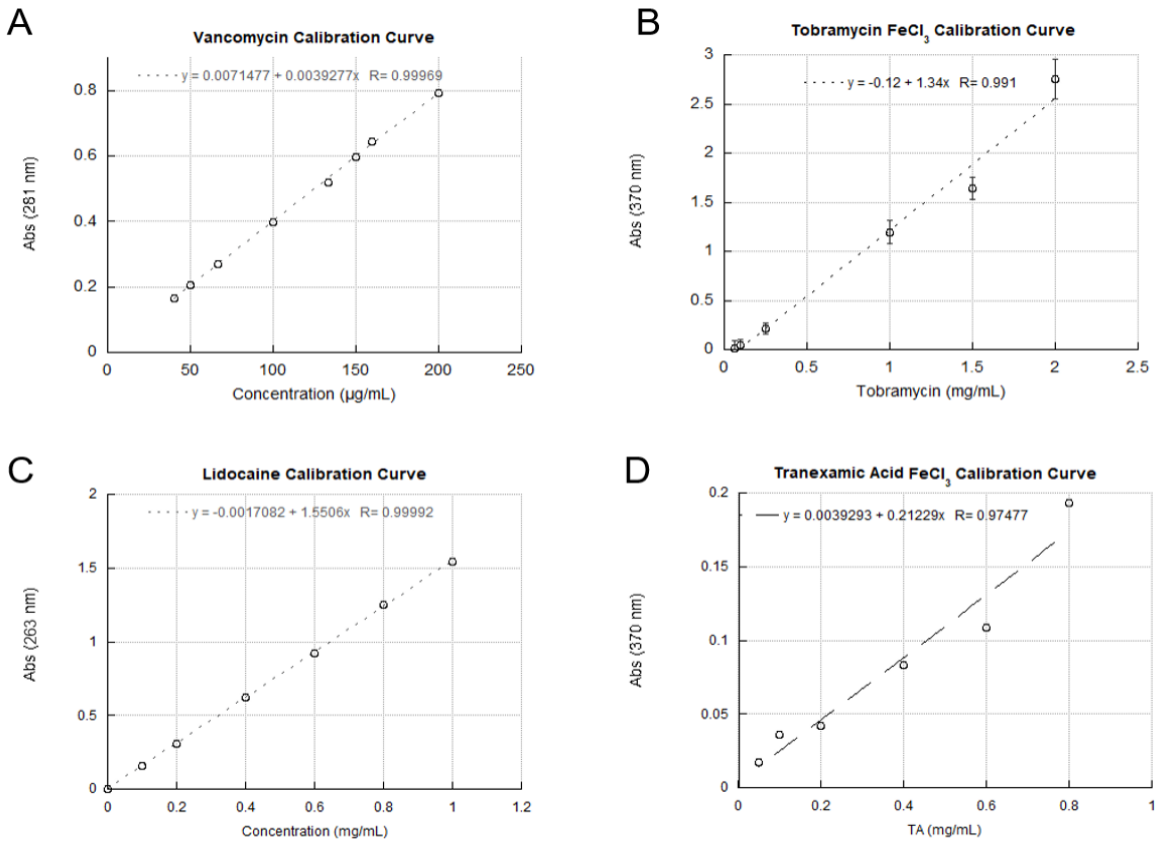

Figure S4.2. UV-visible calibration relating concentration to absorbance of (**A**) vancomycin at 281 nm, (**B**) tobramycin with 0.2% $FeCl_3$ at 370 nm, (**C**) lidocaine at 283 nm, and (**D**) tranexamic acid with 0.2% $FeCl_3$ at 370 nm.

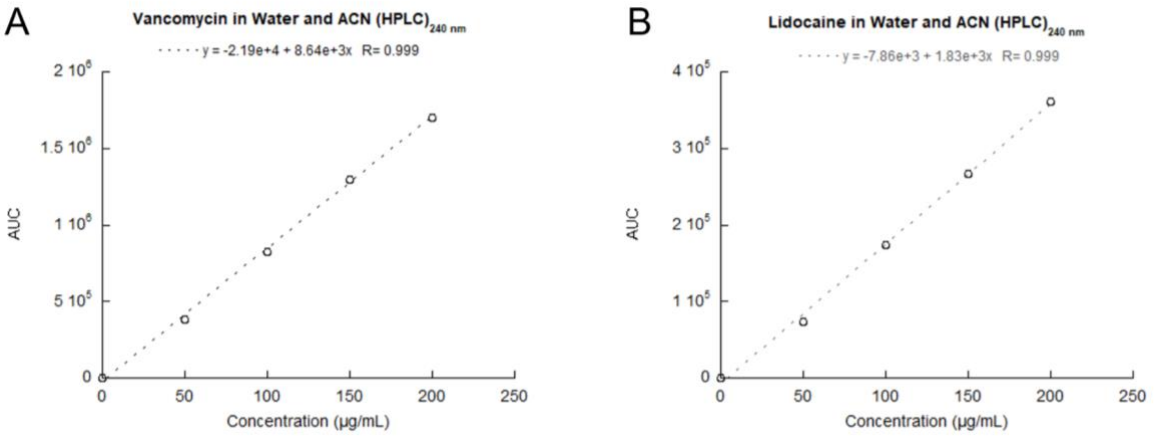

Figure S4.3. HPLC calibration curves for area under the curve (AUC) as a function of (**A**) vancomycin and (**B**) lidocaine concentration, recorded with a mobile phase containing 70:30 (v/v) water and acetonitrile.

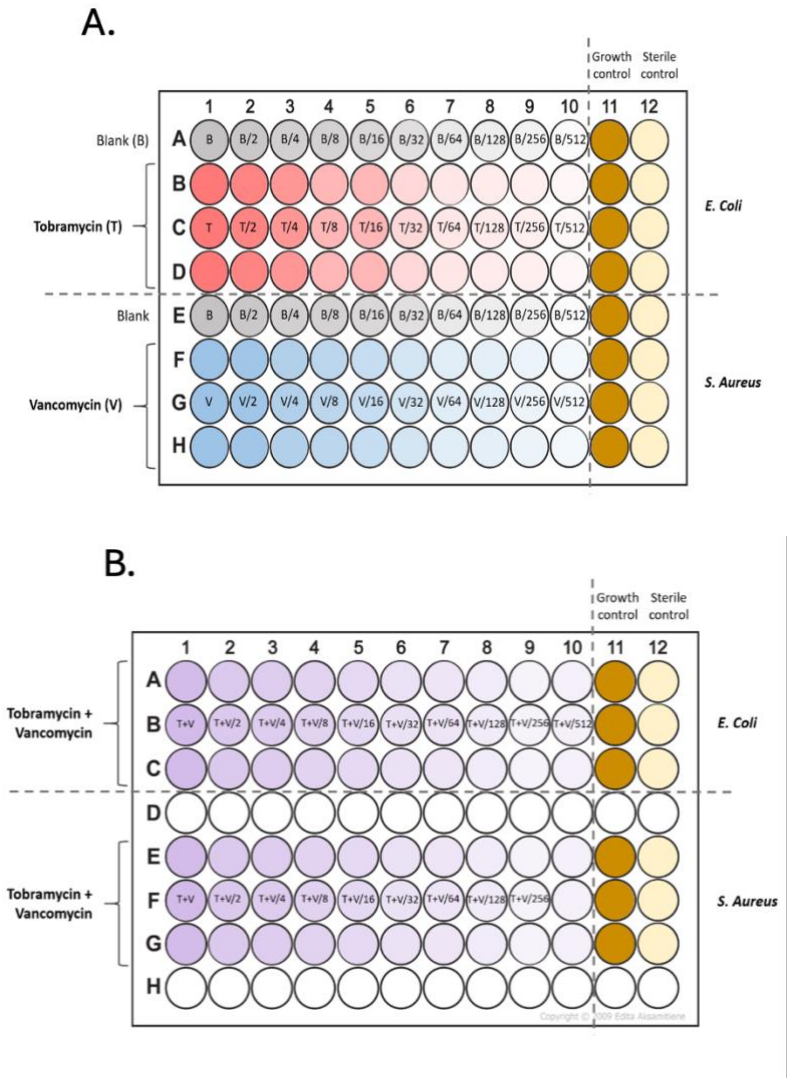

Figure S4.4. Plate maps for LB broth microdilution assay to determine the minimum inhibitory concentration (MICs) of tobramycin-loaded hydrogels, vancomycin-loaded hydrogels, and dual-antibiotic-loaded hydrogels against *E. coli* and *S. aureus* strains. A) single antibiotics in each well plate (vancomycin and tobramycin, and B) dual antibiotics (vancomycin + tobramycin). *Positive growth controls (11) contain log-phase bacterial culture in media, and negative sterile controls (12) contain media alone.*

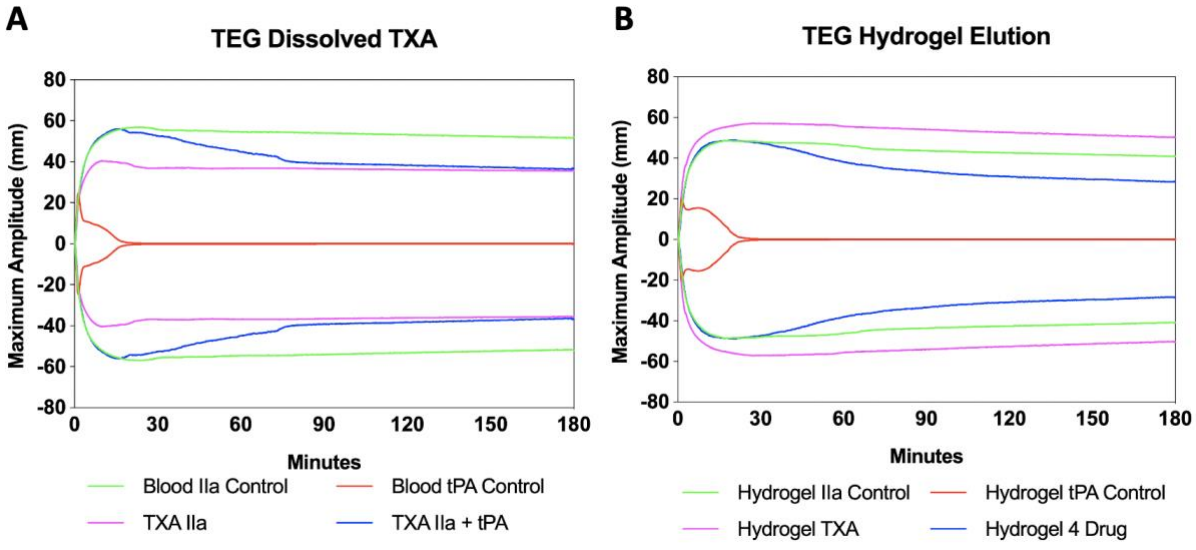

Figure S4.5. Efficacy of released tranexamic acid (TXA) (**A**) TEG curve for experiment 1 testing C57BL/6 mouse blood with or without dissolved TXA. (**B**) TEG curve for experiment 2 demonstrating C57BL/6 mouse blood incubated with hydrogel overnight. Clot strength is determined by a measure of maximum amplitude (mm). *Experiments and result analysis done by the Bernthal group*

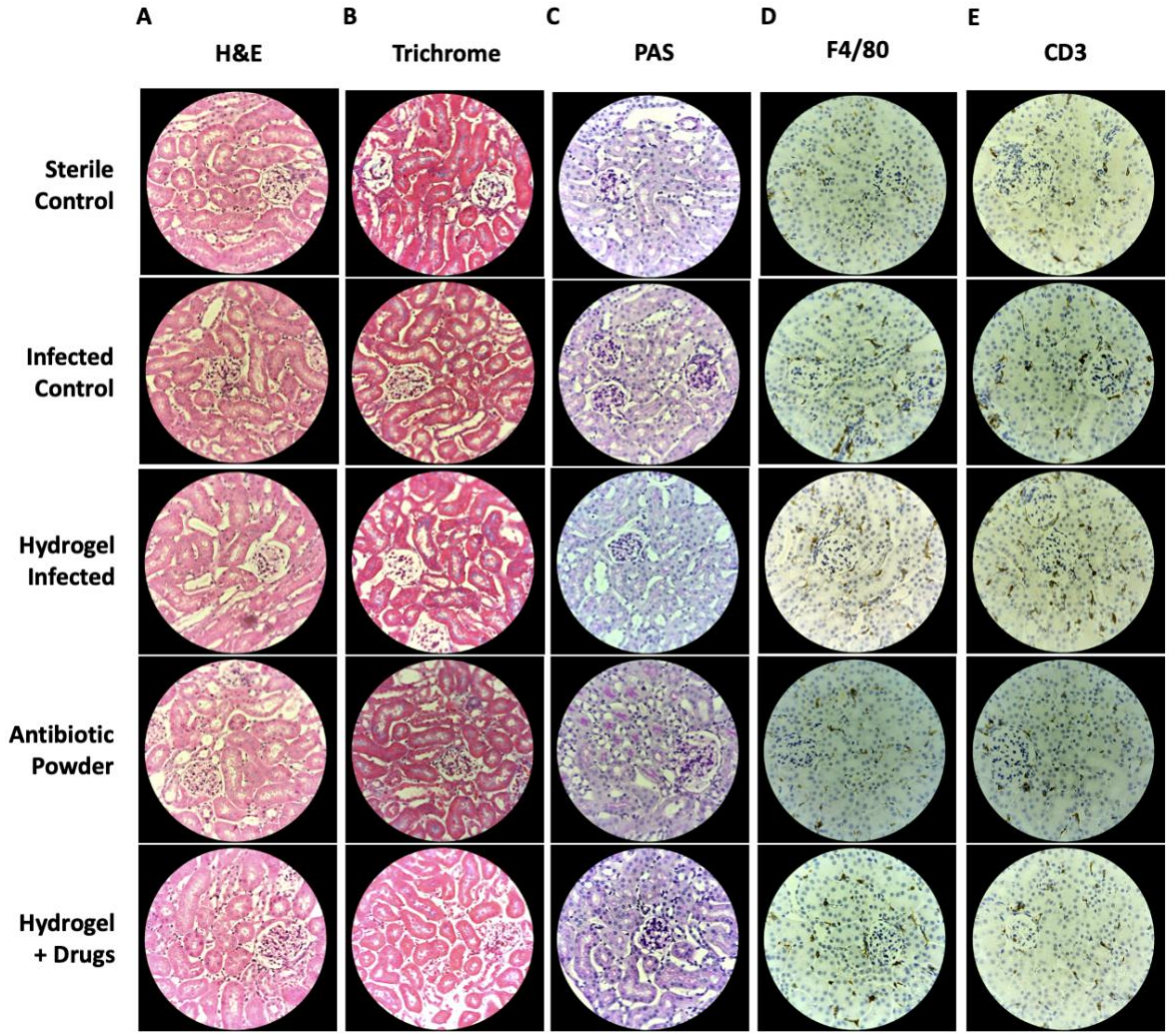

Figure S4.6. Tissue Histologic Analysis. Kidney sections obtained per experimental group on POD5 (**A**) H&E (**B**) Trichrome (**C**) PAS (**D**) IHC F4/80 (**E**) IHC CD3. *Experiments and result analysis done by the Bernthal group*

References

(1) Cross, J. D.; Ficke, J. R.; Hsu, J. R.; Masini, B. D.; Wenke, J. C. Battlefield Orthopaedic Injuries Cause the Majority of Long-Term Disabilities. *JAAOS - J. Am. Acad. Orthop. Surg.* **2011**, *19*, S1.

(2) Kotwal, R. S.; Howard, J. T.; Orman, J. A.; Tarpey, B. W.; Bailey, J. A.; Champion, H. R.; Mabry, R. L.; Holcomb, J. B.; Gross, K. R. The Effect of a Golden Hour Policy on the Morbidity and Mortality of Combat Casualties. *JAMA Surg.* **2016**, *151* (1), 15–24. https://doi.org/10.1001/jamasurg.2015.3104.

(3) Keenan, S.; Riesberg, J. C. Prolonged Field Care: Beyond the "Golden Hour." *Wilderness Environ. Med.* **2017**, *28* (2S), S135–S139. https://doi.org/10.1016/j.wem.2017.02.001.

(4) Wei, X.; Cai, J.; Wang, C.; Yang, K.; Ding, S.; Tian, F.; Lin, S. Quaternized Chitosan/Cellulose Composites as Enhanced Hemostatic and Antibacterial Sponges for Wound Healing. *Int. J. Biol. Macromol.* **2022**, *210*, 271–281. https://doi.org/10.1016/j.ijbiomac.2022.05.007.

(5) Valentine, K. P.; Viacheslav, K. M. Bacterial Flora of Combat Wounds from Eastern Ukraine and Time-Specified Changes of Bacterial Recovery during Treatment in Ukrainian Military Hospital. *BMC Res. Notes* **2017**, *10* (1), 152. https://doi.org/10.1186/s13104-017-2481-4.

(6) Ibberson, C. B.; Barraza, J. P.; Holmes, A. L.; Cao, P.; Whiteley, M. Precise Spatial Structure Impacts Antimicrobial Susceptibility of S. Aureus in Polymicrobial Wound Infections. *Proc. Natl. Acad. Sci.* **2022**, *119* (51), e2212340119. https://doi.org/10.1073/pnas.2212340119.

(7) DeLeon, S.; Clinton, A.; Fowler, H.; Everett, J.; Horswill, A. R.; Rumbaugh, K. P. Synergistic Interactions of Pseudomonas Aeruginosa and Staphylococcus Aureus in an In

Vitro Wound Model. *Infect. Immun.* **2014**, *82* (11), 4718–4728. https://doi.org/10.1128/iai.02198-14.

(8) Fredua-Agyeman, M.; Gaisford, S.; Beezer, A. E. Observation with Microcalorimetry: Behaviour of *P. Aeruginosa* in Mixed Cultures with *S. Aureus* and *E. Coli*. *Thermochim. Acta* **2018**, *663*, 93–98. https://doi.org/10.1016/j.tca.2018.03.009.

(9) Wyldbore, M.; Aldington, D. Trauma Pain – a Military Perspective. *Br. J. Pain* **2013**, *7* (2), 74–78. https://doi.org/10.1177/2049463713487515.

(10) Shackelford, S. A.; Del Junco, D. J.; Riesberg, J. C.; Powell, D.; Mazuchowski, E. L.; Kotwal, R. S.; Loos, P. E.; Montgomery, H. R.; Remley, M. A.; Gurney, J. M.; Keenan, S. Case-Control Analysis of Prehospital Death and Prolonged Field Care Survival during Recent US Military Combat Operations. *J. Trauma Acute Care Surg.* **2021**, *91* (2S Suppl 2), S186–S193. https://doi.org/10.1097/TA.0000000000003252.

(11) Dolan, C. P.; Valerio, M. S.; Lee Childers, W.; Goldman, S. M.; Dearth, C. L. Prolonged Field Care for Traumatic Extremity Injuries: Defining a Role for Biologically Focused Technologies. *Npj Regen. Med.* **2021**, *6* (1), 1–4. https://doi.org/10.1038/s41536-020-00117-9.

(12) Calder, D.; Fathi, A.; Oveissi, F.; Maleknia, S.; Abrams, T.; Wang, Y.; Maitz, J.; Tsai, K. H.-Y.; Maitz, P.; Chrzanowski, W.; Canoy, I.; Menon, V. A.; Lee, K.; Ahern, B. J.; Lean, N. E.; Silva, D. M.; Young, P. M.; Traini, D.; Ong, H. X.; Mahmoud, R. S.; Montazerian, H.; Khademhosseini, A.; Dehghani, F. Thermoresponsive and Injectable Hydrogel for Tissue Agnostic Regeneration. *Adv. Healthc. Mater.* **2022**, *11* (23), 2201714. https://doi.org/10.1002/adhm.202201714.

(13) Kratochvil, M. J.; Seymour, A. J.; Li, T. L.; Paşca, S. P.; Kuo, C. J.; Heilshorn, S. C. Engineered Materials for Organoid Systems. *Nat. Rev. Mater.* **2019**, *4* (9), 606–622. https://doi.org/10.1038/s41578-019-0129-9.

(14) Watanakunakorn, C.; Tisone, J. C. Synergism Between Vancomycin and Gentamicin or Tobramycin for Methicillin-Susceptible and Methicillin-Resistant Staphylococcus Aureus Strains. *Antimicrob. Agents Chemother.* **1982**, *22* (5), 903–905. https://doi.org/10.1128/aac.22.5.903.

(15) Han, W.; Zhang, L.; Yu, L.; Wang, J. Effect of Local Delivery of Vancomycin and Tobramycin on Bone Regeneration. *Orthop. Surg.* **2021**, *13* (5), 1654–1661. https://doi.org/10.1111/os.13020.

(16) Napolitano, L. M.; Cohen, M. J.; Cotton, B. A.; Schreiber, M. A.; Moore, E. E. Tranexamic Acid in Trauma: How Should We Use It? *J. Trauma Acute Care Surg.* **2013**, *74* (6), 1575–1586. https://doi.org/10.1097/TA.0b013e318292cc54.

(17) Morrison, J. J.; Dubose, J. J.; Rasmussen, T. E.; Midwinter, M. J. Military Application of Tranexamic Acid in Trauma Emergency Resuscitation (MATTERs) Study. *Arch. Surg.* **2012**, *147* (2), 113–119. https://doi.org/10.1001/archsurg.2011.287.

(18) Liu, M.; Yang, Z.-H.; Li, G.-H. A Novel Method for the Determination of Vancomycin in Serum by High-Performance Liquid Chromatography-Tandem Mass Spectrometry and Its Application in Patients with Diabetic Foot Infections. *Molecules* **2018**, *23* (11), 2939. https://doi.org/10.3390/molecules23112939.

(19) Lima, T. de M.; Seba, K. S.; Gonçalves, J. C. S.; Cardoso, F. L. L.; Estrela, R. de C. E. A Rapid and Simple HPLC Method for Therapeutic Monitoring of Vancomycin. *J. Chromatogr. Sci.* **2018**, *56* (2), 115–121. https://doi.org/10.1093/chromsci/bmx089.

(20) Al Nebaihi, H. M.; Primrose, M.; Green, J. S.; Brocks, D. R. A High-Performance Liquid Chromatography Assay Method for the Determination of Lidocaine in Human Serum. *Pharmaceutics* **2017**, *9* (4), 52. https://doi.org/10.3390/pharmaceutics9040052.

(21) Wiegand, I.; Hilpert, K.; Hancock, R. E. W. Agar and Broth Dilution Methods to Determine the Minimal Inhibitory Concentration (MIC) of Antimicrobial Substances. *Nat. Protoc.* **2008**, *3* (2), 163–175. https://doi.org/10.1038/nprot.2007.521.

(22) Phadke, A.; Zhang, C.; Arman, B.; Hsu, C.-C.; Mashelkar, R. A.; Lele, A. K.; Tauber, M. J.; Arya, G.; Varghese, S. Rapid Self-Healing Hydrogels. *Proc. Natl. Acad. Sci.* **2012**, *109* (12), 4383–4388. https://doi.org/10.1073/pnas.1201122109.

(23) Li, J.; Mooney, D. J. Designing Hydrogels for Controlled Drug Delivery. *Nat. Rev. Mater.* **2016**, *1* (12), 1–17. https://doi.org/10.1038/natrevmats.2016.71.

(24) Flory, P. J.; Rehner, J. Statistical Mechanics of Cross-Linked Polymer Networks II. Swelling. *J. Chem. Phys.* **1943**, *11* (11), 521–526. https://doi.org/10.1063/1.1723792.

(25) Muheim, C.; Götzke, H.; Eriksson, A. U.; Lindberg, S.; Lauritsen, I.; Nørholm, M. H. H.; Daley, D. O. Increasing the Permeability of Escherichia Coli Using MAC13243. *Sci. Rep.* **2017**, *7* (1), 17629. https://doi.org/10.1038/s41598-017-17772-6.

Chapter 5: Future perspective and broader impact

The theme of this work was to utilize chemical synthesis and engineering principles to address complications that present as urgent, real-world clinical challenges. The promising outcomes from the flavonoid-based polymers lay a strong foundation for the development of novel therapies that are clinically and economically relevant. The sustained release observed from the flavonoid-based macromers, less than 50% over 30 days, suggests significant potential for long-acting antioxidant therapies. These polymers could be further engineered into intravenous formulations that provide therapeutic benefit for up to a month, potentially reducing the frequency of dosing and associated complications such as renal toxicity. This feature addresses a well-known limitation in current vaso-occlusive crisis (VOC) management strategies, which often rely on frequent, high-dose interventions. Looking ahead, broadening the therapeutic scope of this platform will be essential. We aim to tailor the release profile through controlled functionalization such as limiting the number of targeted phenolic groups which can enable the design of flavonoid-based therapies with different release durations (e.g., 1–2 weeks). Moreover, there is a vast array of flavonoids with similar properties of apigenin and apigeninidin, expanding the flavonoid library to include flavones or flavonols with up to four phenolic groups (e.g., quercetin) could enhance antioxidant potency and therapeutic efficacy[1]. One important consideration for future studies is the biocompatibility of the chemical spacers used in macromer synthesis. To study this behavior, we plan to perform cell viability experiments on the polymer degradation products using already established cell culture methods.

From a translational stand point, the chitosan-based wound dressings developed in this study shows a potential for real-world application. Its efficacy in both wet and dry states suggests that they can be tailored for different stages of ulcer progression, creating a versatile product suitable for clinical use. To further support advancement, limulus amoebocyte lysate

(LAL) testing can be carried out to confirm that the gels are free from endotoxins before progressing to preclinical animal models[2]. Furthermore, the PEGDA-based hydrogels designed for wounded soldiers, have already progressed to pre-clinical studies in large animal models. A promising direction for future work involves incorporating hydrolyzable linkages into the hydrogel network. This will allowing the wound dressing to gradually degrade over time in a manner that can be controlled. This feature could eliminate the need for dressing removal and improving patient comfort.

Overall, although this work focused on addressing vaso-occlusive crises and the treatment of complex wounds in the context of SCD and battlefield injuries. The need for antioxidant therapy, and specialized wound care extends beyond these applications. Chronic wounds such as venous ulcers and diabetic foot ulcers share overlapping pathophysiological features such as oxidative stress, inflammation, and impaired healing, and may similarly benefit from these bioactive therapies[3,4]. The hydrogel system may also hold potential for treating acute wounds like those sustained by burn victims, where infection control, moisture balance are equally critical.

References

(1) Hassanpour, S. H.; Doroudi, A. Review of the Antioxidant Potential of Flavonoids as a Subgroup of Polyphenols and Partial Substitute for Synthetic Antioxidants. *Avicenna J. Phytomedicine* **2023**, *13* (4), 354–376. https://doi.org/10.22038/AJP.2023.21774.

(2) Mangini, M.; Verde ,Alessandro; Boraschi ,Diana; Puntes ,Victor F.; Italiani ,Paola; and De Luca, A. C. Interaction of Nanoparticles with Endotoxin Importance in Nanosafety Testing and Exploitation for Endotoxin Binding. *Nanotoxicology* **2021**, *15* (4), 558–576. https://doi.org/10.1080/17435390.2021.1898690.

(3) Bonkemeyer Millan, S.; Gan, R.; Townsend, P. E. Venous Ulcers: Diagnosis and Treatment. *Am. Fam. Physician* **2019**, *100* (5), 298–305.

(4) Falanga, V.; Isseroff, R. R.; Soulika, A. M.; Romanelli, M.; Margolis, D.; Kapp, S.; Granick, M.; Harding, K. Chronic Wounds. *Nat. Rev. Dis. Primer* **2022**, *8* (1), 1–21. https://doi.org/10.1038/s41572-022-00377-3.